Microphysical and Optical Properties of Small Atmospheric Ice Particles

Zur Erlangung des akademischen Grades eines

DOKTORS DER NATURWISSENSCHAFTEN
(Dr. rer. nat.)

von der KIT-Fakultät für Physik des
Karlsruher Instituts für Technologie (KIT)

angenommene

Dissertation

von

M.Sc. Adrian Hamel

aus Marburg

Tag der mündlichen Prüfung: 07. November 2025
1. Referent: Prof. Dr. Thomas Leisner
2. Referentin: Prof. Dr. Corinna Hoose

Abstract

Cirrus clouds are among the most common cloud types globally and play a crucial role as drivers of Earth's climate system. They have a cooling contribution through the reflection of the short wave solar radiation, while simultaneously exerting a warming effect by reflecting the long wave terrestrial radiation. To describe cirrus cloud radiative properties in climate models, a comprehensive understanding of the microphysical and optical properties of ice particles is essential. Although ice particles with sizes below 70 µm are abundant in cirrus clouds, the precise relationship between their morphological and optical properties remains unclear.

This work investigates the effect of the growth conditions on the particle size and morphological complexity of cloud chamber-grown ice particles and inland Antarctic boundary layer ice particles, with sizes predominantly below 70 µm. Furthermore, the resulting influence on their optical properties is analysed.

Cloud chamber experiments were conducted at the Aerosol Interactions and Dynamics in the Atmosphere (AIDA) cloud simulation chamber at the Karlsruhe Institute of Technology (KIT) to study ice particles at specific atmospheric conditions in detail. The measured linear depolarisation ratio of ice particles with sizes between 10 µm and 70 µm was below 0.3, which is lower than typical values of mid-latitude atmospheric LIDAR measurements, but consistent with polar observations. In addition, two distinct temperature-dependent modes in the relationship between linear depolarization ratio and particle size were found. The measurement results were compared to different numerical simulations, which showed good agreement to the measurement data when different types of morphological complexity (surface roughness, internal scattering, and hollowness) were incorporated into the used optical particle model.

By targeted AIDA experiments with the new Particle Habit Imager and Polar Scattering probe (PHIPS-POL) at cirrus conditions, it was further observed

that the asymmetry parameter of ice particles with sizes predominantly below 70 µm decreased by a mean of 0.03 during particle regrowth in comparison to the initial growth period. Furthermore, it is shown that the growth temperature and relative humidity individually influence the asymmetry parameter.

Besides cloud chamber experiments, the size, shape, concentration, and small-scale morphological complexity of boundary layer ice particles with sizes between 11 µm and 150 µm were measured during multi-week field observations at Dome C. It is found that ice fog events at Dome C are characterised by a smaller particle size mode and an increased mean particle concentration compared to diamond dust and cirrus precipitation events. In addition, the observed ice fog events on the Antarctic plateau had a lower mean particle concentration of $1.0\,\mathrm{L}^{-1}$ and consisted of more pristine ice particles compared to polluted ice fog events observed in Fairbanks, Alaska, with a mean particle concentration of $7.7\,\mathrm{L}^{-1}$.

The results of this work demonstrate how the morphological properties of small ice particles depend on their growth conditions and how these, in turn, influence their optical properties. The findings can be used to support the optimisation of the retrieval algorithms of remote sensing ice cloud measurements. Moreover, they can improve the microphysical and optical parametrisations of cirrus clouds in climate models.

Zusammenfassung

Cirruswolken zählen zu den häufigsten Wolkenarten und haben einen wesentlichen Einfluss auf das Klimasystem. Neben einem kühlenden Einfluss durch die Reflexion der kurzwelligen Sonnenstrahlung haben sie auch einen wärmenden Effekt durch die Absorption der von der Erde emittierten langwelligen Infrarotstrahlung. Damit der Einfluss von Cirruswolken gut in Klimamodellen repräsentiert werden kann, müssen deren mikrophysikalische und optische Eigenschaften genau bekannt sein. Eiskristalle mit Größen unter 70 µm kommen häufig in Cirruswolken vor, doch der Zusammenhang zwischen ihren mikrophysikalischen Eigenschaften (wie Größe und morphologische Komplexität) und ihren optischen Eigenschaften ist bislang unklar.

Diese Arbeit beinhaltet eine Untersuchung des Einflusses der Wachstumsbedingungen auf die Größe und morphologische Komplexität von Eispartikeln mit Größen unter 70 µm in Wolkenkammer-Experimenten und eine Messung und Analyse der mikrophysikalischen Eigenschaften bodennaher Eispartikel auf dem Antarktischen Plateau. Zusätzlich untersucht wird der Einfluss der Wachstumsbedingungen und mikrophysikalischen Eigenschaften auf die optischen Eigenschaften der Eispartikel.

Wolkenkammer-Experimente wurden in der Aerosol Interactions and Dynamics in the Atmosphere (AIDA) Wolkensimulationskammer durchgeführt, um Eispartikel gezielt unter kontrollierten atmosphärischen Bedingungen zu untersuchen. Das gemessene lineare Depolarisationsverhältnis (δ) lag mit Werten unter 0.3 unterhalb typischer Messungen in mittleren Breiten, jedoch im Bereich polarer Beobachtungen. Zwei verschiedene temperaturabhängige Moden zwischen δ und der Partikelgröße wurden zudem bei den Wolkenkammermessungen gefunden. Die Messergebnisse konnten bei hinreichender Berücksichtigung morphologischer Komplexität im Modell des Eispartikels (Oberflächenrauigkeit, interne Streupunkte und hohle Strukturen) mit numerischen Simulationen reproduziert werden.

AIDA-Experimenten unter Cirrusbedingungen mit dem neuen Particle Habit Imager and Polar Scattering (PHIPS-POL) Messgerät zeigten, dass der Asymmetrieparameter von Eispartikeln mit Größen bis ca. 70 µm beim erneuten Wachsen nach einer Sublimationsphase im Mittel um 0.03 kleiner war als während der ersten Wachstumsphase. Darüber hinaus wurde der individuelle Einfluss von Temperatur und relativer Luftfeuchte auf den Asymmetrieparameter charakterisiert.

Neben Wolkenkammer-Experimenten wurden während einer mehrwöchigen Feldmesskampagne auf dem antarktischen Plateau Größe, Konzentration und morphologische Komplexität bodennaher Eispartikel auf Dome C mit Größen zwischen 11 µm und 150 µm gemessen. Diese Messungen zeigten, dass Eisnebelereignisse auf Dome C eine höhere Eispartikelkonzentration und eine kleinere Größenmode haben als Cirrus-Niederschlag und Niederschlag bei klarem Himmel. Die Eispartikelkonzentration während Eisnebelereignissen auf dem Antarktischen Plateau lag mit einem Mittelwert von $1.0\,\mathrm{L}^{-1}$ niedriger als bei anthropogen beeinflussten Eisnebelereignissen in Fairbanks, Alaska, mit einem Mittelwert von $7.7\,\mathrm{L}^{-1}$. Hingegen hatten die in Fairbanks gemessenen Eispartikel einen höheren Grad morphologischer Komplexität.

Die Ergebnisse verdeutlichen, dass Wachstumsbedingungen die Morphologie und damit die optischen Eigenschaften von kleinen Eispartikeln entscheidend prägen. Dies liefert wichtige Grundlagen zur Verbesserung von Fernerkundungsalgorithmen und für die Parametrisierung in Klimamodellen.

Preface

During the course of this PhD project, two manuscripts have been authored as first author and are presently under peer review for publication in scientific journals. Chapter 4 and chapter 5 are based on

- Adrian Hamel et al. "Unique Microphysical Properties of Small Boundary Layer Ice Particles under Pristine Conditions on Dome C, Antarctica". In: EGUsphere 2025 (2025), pp. 1–27. doi: 10.5194/egusphere-2025-3598.
- Adrian Hamel et al. "Cloud Chamber Studies on the Linear Depolarisation Ratio of Small Cirrus Ice Crystals". In: EGUsphere 2025 (2025), pp. 1–32. doi: 10.5194/egusphere-2025-3515.

During the PhD period, the RICE04 AIDA cloud simulation chamber measurement campaign was planned and executed. Furthermore, in-situ field measurements in November and December 2023 at Dome C on the Antarctic plateau were planned and conducted.

The datasets used for analysing the linear depolarization properties in chapter 5 were obtained in the AIDA cloud simulation chamber by principal investigator Dr. Martin Schnaiter before the start of this PhD project. The comparison dataset of the ice fog microphysics in Fairbanks, Alaska, was obtained and provided by principal investigator Dr. Carl Schmitt of the University Alaska Fairbanks.

Generative artificial intelligence (AI) has been used in compliance with the guidelines of the Karlsruhe Institute of Technology[1] and the Faculty of Physics[2]. Grammarly and ChatGPT have been used for grammatical and stylistic improvements of this thesis. ChatGPT has been used for performance optimisation of post-processing scripts.

[1] `https://www.kit.edu/downloads/KI-Leitlinien-de.pdf` (last access on 24 November 2025)
[2] `https://www.imk-tro.kit.edu/english/13269.php` (last access on 24 November 2025)

Contents

Glossary

AIDA Aerosol Interactions and Dynamics in the Atmosphere: Cloud simulation chamber at the Karlsruhe Institute of Technology.

AWS Automated Weather Station: A network of automated weather stations is set up across the Antarctic continent. They measure air temperature, air pressure, wind speed, wind direction, and relative humidity at approximately 3 m above ground level.

Concordia station Italian-French Antarctic research station on Dome C, Antarctica. It opened in 2005 and is one of three research stations in inland Antarctica that is operated year-round.

cpdd Lidar-based combined class of cirrus precipitation and diamond dust events at Dome C Antarctica.

CPI Cloud Particle Imager: Commercial imager of cloud particles from SPEC Inc.

Dome C Ice dome on the Antarctic ice sheet where Concordia station is located.

FTIR Fourier Transform Infrared Spectrometer that is operated in the AIDA cloud simulation chamber using white light. Based on the measured spectra, the particle concentration and size can be derived with assumptions on the particle shape and size distribution for sizes down to 1 µm.

GLCM Grey-Level Co-occurrence Matrix: Speckle texture analysis matrix describing how often pairs of pixels with the same gray-level occur along a given direction separated by a defined distance.

HALO06 Measurement campaign at the AIDA cloud simulation chamber consisting of regrowth experiments of ice particles at cirrus temperatures. It took place in January and February 2011.

IITM Invariant-Imbedding Transfer Matrix: A method to calculate the Transfer matrix. It uses a volume integral equation unlike the previously used surface integral equations and makes it possible to calculate the transfer matrix for particles of larger sizes.

INP Ice Nucleating Particle: Aerosol particle which acts as a nucleus during ice crystal formation.

KIT Karlsruhe Institute of Technology.

LIDAR Light Detection And Ranging: A remote sensing method that determines distances detecting the back reflections of emitted laser pulses. It is commonly used to take profiles of cloud and aerosol particles in the atmosphere.

MCPMT Multi Channel Photo Multiplier Tube: Optoelectronic component that converts light pulses into electric current burst for many channels.

PHIPS Particle Habit Imager and Polar Scattering probe: Combined single particle imager and polar nephelometer.

PHIPS-HALO First airborne version the PHIPS. Designed for the German High Altitude and Long Range Research Aircraft (HALO) Gulfstream G550.

PHIPS-POL Particle Habit Imager and Polar Scattering probe (POLarisation): Second version of the PHIPS with improved angular scattering detection layout, top-head intensity profile of scattering laser beam, and the possibility to measure polarisation properties of the scattered light.

PPD-2K Particle Phase Discriminator mark 2 Karlsruhe edition: Single particle counter and diffraction pattern imager (lab version of SID-3).

RICE Rough ICE: Set of measurement campaigns at the AIDA cloud simulation chamber facility between 2011 and 2023 with the aim to analyse the effects that roughness of cirrus ice crystals has on the light scattering properties.

RICE04 Most recent RICE cloud chamber measurement campaign in October 2023 with the aim to analyse the effects that roughness of cirrus ice crystals has on the light scattering properties measured with the PHIPS-POL instrument.

SID-3 Small Ice Detector mark 3: Single particle counter and diffraction pattern imager for airborne applications.

SIMONE Streulichtintensitatsmessungen zum optischen Nachweis von Eispartikeln - Scattering Intensity Measurements for the Optical Detection of Ice Particles: Instrument that measures the near forward (2°) and the near-backscattering (178°) intensity of light that is scattered by particles inside the AIDA cloud simulation chamber.

T-matrix Transfer matrix: An exact method to calculate light scattering properties of non-spherical particles.

Symbols

Symbol	Unit	Description
A, B	-	Fit parameters for PHIPS-POL gain correction
C_P	-	Complexity parameter
$DOLP$	-	Degree of linear polarisation
DOP	-	Degree of polarisation
G_1, G_2	-	Gain setting of PHIPS-POL MCPMT1 and MCPMT2
G	-	Gain setting of PHIPS-POL MCPMT
$I_\perp, I_\parallel$	$\mathrm{W\,m^{-2}}$	Intensity with polarisation perpendicular and parallel to the scattering plane
I_bg	$\mathrm{W\,m^{-2}}$	Background intensity
I	$\mathrm{W\,m^{-2}}$	Intensity
M_scat	-	Amplitude scattering matrix
M	-	Mueller matrix
N	$\mathrm{L^{-1}}$	Particle concentration
P_D	-	Diffraction part of angular phase function
P_GO	-	Geometrical optics part of angular phase function
P_l	-	Legendre polynomial
P	-	Angular phase function
RH_ice	-	Relative humidity with respect to ice
RH_water	-	Relative humidity with respect to liquid water
RH	-	Relative humidity
T_gas	°C	Gas temperature
T_wall	°C	Wall temperature

Symbol	Unit	Description
T	°C	Temperature
Δx	-	Pixel distance
Ω	-	Solid angle
$\vec{E}$	V/m	Electric field
$\vec{E}$	T	Magnetic field
$\vec{S} = \begin{pmatrix} I \\ Q \\ U \\ V \end{pmatrix}$	-	Stokes vector
$\vec{k}$	1/m	Wave vector
$\vec{x} = \begin{pmatrix} x \\ y \\ z \end{pmatrix}$	m	Position
δ	-	Linear depolarisation ratio
ϵ_0	$\mathrm{F\,m^{-1}}$	Vacuum permeability
$\hat{c_1}$	-	Expansion coefficient
λ	m	Wavelength
AGL		Above ground level
ASL		Above sea level
UTC	s	Coordinated Universal Time in hh:mm DD.MM.YYYY
dN/dlogDp	$\mathrm{cm^{-3}}$	Particle size distribution
ppm		Parts per million
μ_0	$\mathrm{kg\,m\,s^{-2}\,A^{-2}}$	Vacuum permittivity
ω_0	-	Single scattering albedo
ω	$\mathrm{s^{-1}}$	Angular frequency
ϕ	-	Azimuth
ϕ	-	Phase shift
π	-	Ratio of a circle's circumference to diameter
ρ	$\mathrm{C\,m^{-3}}$	Charge density
ρ	-	Polar angle
σ^2	-	Variance of Gaussian distribution
σ_{ext}	$\mathrm{m^2}$	Extinction cross section
σ_{sca}	$\mathrm{m^2}$	Scattering cross section
a, b	-	PPD-2K calibration coefficients

Symbol	Unit	Description
a_l, b_l	-	Mie scattering coefficients
c	$\mathrm{m\,s^{-1}}$	Speed of light
d	m	Diameter
f	-	Exponential fit function for PHIPS-POL gain correction
g_D	-	Diffraction part of the asymmetry parameter
g_{GO}	-	Geometrical optics part of the asymmetry parameter
g	-	Asymmetry parameter
j_l, h_l	-	Bessel functions
j	$\mathrm{A\,m^{-2}}$	Current density
k_e	-	Small-scale complexity parameter
m	-	Relative refractive index
n, n'	-	Refractive index
p		p-value of Pearson correlation coefficient
p	hPa	Pressure
r	m	Radius
t	s	Time
v	$\mathrm{m\,s^{-1}}$	Wind speed
x	-	Size parameter

1. Introduction

The observation of the atmosphere is highly important in our warming climate. It is necessary to understand atmospheric processes and to model the future climate with the highest possible confidence. This is crucial to mitigate climate change and to efficiently adapt to the changing climate.

Since the pre-industrial era, the concentration of the greenhouse gas CO_2 has increased from approximately 280 parts per million (ppm) to over 420 ppm [72]. The simultaneous global mean air temperature increase is nearing and likely soon exceeding the 1.5 °C limit from the Paris agreement [9, 77]. Depending on the measures that will be taken, the global mean temperature is expected to increase between 1.4 °C and 4.4 °C until the end of the century (expected increase of 3.2 °C for current policies) [86, Section 3.1]. Consequences will include increased heavy precipitation and flooding events, more frequent and severe droughts, and more heat waves in many regions globally.

Climate models are developed to estimate the future climate. One key feature of the models is to simulate Earth's radiative budget, which consists of the incoming short wave radiation from the sun, and the short and long wave radiation emitted by Earth into space. Different factors affect the radiative budget, including greenhouse gases, surface albedo, and clouds. Cirrus clouds are the most common cloud type, with a global fraction of 40 % - 50 % [145]. They influence the short wave and the long wave radiation [94, 14, 142]. Yet, the exact short wave radiative forcing of cirrus clouds remains a field of current research [61] and is a major uncertainty in climate modelling [31]. To accurately predict cirrus radiative forcing in climate models, improved knowledge of particle microphysical and optical properties is needed. The diversity of shapes and morphological small-scale complexity of cirrus ice crystals makes this task challenging [69]. Due to limited options of high-resolution imaging for ice particles with sizes smaller than 50 µm, knowledge about the microphysical properties of small ice particles is scarce [76].

Small ice particles with sizes below 50 µm are abundant on the Antarctic plateau [162]. A large part of the precipitation in one of the coldest, driest, and cleanest regions on our planet falls as clear sky precipitation of small ice particles [30, 162]. These small boundary layer ice particles can have a high radiative impact [50]. In situ measurements of atmospheric ice crystals in this remote region are scarce, especially for small ice particles with sizes below 50 µm [55]. The first research question of this work is based on a multi-week in situ measurement campaign of atmospheric ice crystals with sizes between 11 µm and 150 µm at Dome C, Antarctica: **What are the microphysical properties of summer time small boundary layer ice particles at Dome C, and how do they differ in comparison to small boundary layer ice particles in polluted urban regions?**

Along with in situ measurements, remote sensing is a valuable tool to characterise atmospheric cirrus clouds. Light Detection and Ranging (LIDAR) instruments are commonly used to identify and study cirrus because of their distinct linear depolarisation feature in the LIDAR backscattering signal. While the general depolarising effect of cirrus clouds is well known, the link between the backscattering linear depolarisation ratio and the particle microphysical properties is highly complex. The second research question addresses this knowledge gap, analysing 47 expansion cloud experiments performed at the Aerosol Interactions and Dynamics in the Atmosphere (AIDA) cloud simulation chamber facility: **How is the backscattering linear depolarisation ratio linked to small ice particle microphysical properties like size, shape, and morphological complexity and how can this be accurately modelled with state-of-the-art light scattering simulations?**

The optical properties of small ice particles, together with their microphysical properties, are essential for climate modelling. Ice particle optical properties depend on the particle microphysics, which are primarily influenced by relative humidity and temperature during particle growth [6, 8, 69]. A key quantity for characterising the optical behaviour of ice clouds in climate models is the asymmetry parameter [38, 19]. In the atmosphere, however, temperature and humidity typically fluctuate during ice particle formation, making it difficult to isolate their effects on the asymmetry parameter. This challenge motivates a cloud chamber study at the AIDA facility, dedicated to answering the third research question: **How do the growth conditions, such as temperature and relative humidity, influence the asymmetry parameter of cirrus clouds composed of small ice particles?**

This work is organised in the following structure: Chapter 2 provides the physics and atmospheric science background which is needed for the comprehension of this work. Chapter 3 introduces the scientific instruments that were used for the data acquisition. Details of the calibration of the different instruments and the data processing procedures are given. Furthermore, the measurement site at Dome C and the AIDA cloud simulation chamber are described. Chapter 4 analyses the microphysical properties of ice fog and diamond dust boundary layer ice particles at Dome C, measured during a field campaign between November 2023 and January 2024. The results are compared to urban polluted ice fog events at Fairbanks, Alaska, measured with the same instrument in three winters between 2020 and 2022. In chapter 5 the link between the backscattering linear depolarisation ratio and the particle microphysical properties like size, shape, and morphological complexity is analysed based on multiple AIDA measurement campaigns between 2011 and 2014. Chapter 6 analyses the effects of temperature and relative humidity on the asymmetry parameter of cloud chamber grown ice particles using the measurement data from the RICE04 AIDA cloud simulation chamber measurement campaign in October 2023. Finally, a summary of the results is given in chapter 7 with an outlook of future research. Overall, this work focuses on the link between atmospheric conditions, microphysical properties, and optical properties of small atmospheric ice particles with sizes below 70 µm. It aims to reconcile in situ atmospheric observations and laboratory cloud chamber experiments with light scattering simulations.

2. Theoretical background

This chapter provides the theoretical basis for this work, beginning with a description of light and its polarisation property, followed by the process of light scattering. Next, different methods of light scattering simulations are introduced, which will be used in chapter 5. Finally, a general introduction of cirrus clouds, their occurrence, and microphysical properties is given.

2.1. Description of light

2.1.1. Maxwell's equations

In order to understand the processes of light scattering, a theoretical description of light is needed. Light can be described as an electromagnetic wave. As a starting point, we use the four Maxwell equations for electromagnetic fields

$$\vec{\nabla} \cdot \vec{E} = \frac{\rho}{\epsilon_0} \qquad \text{Gauss' law for electricity} \tag{2.1a}$$

$$\vec{\nabla} \cdot \vec{B} = 0 \qquad \text{Gauss' law for magnetism} \tag{2.1b}$$

$$\vec{\nabla} \times \vec{E} = -\frac{\partial \vec{B}}{\partial t} \qquad \text{Faraday's law of induction} \tag{2.1c}$$

$$\vec{\nabla} \times \vec{B} = \mu_0 \vec{j} + \mu_0 \epsilon_0 \frac{\partial \vec{E}}{\partial t} \qquad \text{Ampere's law} \tag{2.1d}$$

with electric field $\vec{E}$, magnetic field $\vec{B}$, charge density ρ, and current density $\vec{j}$. μ_0 is the vacuum permittivity and ϵ_0 is the vacuum permeability. Gauss' law for electricity describes the electric field around enclosed charges. Gauss' law for magnetism states that no magnetic monopoles exist. Faraday's law of induction explains the curl of the electric field around a changing magnetic

field. Ampere's law describes the curl of a magnetic field around a changing electric field or changing current. [25, section 4.6]

2.1.2. The plane wave

For the description of a plane wave in vacuum, we start with Maxwell's equations in vacuum

$$\vec{\nabla} \cdot \vec{E} = 0 \tag{2.2a}$$

$$\vec{\nabla} \cdot \vec{B} = 0 \tag{2.2b}$$

$$\vec{\nabla} \times \vec{E} = -\frac{\partial \vec{B}}{\partial t} \tag{2.2c}$$

$$\vec{\nabla} \times \vec{B} = \mu_0 \epsilon_0 \frac{\partial \vec{E}}{\partial t} \tag{2.2d}$$

using that no charges $\rho = 0$ and no currents $\vec{j} = 0$ exist. Taking the curl of Faraday's law of induction and Ampere's law

$$\vec{\nabla} \times (\vec{\nabla} \times \vec{E}) = -\frac{\partial}{\partial t}(\vec{\nabla} \times \vec{B}) \tag{2.3a}$$

$$\vec{\nabla} \times (\vec{\nabla} \times \vec{B}) = \mu_0 \epsilon_0 \frac{\partial}{\partial t}(\vec{\nabla} \times \vec{E}) \tag{2.3b}$$

and using the identity of a vector $\vec{V}$

$$\vec{\nabla} \times (\vec{\nabla} \times \vec{V}) = \vec{\nabla}(\vec{\nabla} \cdot \vec{V}) - \Delta \cdot \vec{V} \tag{2.4}$$

we obtain the wave equations for the electric and the magnetic field of an electromagnetic wave in vacuum

$$\Delta \vec{E} = \mu_0 \epsilon_0 \frac{\partial^2 \vec{E}}{\partial t^2} \tag{2.5a}$$

$$\Delta \vec{B} = \mu_0 \epsilon_0 \frac{\partial^2 \vec{B}}{\partial t^2} \tag{2.5b}$$

with the propagation speed $c = \frac{1}{\sqrt{\mu_0 \epsilon_0}}$. The wave equation can be solved by a plane wave $\vec{E}(\vec{x}, t)$ with wavelength λ propagating in the direction of the wave vector $\vec{k}$ defined as

$$\vec{E}(\vec{x}, t) = \vec{E}_0 \sin(\vec{k}\vec{x} - \omega t) \tag{2.6}$$

with amplitude of the electric field $\vec{E}_0$, wave number $k = |\vec{k}| = \frac{2\pi}{\lambda}$, angular frequency $\omega = c\frac{2\pi}{\lambda}$, position $\vec{x} = (x, y, z)^T$, and time t. [25, sections 7.1 - 7.3]

2.1.3. Polarisation

Polarisation is a property of light that can be described with the polarisation ellipse. Choosing the coordinate system in a way that the plane wave is propagating in the z-direction, the plane wave is defined as

$$\vec{E}(\vec{x}, t) = E_{0\mathrm{x}}\vec{e_x} \sin(kz - \omega t) + E_{0\mathrm{y}}\vec{e_y} \sin(kz - \omega t - \phi) \tag{2.7}$$

with x-component $E_{0\mathrm{x}}$ and y-component $E_{0\mathrm{y}}$ of the amplitude of the electric field and phase shift ϕ between $E_{0\mathrm{x}}$ and $E_{0\mathrm{y}}$. The polarisation ellipse is the shape which the electric field vector traces for $z = 0$. When there is no phase shift ($\phi = 0$) and thus the amplitude $\vec{E}_0$ points in the same direction at position $\vec{x}$ for all times t, the polarisation is called linear. In this case, the polarisation ellipse is a line. If $\phi = \pm\frac{\pi}{2}$ and $E_{0\mathrm{x}} = E_{0\mathrm{y}}$, the polarisation ellipse is a circle and the polarisation is called circular. In all other cases with defined phase shift ϕ, a plane wave has elliptical polarisation. Light is called unpolarised when the amplitude of the electric field does not point in the same direction for all times t at a position $\vec{x}$ and no constant phase shift ϕ exists between the orthogonal components. The state of polarisation can be described with the Stokes vector $\vec{S} = (I, Q, U, V)^T$.

$$I = I_{0^\circ} + I_{90^\circ} = E_{0\mathrm{x}}^2 + E_{0\mathrm{y}}^2 \tag{2.8a}$$

$$Q = I_{0^\circ} - I_{90^\circ} = E_{0\mathrm{x}}^2 - E_{0\mathrm{y}}^2 \tag{2.8b}$$

$$U = I_{45^\circ} - I_{135^\circ} = 2E_{0\mathrm{x}}E_{0\mathrm{y}} \cos(\phi) \tag{2.8c}$$

$$V = I_{\mathrm{circ,R}} - I_{\mathrm{circ,L}} = 2E_{0\mathrm{x}}E_{0\mathrm{y}} \sin(\phi) \tag{2.8d}$$

where I is the intensity of the light. Q is the intensity of the light passing an ideal polariser at 0° orientation (I_{0°) subtracted by the intensity of the light passing an ideal polariser at 90° orientation (I_{90°) . U is the intensity of the light passing an ideal polariser oriented at 45° (I_{45°) subtracted by the intensity of the light passing an ideal polariser oriented at 135° (I_{135°). V is the intensity of the light with a right-circular polarisation ($I_{\mathrm{circ,R}}$) subtracted by the intensity of the light with a left-circular polarisation ($I_{\mathrm{circ,L}}$). Whereas the polarisation

ellipse can only describe fully polarised light, the Stokes vector can also describe unpolarised and partially polarised light. Exemplary Stokes vectors for unpolarised light ($\vec{S}_{\text{unpol}}$), linearly polarised light with orientations of 0°, 90°, and ± 45° ($\vec{S}_{0°}$, $\vec{S}_{90°}$, $\vec{S}_{\pm 45°}$), and right-circularly/ left-circularly polarised light ($\vec{S}_{\text{circ,R/L}}$) are given below.

$$\vec{S}_{\text{unpol}} = \begin{pmatrix} 1 \\ 0 \\ 0 \\ 0 \end{pmatrix} \quad \vec{S}_{0°} = \begin{pmatrix} 1 \\ 1 \\ 0 \\ 0 \end{pmatrix} \quad \vec{S}_{90°} = \begin{pmatrix} 1 \\ -1 \\ 0 \\ 0 \end{pmatrix} \quad \vec{S}_{\pm 45°} = \begin{pmatrix} 1 \\ 0 \\ \pm 1 \\ 0 \end{pmatrix} \quad \vec{S}_{\text{circ,R/L}} = \begin{pmatrix} 1 \\ 0 \\ 0 \\ \pm 1 \end{pmatrix}$$

The degree of polarisation *DOP* and degree of linear polarisation *DOLP* are defined as

$$DOP = \frac{\sqrt{Q^2 + U^2 + V^2}}{I^2} \tag{2.9a}$$

$$DOLP = \frac{\sqrt{Q^2 + U^2}}{I^2} \tag{2.9b}$$

The Mueller matrix formalism describes how the polarisation state of light changes when interacting with optical components. It describes the relationship between the polarisation state $\vec{S}_{\text{i}}$ of the incident light and the polarisation state $\vec{S}_{\text{t}}$ of the transmitted light with the 4x4 Mueller matrix M

$$\vec{S}_{\text{t}} = M \cdot \vec{S}_{\text{i}} \tag{2.10}$$

An exemplary Mueller matrix of a linear polarisation filter is given as

$$M_{\text{polariser}}(\theta) = \frac{1}{2} \begin{pmatrix} 1 & \cos(2\theta) & \sin(2\theta) & 0 \\ \cos(2\theta) & \cos^2(2\theta) & \cos(2\theta)\sin(2\theta) & 0 \\ \sin(2\theta) & \cos(2\theta)\sin(2\theta) & \sin^2(2\theta) & 0 \\ 0 & 0 & 0 & 0 \end{pmatrix} \tag{2.11}$$

with filter orientation θ. [12, section 2.11.2]

2.2. Light scattering

An electromagnetic wave is altered when it hits a particle. This process is called light scattering for electromagnetic waves in the visible spectrum. The

particle, which is hit by the electromagnetic wave, can be seen as a multitude of electric dipoles. These dipoles start oscillating when they are driven by the electric field of the incident electromagnetic wave. The oscillating dipoles again start radiating electromagnetic waves. This secondary radiation is called the scattered light. Some of the incident radiation can also get transferred to heat through dampening of the dipoles. This process is called absorption. The scattered light that is received at a defined direction is the superposition of the scattered wavelets emitted by the multitude of electric dipoles of the scattering particle. The phase and the amplitude of the scattered light depend on the material of the particle. If the particle is not much smaller than the wavelength of the incident light, the phase difference between the scattered wavelets depends on the particle size, shape, and orientation. [12, sections 1.1 - 1.3]

The scattering properties thus strongly depend on the size parameter

$$x = \frac{2\pi n' r}{\lambda} \tag{2.12}$$

with particle radius or characteristic length r and refractive index of the surrounding medium n' [12, section 4.3.3]. For $x \ll 1$ the scattering is called Rayleigh scattering. For particles with $x \approx 1$ of the incident light the scattering is called Mie scattering, and for $x \gg 1$ the light scattering enters the regime of geometrical optics. In the geometrical optics regime, light can be approximated as a bundle of rays and wave effects like diffraction and interference can be neglected. This approximation is also called geometrical optics approximation. Cirrus ice crystals with sizes from a few to a few hundred µm are in the transition region between Mie scattering and the geometrical optics regime. [25, section 10.9 and 10.10]

2.2.1. Phase function and asymmetry parameter

The intensity of the scattered light as a function of the polar angle θ is called the phase function $p(\theta)$ with normalisation

$$\int_{\phi=0}^{2\pi} \int_{\theta=0}^{\pi} p(\theta) \sin(\theta) d\theta d\phi = 1 \tag{2.13}$$

From the phase function, the asymmetry parameter g can be derived

$$g = \int_{\phi=0}^{2\pi} \int_{\theta=0}^{\pi} p(\theta) \cos(\theta) \sin(\theta) d\theta d\phi \tag{2.14}$$

which is a measure for the symmetry of the scattered light. g is equal to zero for symmetric scattering about an angle of 90°. If more light is scattered in the forward than in the backward direction, g becomes positive. If more light is scattered in the backward direction, g becomes negative. [12, section 3.4]

2.2.2. Mie theory

Mie theory enables us to calculate the scattering properties of spherical particles. Gustav Mie found a solution to Maxwell's equations in vector spherical harmonics with the boundary condition for spherical particles in 1908. The boundary condition is the continuity of the transversal electric field at the particle boundary. The scattering cross section σ_{sca} and the extinction cross section σ_{ext} are given by

$$\sigma_{\text{sca}} = \frac{2\pi}{k^2} \sum_{n=1}^{\infty} (2n+1)(|a_n|^2 + |b_n|^2) \tag{2.15}$$

$$\sigma_{\text{ext}} = \frac{2\pi}{k^2} \sum_{n=1}^{\infty} (2n+1)\text{Re}(a_n + b_n) \tag{2.16}$$

with Mie scattering coefficients a_l and b_l,

$$a_l = \frac{m^2 j_l(mx)[x j_l(x)]' - j_l(x)[mx j_l(x)]'}{m^2 j_l(mx)[x h_l^{(1)}(x)]' - h_l^{(1)}(x)[mx j_l(x)]'} \tag{2.17}$$

$$b_l = \frac{j_l(mx)[x j_l(x)]' - j_l(x)[mx j_l(x)]'}{j_l(mx)[x h_l^{(1)}(x)]' - h_l^{(1)}(x)[mx j_l(x)]'} \tag{2.18}$$

Bessel functions $j_n(x)$ and $h_n^{(1)}(x)$, and relative refractive index $m = \frac{n}{n'}$ with refractive indices of medium n' and particle n. [12, sections 4.1-4.3]

2.2.3. Amplitude scattering matrix

For the scattering problem, a Mueller matrix can be defined that relates the Stokes parameters of the incident light ($\vec{S}_\mathrm{i}$) to the Stokes parameters of the scattered light ($\vec{S}_\mathrm{scat}$). This Mueller matrix is called the amplitude scattering matrix M_scat

$$\vec{S}_\mathrm{scat}(\Omega) = \frac{1}{k^2 r^2} \cdot \begin{pmatrix} M_{11}(\Omega) & M_{12}(\Omega) & M_{13}(\Omega) & M_{14}(\Omega) \\ M_{21}(\Omega) & M_{22}(\Omega) & M_{23}(\Omega) & M_{24}(\Omega) \\ M_{31}(\Omega) & M_{32}(\Omega) & M_{33}(\Omega) & M_{34}(\Omega) \\ M_{41}(\Omega) & M_{42}(\Omega) & M_{43}(\Omega) & M_{44}(\Omega) \end{pmatrix} \cdot \vec{S}_\mathrm{i} \tag{2.19}$$

with solid angle Ω and particle radius or characteristic length r. [12, section 3.3]

Due to the symmetries of an ensemble of arbitrarily shaped particles with random orientation, the amplitude scattering matrix only has six independent entries

$$\vec{S}_\mathrm{scat}(\Omega) = \frac{1}{k^2 r^2} \cdot \begin{pmatrix} M_{11}(\Omega) & M_{12}(\Omega) & 0 & 0 \\ M_{12}(\Omega) & M_{22}(\Omega) & 0 & 0 \\ 0 & 0 & M_{33}(\Omega) & M_{34}(\Omega) \\ 0 & 0 & -M_{34}(\Omega) & M_{44}(\Omega) \end{pmatrix} \cdot \vec{S}_\mathrm{i} \tag{2.20}$$

. [12, section 13.6]

2.2.4. Backscattering linear depolarisation ratio

The backscattering linear depolarisation ratio is an important measurement size for atmospheric light detection and ranging instruments (LIDARs). These instruments send linearly polarised light pulses and separately detect the backscattered intensities of the light with polarisation parallel and perpendicular to the polarisation of the incident light. δ is defined as

$$\delta = \frac{I_{90^\circ}}{I_{0^\circ}} \tag{2.21}$$

with backscattering intensity I_{90° for a polarisation perpendicular and backscattering intensity I_{0° for a polarisation parallel to the polarisation of the incident

light. δ can also be expressed as a function of the Stokes vector of the backscattered light I and Q:

$$\delta = \frac{I - Q}{I + Q} \tag{2.22}$$

using the Mueller matrix of a linear polarisation filter 2.11. Using the amplitude scattering matrix (2.20) elements $M_{11}(\theta)$, $M_{12}(\theta)$, and $M_{22}(\theta)$ for an ensemble of arbitrarily shaped particles with random orientation, δ is defined as

$$\delta(\theta) = \frac{M_{11}(\theta) - M_{22}(\theta)}{M_{11}(\theta) + 2M_{12}(\theta) + M_{22}(\theta)} \tag{2.23}$$

for incident light with linear polarisation parallel to the scattering plane and scattering angle θ. [136]

The bulk scattering linear depolarisation ratio for an ensemble of arbitrarily shaped particles with random orientation is calculated with equation 2.23 using the bulk amplitude scattering matrix elements $\tilde{M_{\mathrm{ii}}}(\theta)$. The $\tilde{M_{\mathrm{ii}}}(\theta)$ are calculated with a size integration of the single size amplitude scattering matrix elements $M_{\mathrm{ii}}(\theta, d)$

$$\tilde{M_{\mathrm{ii}}}(\theta) = \frac{\int_{d_{\min}}^{d_{\max}} M_{\mathrm{ii}}(\theta, d')\, C_{\mathrm{sca}}(d')\, n(d')\, dd'}{\int_{d_{\min}}^{d_{\max}} C_{\mathrm{sca}}(d')\, n(d')\, dd'} \tag{2.24}$$

where $n(d)$ is the particle size distribution and $C_{\mathrm{sca}}(d)$ is the scattering cross section [121].

LIDARs record profiles of the atmosphere from the backscattered intensity, which is proportional to the backscattering cross section and the concentration of particles in the atmosphere. The main feature of δ is that it holds information about the shape of the particle. Spherical particles have a backscattering linear depolarisation ratio of $\delta = 0$ and non-spherical particles have a linear depolarisation ratio of $\delta > 0$ [164].

2.3. Light scattering simulations of complex shaped ice particles

The light scattering properties of complex particles cannot be calculated with Mie theory. Therefore, other methods are needed. For ice crystals in

the geometrical optics regime, ray tracing methods are widely used. The geometrical optics approximation is accurate for particles with sizes that are much larger than the wavelength of the incident light [100]. Usually, a lower size limit of size parameters between 50 - 100 is applied for ray tracing simulations of non-spherical particles [92]. For smaller particles, the geometrical optics approximation does not hold. Thus, numerically exact methods are used that solve Maxwell's equations for the given particle shape. Common methods include the Transition matrix (T-matrix) method [109], the discrete-dipole approximation (DDA) method [32], the finite-difference time domain (FDTD) method [177], and the pseudo-spectral time domain (PSTD) method [115]. The disadvantage of these numerically exact methods is the increase in computational effort with increasing particle size.

2.3.1. Ray tracing simulations

During the process of ray tracing, the propagation of individual rays is simulated. In the geometrical optics approximation, the incident light can be seen as a bundle of rays [177]. Rays hitting the particle undergo refraction and reflection according to Fresnel's law. Rays passing the particle undergo diffraction.

In this work, the conventional geometrical optics ray tracing method by [98] is applied. It uses the tilted facet method to model ice crystal morphological complexity. This method applies a random tilt to the facet when a ray hits. Then, the refracted and the reflected ray are calculated according to Fresnel's law. The distribution of the random tilt around the facet normal simulates different degrees of morphological complexity. Nevertheless, the widely used tilted facet method is a non-physical approach because no well-defined particle surface is used [69]. The lack of a well-defined ice particle surface impedes relating the tilted facet method to any type of morphological complexity that is observed in atmospheric ice crystals [92]. A second way to implement ice crystal morphological complexity in this conventional geometrical optics ray tracing method is the addition of internal scatterers, which are defined by the mean free path and the single scattering albedo. The mean free path is the mean distance that a ray propagates before its direction is changed due to an internal scatterer. The single scattering albedo describes the absorption during the internal scattering process. Internal scatterers can be, for example, non-absorbing air bubbles or soot particles.

2.3.2. T-matrix simulations

T-matrix simulations give exact solutions of Maxwell's equations [109]. They express the electromagnetic field of the incident and scattered light as a series of vector spherical harmonics. The dependence between the incident and scattered field is described by the transition matrix (T-matrix), which solves Maxwell's equations with the boundary conditions of the continuity of the transverse electric field at the edge of the particle. The T-matrix has the advantage of being independent of the direction of the scattered and the incident light. Therefore, once calculated, it enables one to quickly derive the scattered light for any direction of the incident and scattered light. The disadvantage of the T-matrix method is that the computational effort for large particle sizes or aspect ratios strongly increases. The T-matrix code by [109] is used in this work with a python wrapper by [87]. The simulations can be used for spheroids with size parameters up to approximately 50 depending on the used aspect ratio. However, the T-matrix method of [109] has no implementation of surface roughness, hollowness, or internal scattering.

Another method, which is used in this work, is the Invariant-Imbedding T-matrix (IITM) method by [120]. The used dataset contains hexagonal particles with size parameters of up to 316. The IITM method uses a volume integral equation, in contrast to the previously used surface integral equations [10]. Using an additional separation of variables method, it allows calculating the T-matrix for larger sizes than previously possible. This method furthermore simulates ice particle surface roughness, which is modeled with a two-dimensional Gaussian distribution of local planar surface slopes with a variance σ^2.

2.4. Cirrus clouds

Cirrus are clouds consisting of ice particles. The ice particles have complex shapes that depend on different factors such as temperature, humidity, and the concentration of ice nucleating particles [6]. Cirrus generally have lower particle concentrations and larger particle sizes in comparison to liquid clouds. Cirrus particle concentrations roughly range from below $0.01\,\mathrm{L}^{-1}$ to a few L^{-1} [80], while liquid cloud particle concentrations tend to range between $10\,\mathrm{L}^{-1}$ and a few hundred L^{-1} [104]. Cirrus particle sizes can range from a

Figure 2.1.: Cirrus clouds above Mount Cook in New Zealand on 8 December 2023.

few micrometers to >100 µm [80], whereas liquid cloud particle sizes usually range between approximately 4 µm and 20 µm [104]. The parameters largely vary depending on temperature, humidity, and aerosol concentration. Furthermore, cirrus are optically thinner than liquid clouds with an optical depth of usually below one [56, 52], in comparison to liquid clouds that can

reach an optical thickness of more than 100 in deep convection [149]. The global cirrus cloud coverage is estimated between 16.8 % using satellite-borne LIDAR measurements [126] and up to 42 % using satellite-borne infrared radiation sounders [172]. More recent satellite observations estimate a global cloud cover of approximately 70 %, of which approximately 40 % are cirrus clouds [145, 146]. The large difference in the estimated global cirrus cloud coverage can be attributed to different detection thresholds for thin cirrus. Cirrus can occur through different pathways [79]. In situ origin cirrus form directly from the gas phase through vapour deposition at temperatures above the homogeneous freezing threshold of approximately -38 °C, whereas liquid origin cirrus develop from liquid water droplets that freeze when transported to regions with temperatures below the homogeneous freezing threshold. Liquid origin cirrus have a higher ice water content and particle concentration than in situ cirrus.

Furthermore, cirrus radiative properties are a major contribution to Earth's radiative budget [102, 168]. Uncertainties in these parameters play an important role in the overall uncertainty of climate modelling [13]. The generally complex-shaped ice particles make radiative simulations more challenging than for liquid clouds consisting of spherical droplets [69]. The radiative effect of cirrus depends on their formation path [80]. In situ origin cirrus tend to have a slight warming effect, whereas liquid origin cirrus tend to have a strong cooling effect due to their higher optical thickness [80]. Cirrus microphysical and optical properties remain a field of current research.

2.4.1. Ice fog and diamond dust

Small boundary layer ice particles can be separated into ice fog and diamond dust [49]. Ice fog consists of suspended ice particles in the atmosphere [3, 171]. An example photograph from Dome C, Antarctica, is shown in Fig. 2.2a. Ice fog can form at temperatures below -20 °C, typically in Arctic and Antarctic regions, and can significantly reduce visibility [134, 55]. Therefore, it is a threat for transportation. Ice fog forms through the freezing of water droplets or through water vapour deposition on ice nucleating particles (INP) [55]. Ice fog has a strong radiative effect because it influences the heat and moisture budget of the atmosphere [50]. The nucleation processes, microphysical properties, and optical properties of ice fog are a field of current research, especially on the Antarctic plateau [154].

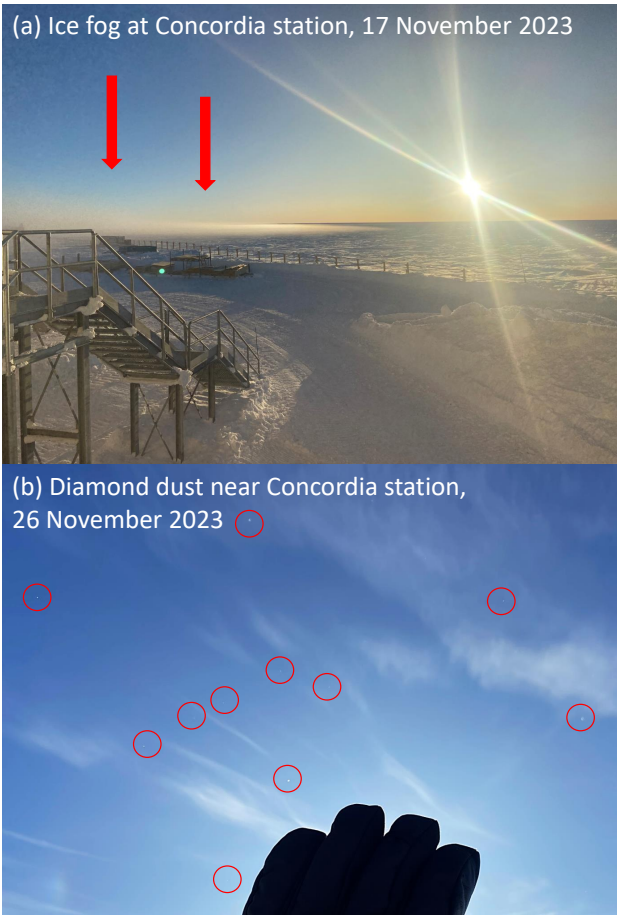

Figure 2.2.: a) Ice fog near Concordia station on 17 November 2023. **b)** Diamond dust particles photographed near Concordia station on 24 November 2023. The particles are highlighted with red circles.

Diamond dust is defined as frozen clear sky precipitation [2, 170]. It contributes approximately 40 % to the precipitation on the Antarctic plateau [30]. Exemplary diamond dust particles imaged during a diamond dust event at Dome C are seen as white dots inside the red circle markers in Fig. 2.2b. Diamond dust differs from ice fog through higher visibility, lower particle

Table 2.1.: Ice fog and diamond dust particle concentration and particle sizes according to the commonly used definition by [49].

	Particle concentration in L^{-1}	Particle mean diameter in µm
Ice fog	$> 1 \cdot 10^3$	<30
Diamond dust	$< 4 \cdot 10^3$	>30

concentration, and higher particle size. However, the separation between the diamond dust and ice fog events is not always clear [55]. A commonly used parametrisation of particle concentration and particle size of ice fog and diamond dust is given in table 2.1.

2.4.2. Halo phenomena

Cirrus clouds often show a visible ring at approximately 22° around the sun, called a 22° halo. An exemplary photo of a bright 22° halo around the sun is shown in Fig. 2.3a, taken near Concordia station, Antarctica. The 22° halo is the most common halo phenomenon. The intensity maximum occurs for light that is scattered by pristine hexagonal ice particles. The path that the light takes leading to the intensity maximum at a polar angle of 22° is shown in Fig. 2.3b. The ring appears through the random orientation of the ice crystals. If there is a larger fraction of horizontally aligned ice crystals, sun dogs appear as bright spots left and right of the sun on the 22° halo. Sun dogs are also seen in Fig. 2.3a. [25, p. 10.10.2]

2.4.3. Nucleation of ice particles

Two pathways exist for the nucleation of ice particles (see Fig. 2.4) [75]. The first pathway is heterogeneous nucleation, when ice particles freeze assisted by an ice nucleating particle. Multiple mechanisms of heterogeneous freezing exist. Immersion freezing describes the freezing of a liquid droplet due to the composition of its immersed condensation nuclei. If a supercooled liquid droplet freezes when it comes in contact with an ice nucleating particle, the process is called contact freezing. Deposition freezing describes the direct transfer of water vapour on the surface of the ice nucleating particle.

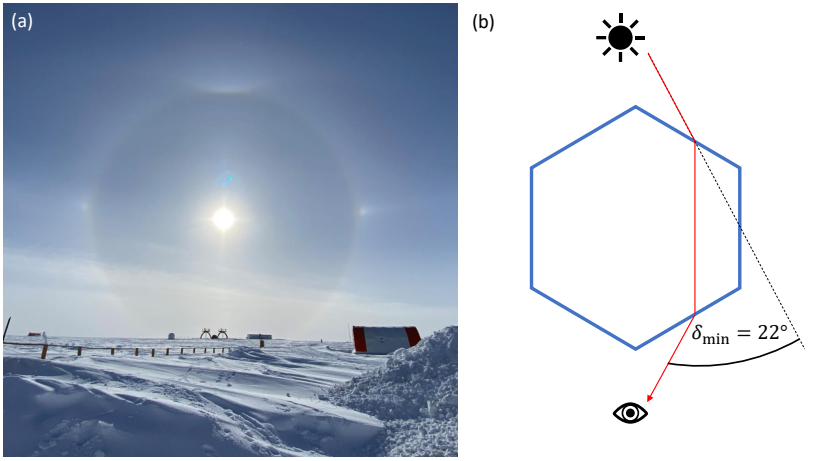

Figure 2.3.: (a) 22° halo photographed near Concordia station on 21 November 2023. Also visible are the circumzenithal arc above the 22° halo and the sun dogs as intensity maxima on the 22° halo at the height of the sun. **(b)** Light path in an hexagonal ice crystal that is responsible for the 22° halo.

The second pathway is homogeneous freezing, when supercooled liquid droplets freeze spontaneously at a temperature below approximately -38 °C [61]. The exact temperature depends on the droplet size and water activity [78].

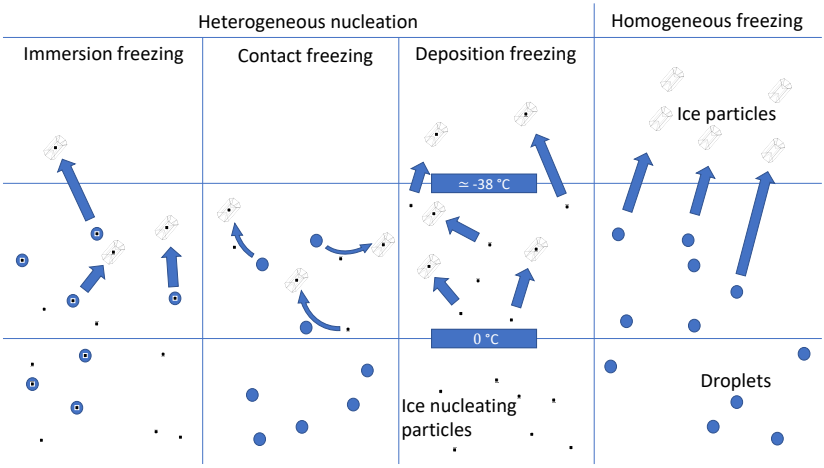

Figure 2.4.: Schematic pathways of ice nucleation in the atmosphere [75].

3. Methods and instrumentation

In this chapter, the particle imager and polar nephelometer PHIPS-POL, the single particle counters and diffraction pattern imagers PPD-2K and SID-3, and the LIDAR-like SIMONE instrument are introduced. These are the primary instruments used in this work. Furthermore, the setup of the instruments for the laboratory and field measurements and the data processing are detailed. Finally, the AIDA cloud simulation chamber facility at Karlsruhe Institute of Technology (KIT) and the measurement site Concordia station at Dome C, Antarctica, are introduced.

3.1. Particle Habit Imager and Polar Scattering probe (PHIPS-POL)

3.1.1. Instrument description

The Particle Habit Imaging and Polar Scattering probe (PHIPS) is an airplane underwing probe capable of producing microscopic stereo images and simultaneously measuring the corresponding angular scattering functions of single particles in a size range between approximately 20 µm and 700 µm [1, 137, 161]. The instrument is a combined single particle imager and nephelometer. The PHIPS-Polarisation (PHIPS-POL) is the newest version of the PHIPS instruments. A photo of the instrument in the laboratory can be seen in Fig. 3.1. The instrument has improvements and new features in comparison to the original PHIPS-HALO. The instrument is used for the data acquisition of chapter 6. We will start with an explanation of the measurement principle of both instruments and continue with the instrument setup of PHIPS-POL, highlighting the differences to PHIPS-HALO.

In both instruments, the particles cross a laser beam that is perpendicular to the particle flux (see schematics in Fig. 3.2). Individual particles are recorded

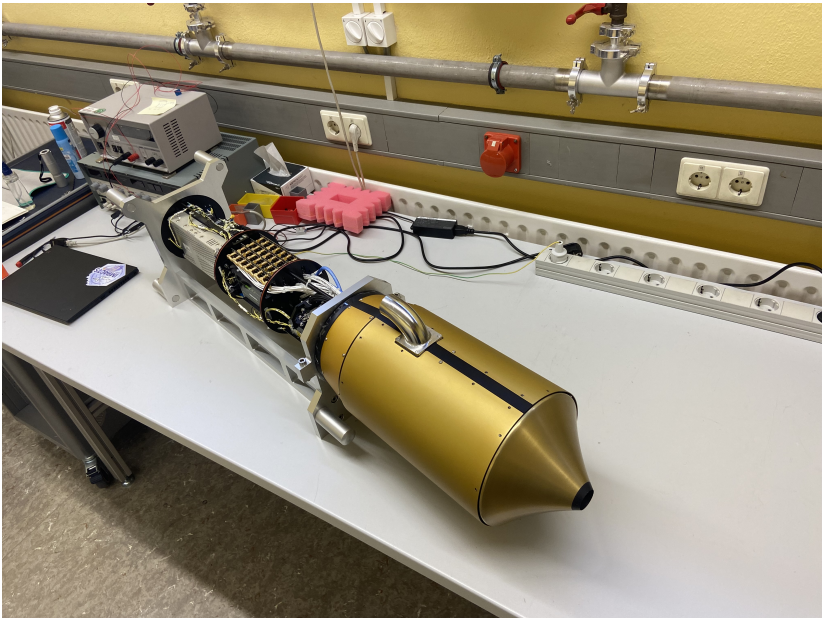

Figure 3.1.: PHIPS-POL in the laboratory.

by peaks in the light that is scattered in the direction of the trigger detector, which is placed at a polar angle of 90° with reference to the laser beam. The trigger detector is azimuthally tilted 32° out of the scattering plane of the nephelometer detector ring. When a particle is detected, the nephelometer measurements record the scattered light with off-axis parabolic mirrors at equidistant spacing of 8° at a radial distance of 83 mm from the scattering center. A particle detection, furthermore, induces two stereoscopic images to be taken of the particle with camera telescope arrays, separated by an angle of 120°. The luminosity is provided by a pulsed laser.

PHIPS-POL uses a continuous wave OBIS LS 532 nm 150 mW optically pumped semiconductor laser as the light source for the scattering measurements, instead of the solid-state laser used in PHIPS-HALO. This allows for a more stable power output, a shorter start-up time, and quick adjustments of the output power. Instead of using a spherical Gaussian beam intensity profile with 0.8 mm $1/e^2$ beam diameter (used in the original PHIPS-HALO),

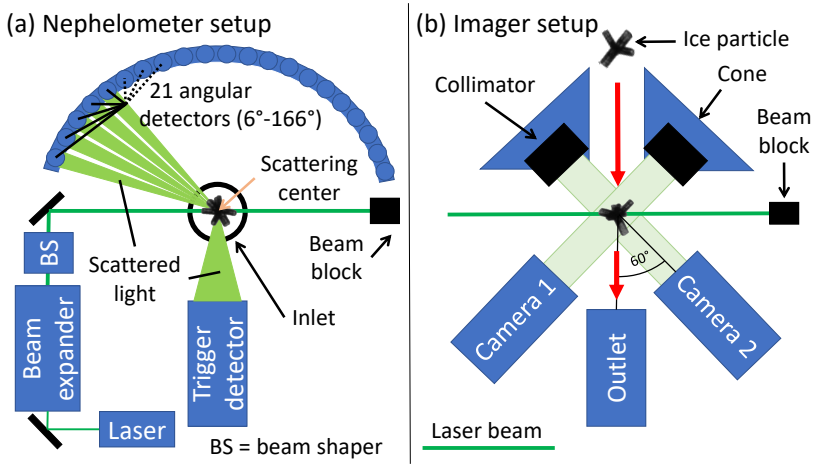

Figure 3.2.: **(a)** shows the schematic setup of the nephelometer of PHIPS-POL. The schematic setup of particle imager of PHIPS-POL is shown in **(b)**.

a horizontally top-hat shaped beam intensity profile with a $1/e^2$ beam width of 0.4 mm at the scattering center is produced with beam shaping optics. In the vertical direction, the beam has a Gaussian intensity profile with a $1/e^2$ beam height of 3.5 mm. The setup uses a TOPAC 10x beam expander in combination with a TOPAC Top-Hat beam shaper GTH-3.6, a cylindrical lens with a focal length of $f = 250$ mm, and a cylindrical lens with a focal length of $f = 1000$ mm. The beam shaping applied in PHIPS-POL enables a near constant laser intensity over the full sensing area. This allows for a better-defined sensing area than for PHIPS-HALO. A wave plate can be added to change the polarisation of the incident light in PHIPS-POL.

The sensing volume is the overlap between the scattering laser and the trigger detector field of view. Using a GeSIM piezo electric droplet generator with droplets of diameters of (27 ± 2) µm the sensing area is measured to $(0.0095 \pm 0.0005)\,\mathrm{cm}^2$ for PHIPS-POL compared to $0.0018\,\mathrm{cm}^2$ for PHIPS-HALO [137]. The limit of the sensing area is defined as the position where the trigger intensity is reduced to 10 % of its peak value. The larger sensing area of PHIPS-POL is also an effect of the altered beam profile in comparison to PHIPS-HALO.

The angular layout of the off-axis parabolic mirrors is changed for PHIPS-POL. 21 off-axis mirrors are located on the upper hemisphere at a radial distance of 83 mm at polar angles between 6° and 166° with an equidistant spacing of 8°. This detector layout has the advantage of better detection of the near forward scattering characteristics as well as probing the HALO angles of 22° and 46°. An additional 16 off-axis parabolic mirrors are located with equidistant spacing of 8° at a radial distance of 83 mm between 46° and 166° on the lower hemisphere (not shown in the schematics). Furthermore, the possibility to add polarisation filters to the angular positions is implemented. This enables the potential to measure the fraction of scattered light that has a polarisation parallel or perpendicular to the scattering plane.

A measurement takes place when the intensity of scattered light detected by the trigger optics is above a set threshold. The light that is collected by the parabolic off-axis mirror is converted into a voltage pulse proportional to the intensity using a multichannel photomultiplier (MCPMT). The nephelometer measurements are peak detection. Instead of one MCPMT with 32 channels (setup of the original PHIPS-HALO), two Hamamatsu H10515B-200 MCPMTs with 16 channels each are used in PHIPS-POL. They enable different gain settings for different angular positions and thus a larger intensity range where the angular phase function can be measured. The calibration of the two MCPMTs relative to each other is detailed in appendix C.1.2. The electric signal is amplified and digitized with automated background subtraction to a number between 0 and 2047 where 2047 is equivalent to the maximum output voltage of the MCPMT of 12 V. The maximum count rate is 6 kHz. A small part of the intensity that is detected in one channel can crosstalk to the neighbouring channels. This is typically below 3 % according to the manufacturer's specifications [57]. The crosstalk is characterised in appendix C.1.1.

The imaging setup of PHIPS-POL is identical to PHIPS-HALO (see Fig. 3.2). Two camera telescope arrays with Allied Vision Prosilica GC 1380H CCD cameras take images of the particles with a resolution of 1360 x 1024 pixels. Fig. 3.3a-h show example stereoscopic images, which were taken with PHIPS-POL during measurement campaign RICE04 at the AIDA cloud simulation chamber. The camera maximum imaging rate is 30 Hz, but limited to 10 Hz by image processing limitations of the computer. The illumination of the images is provided by a custom fiber-coupled incoherent Cavitar laser emitting pulses with a pulse length of 10 ns at a wavelength of 640 nm. The light is directed to the two cameras through two fiber-connected condensers. The laser is set to

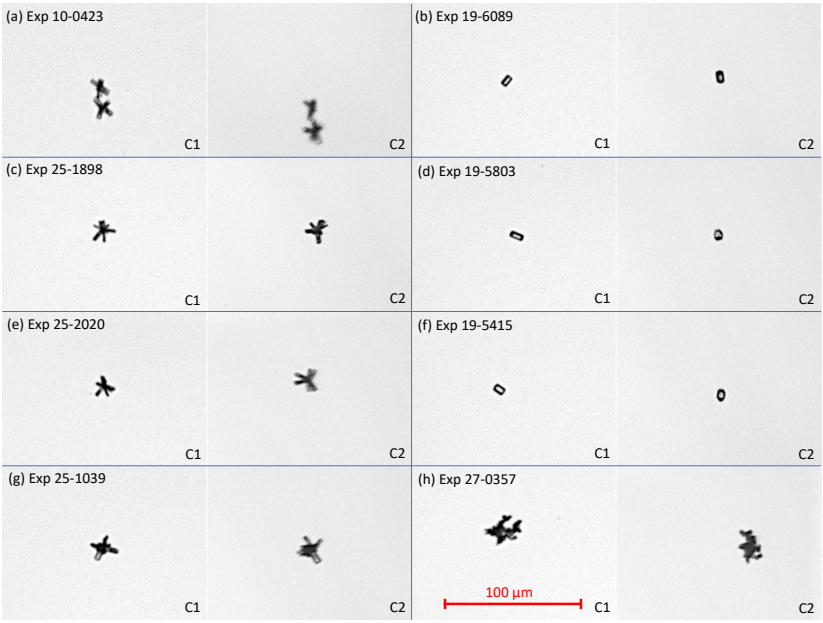

Figure 3.3.: (a)-(h) show example stereoscopic images of ice crystals taken with PHIPS-POL during measurement campaign RICE04 at the AIDA cloud simulation chamber.

flash with a fixed delay of 5 ms when a particle is recorded in the sensing area by a recorded trigger intensity above the set threshold. The viewing angle between the two cameras is 120° and the maximum pixel resolution is 1.61 µm. The optical resolution of the NAVITAR Zoom 6000 telescopes of type 'None + 6.5X Zoom + 2.0x' with a working distance of 92 mm is 4.7 µm at the highest magnification of 9 according to the specifications of the manufacturer. This was confirmed with a 1951 USAF Resolution target placed in the sensing area of the instrument. It was possible to resolve lines down to a resolution of 5.5 µm and 6.2 µm for camera 1 and camera 2, respectively, at a magnification of 8. The field of view is approximately 2.2 mm x 1.6 mm at the standard zoom setting of four with a pixel-to-size relation of

$$1\,\text{pixel} \triangleq \frac{6.45}{2 \cdot M}\,\mu\text{m} \tag{3.1}$$

where M is the magnification setting of the camera telescope array.

Figure 3.4.: Integration of PHIPS-POL in a vacuum cannister (black cylinder) in the AIDA cloud simulation chamber. The picture was taken during the RICE04 measurement campaign.

3.1.2. Integration in the AIDA cloud chamber

During measurements at the AIDA cloud simulation chamber facility, PHIPS-POL was mounted in an upright position in a sealed canister (see Fig. 3.4). The canister is placed below the cloud chamber within the insulated housing of the cloud chamber where the temperature is approximately the same as the temperature inside the cloud chamber at static operation. The cannister

is connected to the cloud chamber with a vertical, straight stainless steel sampling tube with an inner diameter of 10 mm. Inside the cloud chamber the sampling line ends in an upward-facing horn that is shaped in a specific way to minimise sampling artifacts. The lower end of the line ends approximately 10 mm in front of the sensing area of PHIPS-POL. The exhaust of PHIPS-POL was connected with a valve and a mass flow controller to the cloud chamber vacuum system. PHIPS-POL was operated with a mass flow rate of 50 standard liters per minute (standard $\mathrm{L\,min^{-1}}$), resulting in a particle speed of approximately $11\,\mathrm{m\,s^{-1}}$. Standard liters refer to liters at standard conditions of a temperature of 20 °C and a pressure of 1013.25 hPa.

3.1.3. Channel-to-channel calibration with polystyrene microspheres

The individual amplification of the different angular positions of PHIPS can differ slightly. This is due to possible small differences in fiber-coupling efficiency and to varying amplification of the photomultiplier channels. According to Hamamatsu, the channel-to-channel amplification difference can be up to 1:2 [57]. These differences are corrected with a set of calibration factors. The calibration factors can be determined by measuring spherical particles like droplets or polystyrene microspheres because spherical particles with a known size and refractive index allow the calculation of the angular phase function with Mie theory.

In this work, DRI-CAL^{TM} polystyrene DVB microsphere standards from Thermo Scientific with particle diameters of $(20.0 \pm 1.9 \pm 0.9)$ µm and $(49.4 \pm 3.5 \pm 1.6)$ µm are used for the calibration. The first uncertainty is the standard deviation of the individual beads and the second uncertainty is the measurement uncertainty in the mean diameter of the ensemble of beads of the used bottle, both specified by the manufacturer. Dispersed in an air flow, the microspheres are blown into the PHIPS-POL sensing area with a speed of approximately $20\,\mathrm{ms^{-1}}$. Fig. 3.5 shows an example angular scattering function of a polystyrene microsphere with a diameter of $(20.0 \pm 1.9 \pm 0.9)$ µm in comparison to the linearly scaled theoretic scattering function calculated with Mie theory using a refractive index of 1.59. The incident light is linearly polarised with an orientation parallel to the scattering plane. No polarisation filters are mounted on the angular detectors. Calibration factors are obtained by dividing the intensity per channel calculated with Mie theory by 67 intensity

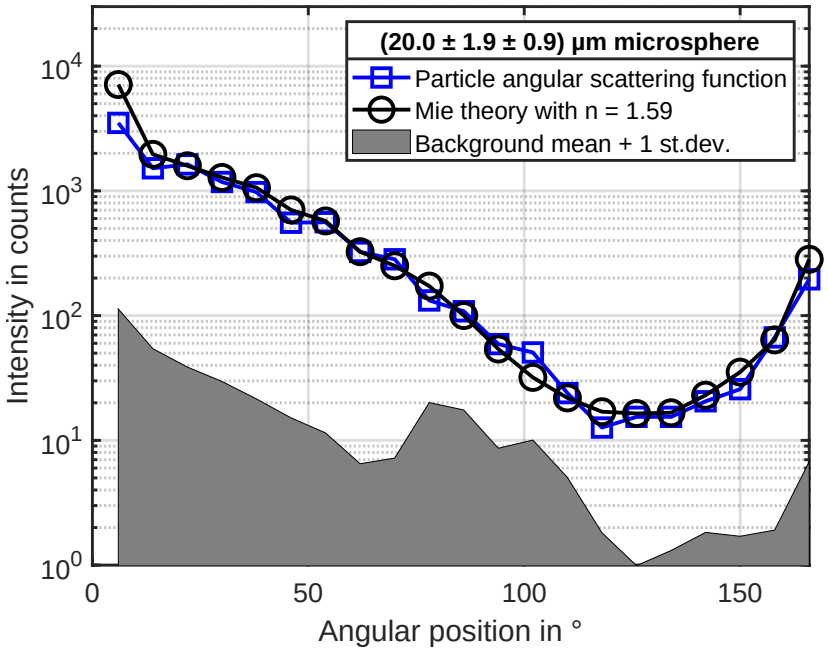

Figure 3.5.: Angular scattering function of a $(20.0 \pm 1.9 \pm 0.9)$ µm polystyrene microsphere with gain 115 on MCPMT1 and gain 95 on MCPMT2 in blue (Image 15 of 23 October 2025). The first uncertainty is the standard deviation of the individual beads and the second uncertainty is the measurement uncertainty in the mean diameter of the ensemble of beads of the used bottle both specified by the manufacturer. In black linearly scaled scattering function calculated with Mie theory using a diameter of 20.0 µm and a refractive index of 1.59. In grey the mean background (after the automated background subtraction) plus one standard deviation from nephelometer measurements is shown.

measurements of polystyrene microspheres (see Fig. 3.6). The measurements are conducted with gain settings of 115 and 95 for MCPMT1 and MCPMT2, respectively. Only individual particles with clear images, where no defects are seen on the microspheres, are used for the calculation of the calibration factors, which are applied to the measurement data of the RICE04 campaign presented in chapter 6 and in appendix C.2.2.

It can be noted that, except for the 6° angular position, all other angular positions are within the typical channel-to-channel gain differences specified by the manufacturer. The 6° detector is located at an angle close to the

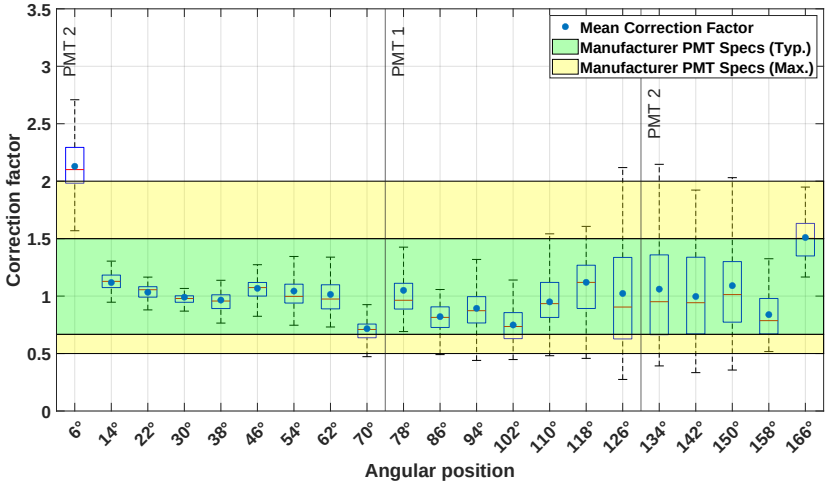

Figure 3.6.: PHIPS-POL channel-to-channel calibration factors determined for the 21 angular positions of the nephelometer measurements from 67 phase functions of $(20.0 \pm 1.9 \pm 0.9)$ µm and $(49.4 \pm 3.5 \pm 1.6)$ µm polystyrene microspheres. The first uncertainty is the standard deviation of the individual beads and the second uncertainty is the measurement uncertainty in the mean diameter of the ensemble of beads of the used bottle both specified by the manufacturer. The typical range of channel-to-channel amplification differences is added as a green and and the maximum range as a yellow box [57]. The deviation of the 6° angular position is caused by effects of diverging stray light from the continuos-wave light source that enters this angular position close to the laser beam. The 6° position is not used for the data analysis in this work.

laser beam. The PHIPS-POL specific beam shaping optics increase the beam divergence in comparison to the original PHIPS-HALO setup with a Gaussian laser beam. This leads to an increased intensity background at the 6° position. The background is subtracted in the PHIPS-POL electronics but, due to the high intensity of the stray light, it is possible that the intensity measurements of the 6° angular position are altered. Therefore, the data analysis in chapter 6 uses the angular scattering function between 14° and 166°. Nonetheless, the results for the angular scattering function between 6° and 166° are provided in appendix C.2.2. A better focusing of the laser beam at the position of the beam dump needs to be implemented for future measurements.

3.1.4. PHIPS-POL data processing during the RICE04 campaign

Nephelometers measure the intensity of the angular scattering function at a limited number of angular positions. Therefore, assumptions on the form of the angular scattering function need to be made to determine the asymmetry parameter g. This work uses the method of [173] where g and the complexity parameter C_P are retrieved from a fit of a series of Legendre polynomials to the mean angular scattering function of the PHIPS-POL nephelometer measurements using the following procedure.

Firstly, the angular scattering function $P(\theta)$ is expanded as a series of Legendre polynomials [167]

$$P(\theta) = \sum_{i=0}^{\infty} (2l+1)\hat{c_l} P_l(cos(\theta)) \tag{3.2}$$

with Legendre polynomials $P_l(cos(\theta))$ and expansion coefficients $\hat{c_l}$

$$\hat{c_l} = \frac{1}{2} \int_{-1}^{1} P(\theta) P_l(cos(\theta)) d(cos(\theta)) \tag{3.3}$$

of degree l. When using a normalisation of

$$\int_0^{2\pi} \int_0^{\pi} P(\theta) sin(\theta) d\theta d\phi = 4\pi \tag{3.4}$$

the asymmetry parameter g is the first moment

$$\hat{c_1} = g \tag{3.5}$$

of the angular scattering function expanded as Legendre polynomials. For particles that are large compared to the wavelength of the incident light, the geometrical optics approximation holds and the scattering phase function can be seen as two separate contributions, the diffraction part P_D and the geometrical optics refraction and reflection part P_{GO}

$$P(\theta) = \frac{1}{2\omega_0} ((2\omega_0 - 1) P_{GO}(\theta) + P_D(\theta)) \tag{3.6}$$

with single scattering albedo ω_0 [99, 176]. Both parts contribute asymptotically equally for particles in the geometrical optics approximation [180]. Applying the Legendre expansion 3.2, g can be expressed as

$$g = \frac{1}{2\omega_0} ((2\omega_0 - 1) g_{GO} + g_D) \tag{3.7}$$

for $l = 1$ with geometrical optics contribution $g_{GO} = \hat{c}_{GO,1}$ and diffraction contribution $g_D = \hat{c}_{D,1}$. An empirical function based on scalar diffraction theory is used to determine g_D

$$g_D(d) = -5.9270 \cdot 10^{-5} - 0.00130 \cdot ln(d) - 0.01087 \cdot (ln(d))^2 + 0.04093 \cdot (ln(d))^3 + 0.94029 \cdot (ln(d))^4 \quad (3.8)$$

for the size of a spherical aperture d and a wavelength of the incident light of 532 nm [173]. The retrieval error is determined to be less than 0.01, taking into account the error from the geometrical optics approximation for particles larger than 26 µm at a wavelength of 532 nm and the error from the approximation of the angular phase function as a series of Legendre polynomials with a degree of 14 [173].

The complexity parameter C_P

$$C_P = (\sum_{l=0}^{\infty} |\hat{c}_l|)^{-1} \quad (3.9)$$

is derived from the Legendre expansion of the angular scattering function. C_P is a measure of the smoothness of the scattering function and correlates with the ice particle complexity in ray tracing simulations [173]. Pristine hexagonal ice particles show halo peaks on the angular scattering function, resulting in a low C_P value, while complex ice particles show a smooth scattering function, resulting in a higher C_P value. For isotropic scattering $C_P = 1$ and for no scattering $C_P = 0$. Furthermore, C_P is a measure of the accuracy of the retrieval of g. More details are given in section 6.9.

The measurement uncertainty of g from the measurement uncertainty of the nephelometer measurements is determined with a Monte Carlo method. For the estimation of the measurement uncertainty, 1000 sets of channel-to-channel correction factors are determined, where the value of each correction factor is chosen randomly from a normal distribution around the mean value of the correction factor. The standard deviation of the normal distribution is the standard deviation of each correction factor according to the microsphere calibration measurements. With the 1000 sets of correction factors, 1000 angular scattering functions are calculated. For each of the angular scattering functions, g and C_P are determined. The standard deviation of this set of 1000 g and C_P values is used as the measurement uncertainty of the retrieved g and C_P values.

During AIDA operation the particle flow speed was approximately 11 m s^{-1}, resulting in a particle residence time of approximately 36 µs in the sensing volume with a depth of 0.4 mm. This is much longer than during airborne operation, where particle flow speeds exceed 100 m s^{-1}. Therefore, it was occasionally observed during the laboratory and cloud chamber operation that individual particles triggered multiple times and were recorded as multiple scattering events. To avoid counting individual particles multiple times, in this campaign only angular scattering functions of imaged particles are used for the data analysis. The camera count rate is limited to 10 Hz using a post trigger delay of 100 ms. This is much longer than the residence time of the particle in the sensing volume of approximately 36 µs and thus multiple triggers on the same particle are avoided.

For the retrieval of g and C_P in this work, the mean of the calibrated angular scattering functions and the mean of the maximum dimension of 50 imaged scattering events with no saturated channels are used. When a particle group with more than 50 particles is analysed, g and C_P are calculated for sets of 50 consecutive particles and the mean values of g and C_P are calculated. To take into account different gain settings and laser power settings during different experiments, all scattering functions are normalized to a gain of 105 on the MCPMT1 and a laser power of 50 mW. This is relevant for the analysis of a mean angular scattering function of individual ice particles from different experiments. The particle maximum dimension and the aspect ratio are determined by an algorithm based on [139]. The aspect ratio is determined as the maximum dimension of the particle divided by the maximum dimension orthogonal to the particle's maximum dimension. To obtain the values closest to the real particle shape, the higher value of the maximum dimensions and the lower value of the aspect ratios from the two stereoscopic camera images are used.

3.2. Particle phase discriminator (PPD-2K) and Small Ice Detector (SID-3)

The Particle Phase Discriminator mark 2 Karlsruhe edition (PPD-2K) and the Small Ice Detector mark 3 (SID-3) are single-particle counters with the additional feature to take images of particle diffraction patterns [156, 73, 76]. Both instruments have the same working principle. The particles are

counted by the light that they scatter when crossing a laser beam, while simultaneously images of the diffracted light are taken. The instruments are used in chapters 4 and 5 to measure the particle concentration and derive information about the particle shape and small-scale complexity.

SID-3 and PPD-2K use a 100 mW frequency-doubled Nd:YAG CrystaLaser at a wavelength of 532 nm as a light source and a Photek ICCD218 camera with an image intensifier for the diffraction pattern imaging. The trigger design differs for both instruments. SID-3 is an underwing airplane probe and thus uses an open path geometry with two nested trigger optics with half angles of 9.25°, which are aligned at 50° with respect to the forward scattering direction. The diffraction pattern images are taken between approximately 5° and 26° with a resolution of 780 × 582 pixels. PPD-2K is the lab version of SID-3. A schematic drawing of PPD-2K is shown in Fig. 3.7. It has a measurement chamber, where the particle flux is focused into the laser beam. In PPD-2K 8 % of the forward scattered light is directed to the trigger optics with a beam-splitting mirror. The diffraction patterns are recorded for the remaining 92 % of the forward scattered intensity at an annulus between 7.4° and 25.6° with a resolution of 582 × 592 pixels. Both instruments use a photomultiplier tube to measure the trigger intensity.

During the deployment at the AIDA cloud simulation chamber PPD-2K and SID-3 are operated with a mass flow rate of 5.4 standard L min^{-1} and 50 standard L min^{-1}, respectively. A reduction of the effective sampling volume due to the electronic dead time of 8.00 µs (SID-3) and 8.25 µs (PPD-2K) is taken into account for the calculation of the particle concentration, following the procedure of [156]. Particle concentrations are calculated with an integration time of 10 s. Both instruments have a maximum particle detection rate of 11 kHz and a maximum image rate of 30 Hz. For particle rates higher than 30 Hz, diffraction patterns are recorded only for a subsample of the particles. The PPD-2K measurement uncertainty in particle concentration is dominated by the uncertainty in mass flow rate. In PPD-2K all particles pass the laser beam because a specific nozzle with a sheath flow focuses the particle flux to a smaller diameter than the laser beam width. For the Dome C deployment, the relative uncertainty in mass flow rate and therefore also in concentration is estimated to be 10 %. The particle concentration is the concentration of particles with sizes larger than the lower size detection limit of PPD-2K of 11 µm.

The size calibration of both instruments is performed by measuring droplets of different sizes according to the procedure of [156]. The diffraction patterns for spherical particles show distinct concentric rings. The particle size can be derived by fitting an intensity distribution calculated with Mie theory to these rings. The relation between the trigger intensity I in counts and the spherical equivalent diameter d of the particle is then given by

$$d = a \cdot I^b \tag{3.10}$$

with calibration coefficient a and b. Calibration coefficient a depends on the photomultiplier tube gain and the laser power and calibration coefficient b depends on the trigger geometry ($b = 0.528$ for SID-3 and $b = 0.522$ for PPD-2K) [156]. For all particles —independent of their shape— the resulting diameter is the spherical equivalent diameter d. The detectable range of d depends on the used trigger gain settings and campaign-specific size calibration. The detectable particle size range ranges between 5 µm to 35 µm for high gain settings and between 11 µm and 150 µm for low gain settings.

Exemplary, the calibration for the measurements at Dome C, Antarctica, is shown in Fig. 3.8e. The droplet size derived from Mie fits is shown as a function of the trigger intensity. A function fit of equation 3.10 to the measurement data returns $a = (2.02 \pm 0.03)$ µm. The fit uncertainty in a of 0.03 leads to relative measurement uncertainty in particle size of 1.5 %. The spherical equivalent diameter is the diameter of a sphere that scatters the same intensity in the direction of the trigger field of view as the detected particle. The ice particle maximum dimension is estimated to be up to 2.5 times larger than the spherical equivalent diameter due to the variety of ice particle shapes with different degrees of morphological complexity (see appendix A.2).

The diffraction patterns allow us to obtain information about the shape and small-scale complexity of the measured particles. The complexity is quantified using the normalised energy parameter k_e of the gray-level co-occurrence matrix (GLCM) method [95]. The GLCM method is a speckle texture analysis describing how often pairs of pixels with the same gray level occur along a given direction separated by a defined distance Δx. The method has previously been applied to characterise ice crystal complexity from the diffraction patterns [152, 150, 135]. The energy parameter k_e is the

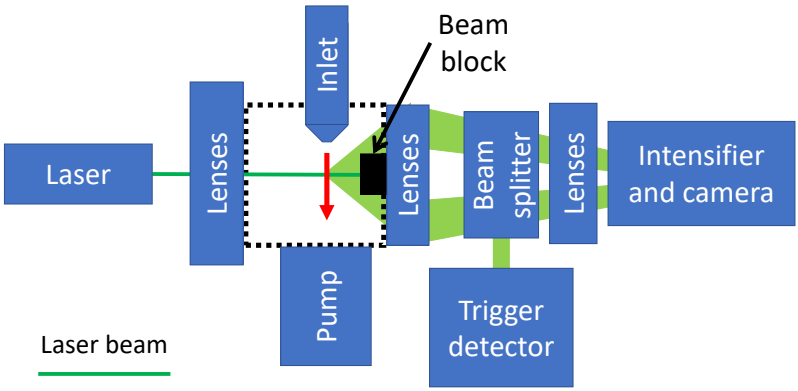

Figure 3.7.: Schematic drawing of PPD-2K.

coefficient of an exponential fit to the sum $E(\Delta x)$ of the squared elements of the GLCM

$$E(\Delta x) = \sum_{i=0}^{m-1} \sum_{j=0}^{m-1} p(\Delta x, i, j)^2 \tag{3.11}$$

with normalised co-occurrence matrix elements $p(\Delta x, i, j)$ for pixel distance Δx and co-occurrence matrix size m. k_e has been identified as the most robust parameter to characterize ice crystal small-scale complexity by [135], using diffraction pattern images with a mean intensity between 10 and 25 counts to reduce the bias from mean intensity fluctuations. The ice crystal complexity measured with k_e is in dimensions of the size of the wavelength of the used light ($\approx 0.5\,\mu m$) [69]. Thus, k_e is referred to as the small-scale complexity parameter in the following. A threshold for ice crystals with a rough surface is defined to $k_e = 4.6$ for SID-3 measurements by [135]. In this work, k_e is calculated for images of PPD-2K diffraction patterns. PPD-2K diffraction patterns with k_e between 3.8 and 5.0 are shown in appendix A.3. Images with $k_e = 4.6$ and higher show increasing speckles in the diffraction patterns, confirming the threshold of $k_e = 4.6$ for rough ice particles also for PPD-2K.

Information about the shape of the ice particles can be derived from the diffraction patterns using a Fourier analysis. A fast Fourier transformation

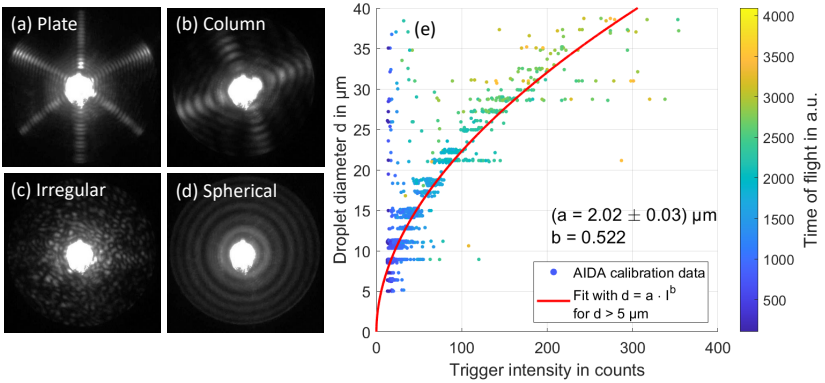

Figure 3.8.: Size calibration of PPD-2K for the field campaign at Dome C in **(a)**. The droplet size derived from Mie fits to the diffraction patterns is shown as a function of the trigger intensity in counts. The time of flight is the time that the measured intensity exceeds the set trigger threshold and therefore increases with the particle size for constant particle speed. The calibration droplet clouds with changing droplet sizes are created in the AIDA cloud simulation chamber during the Cloud In Situ 01 (CIS01) campaign in May 2023. **(b)**-**(d)** shows example diffraction patterns of a plate-like, an irregular, a columnar and a spherical particle recorded at Dome C, Antarctica.

of the polar integrated intensity profile was introduced by [156]. Maximum Fourier coefficients of 3 and 6 occur for plate-like hexagonal particles (see example diffraction pattern in Fig. 3.8a) and maximum Fourier coefficients of 2 and 4 occur for columnar particles (see example diffraction pattern in Fig. 3.8b). Other maximum Fourier coefficients are interpreted as irregular (see example diffraction pattern in Fig. 3.8c) unless the particle is identified as spherical having clear maxima in the azimuthally integrated intensity profile that correspond to the maxima calculated for a sphere with Mie theory (see example diffraction pattern in Fig. 3.8d). A different approach from [132] uses machine learning to identify particle habits from the diffraction patterns. A visual geometry group 16 (VGG16) convolutional neural network (CNN) [141] trained with hand-selected images sorts the diffraction patterns into groups of small rough, rough pristine, irregular, sublimating, and spherical particles. Additional categories are small (empty) and large (saturated) images. Small particles are removed from the analysis because they were predominantly empty images that were triggered on noise. More details about the VGG16 method, its accuracy, and the training process are found in [132].

At Dome C, the instrument sometimes recorded bursts of triggers on noise at count rates orders of magnitude higher than real particle counts. The bursts of triggers on noise only resulted in empty images, which confirms that they were not caused by real particles. These short periods that occurred mainly during the start-up phase of the instrument are removed from the data analysis with the following procedure. The particle counts are integrated over time periods of 10 s. Integration periods that contain two or more consecutive empty diffraction patterns are excluded. Empty images are identified by a mean image intensity that is smaller than seven counts, which is the upper limit of the empty image intensity range. Then, the average concentration over periods of 1200 s is calculated only using the valid 10 s measurement periods. The averaging period of 1200 s is chosen to obtain robust counting statistics also at low particle concentrations and is comparable to the particle concentration measurement integration time by [85] for measurements at South Pole station on the Antarctic plateau. The used averaging period is slightly higher than the integration time of ice fog measurements with PPD-2K at Fairbanks, Alaska, [133], where higher particle concentrations persisted. This procedure ensures that the triggers on noise do not affect the recorded particle concentration.

3.3. Light scattering and depolarisation instrument SIMONE

SIMONE (Streulichtintensitatsmessungen zum optischen Nachweis von Eispartikeln - Scattering Intensity Measurements for the Optical Detection of Ice Particles) measures the near forward (2°) and the near-backscattering (178°) intensity of light that is scattered by particles in the detection volume of approximately 7 cm^3 inside the AIDA cloud simulation chamber [136]. Fig. 3.9 shows the schematic setup. The linear depolarisation ratio δ is calculated as

$$\delta = \frac{I_{\perp} - I_{\perp,\mathrm{bg}}}{I_{\parallel} - I_{\parallel,\mathrm{bg}}} \tag{3.12}$$

where $I_{\parallel/\perp}$ is the detected intensity of scattered light with polarisation parallel/perpendicular to the scattering plane and $I_{\parallel/\perp,\mathrm{bg}}$ the background intensity with a polarisation parallel/perpendicular to the scattering plane [106]. The intensity is averaged over time intervals of 10 s.

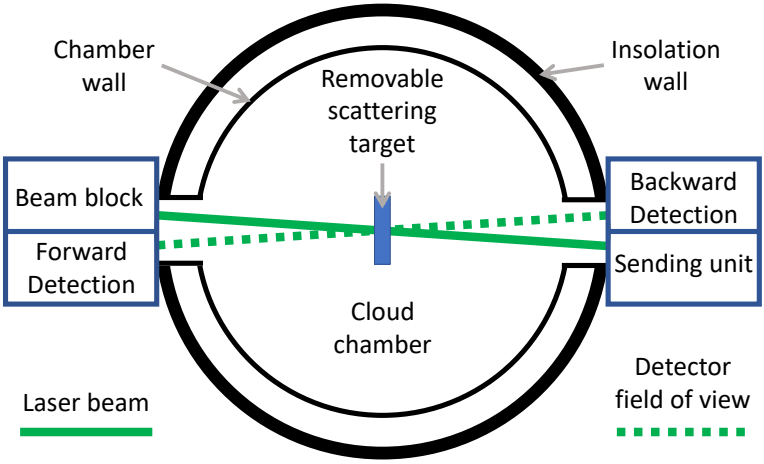

Figure 3.9.: Schematic drawing of the SIMONE instrument inside the AIDA cloud simulation chamber.

An optically-pumped semiconductor continuous wave laser (Coherent Sapphire) with a wavelength of 488 nm is used as a light source. The laser beam is linearly polarised and the polarisation direction can be adjusted with a liquid crystal rotator. For the depolarisation measurements, a polarisation axis parallel to the scattering plane is used. A polarising beam splitter allows the separate analysis of the near-backward direction intensity components with linear polarisation parallel and perpendicular to the scattering plane. The intensities are detected with Perkin Elmer MP-1383 photo multiplier tubes. The two channels are calibrated for each campaign using a scattering target (Spectralon diffuser from Labsphere) that is placed in the detection volume with a known linear depolarisation ratio of 0.92 at near-normal incidence and detection angle. For the RICE03 campaign, a slightly different setup was used, which is called SIMONE-Junior and operated at a wavelength of 552 nm with a detection volume of approximately 30 cm^2. Exemplary, the calibration of the RICE03 measurement campaign can be seen in Fig. 3.10. During the calibration procedure, the orientation of the linearly polarised incident light is switched between parallel and perpendicular orientation with reference to the scattering plane. A calibration factor can be multiplied to the parallel polarised channel to obtain the same linear depolarisation ratio independent of the orientation of the linearly polarised incident light. This calibration

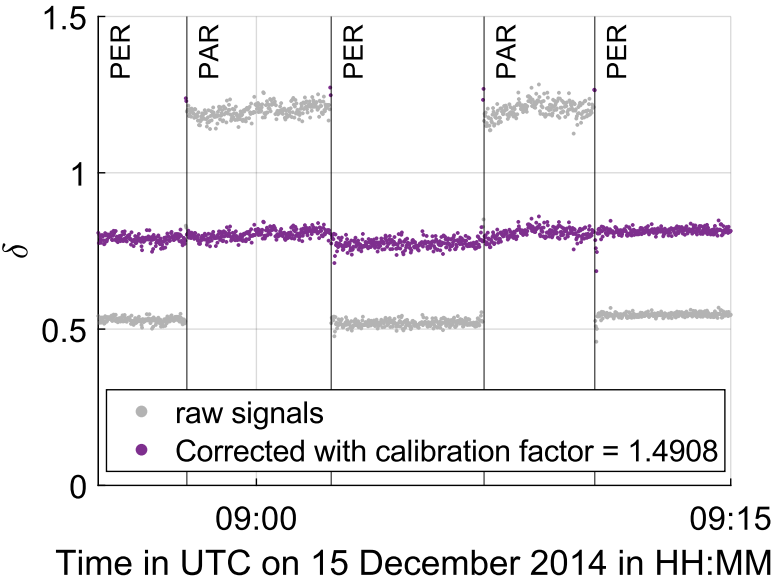

Figure 3.10.: Linear depolarisation ratio of the Spectralon diffusor, which is used as scattering target target to calibrate the gains of the two SIMONE backscattering photomultipliers during the RICE03 campaign. PAR indicates incident light with linear polarisation parallel to the scattering plane and PER indicates incident light with linear polarisation perpendicular to the scattering plane. For SIMONE-Junior during the RICE03 campaign, a calibration factor of 1.4908 is multiplied to the channel which detects light with parallel linear polarisation with reference to the scattering plane.

factor is 1.4908 for measurement campaign RICE03 (see Fig. 3.10). It takes into account the different gains of the detectors, different losses of the polarisation filtering, and effects of possible differences in alignment of the detectors. The uncertainty of the linear depolarisation ratio of SIMONE and SIMONE-Junior are 1.4 % [136] and 3 % [65], respectively.

3.4. AIDA cloud chamber

The Aerosol Interactions and Dynamics in the Atmosphere (AIDA) cloud simulation chamber at the Karlsruhe Institute of Technology (KIT) is an

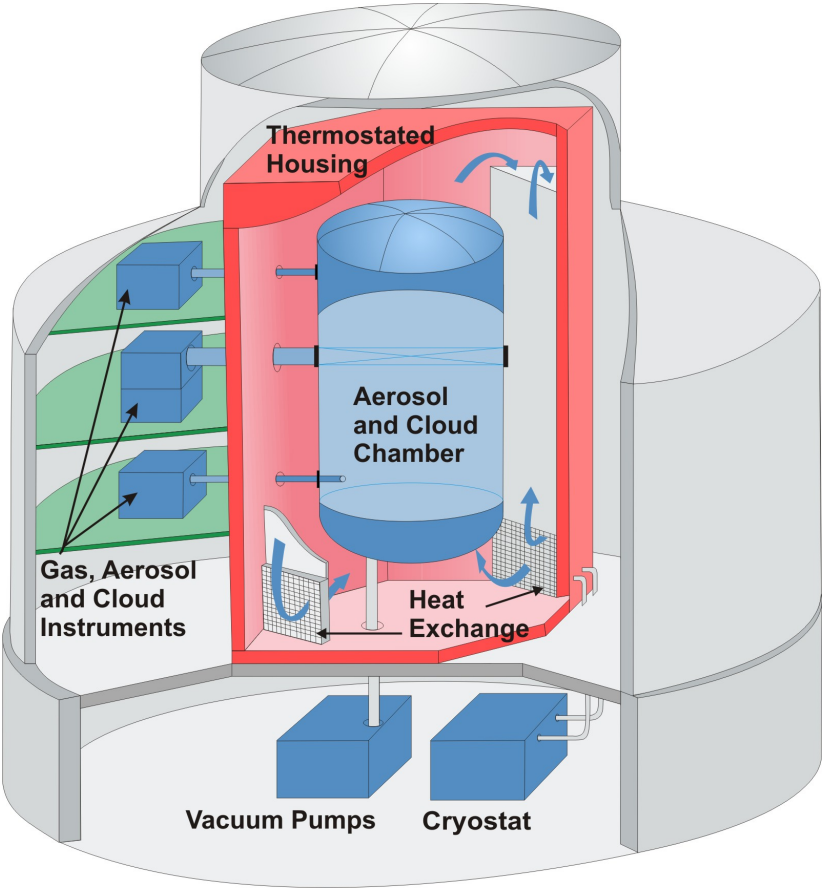

Figure 3.11.: Schematic drawing of the AIDA cloud simulation chamber at Karlsruhe Institute of Technology (KIT) [147] showing the cloud chamber, the thermostated, insulted housing, heat exchangers, and instrumentation.

expansion-type cloud chamber that simulates adiabatic cooling conditions of ascending air parcels in the atmosphere. A detailed description is given in e.g. [111]. It consists of a 84 m^3 cylindrical aluminium vessel inside an insulated, thermostated housing that can be cooled down to -90 °C using heat exchangers that evaporate liquid nitrogen. A schematic drawing can be seen in Fig. 3.11. A mixing fan is located at the bottom of the cloud chamber to

achieve homogeneous conditions through mixing. Multiple vacuum pumps with adjustable pump speeds can be used to evacuate the cloud chamber. Temperature and pressure are recorded at multiple positions inside the chamber and on its wall with the AIDA logging system. A tunable diode laser hygrometer setup [34] and a commercial chilled mirror dew point hygrometer (MBW calibration AG, model 373) are used for relative humidity measurements. Below the cloud chamber inside the insulated, thermostated housing, cloud instrumentation like PHIPS, SID-3, and PPD-2K can be mounted. Their inlets are connected via valves to the cloud chamber and their outlets are connected via valves and mass flow controllers to the vacuum pumps. This allows isolating the instruments when evacuating the cloud chamber during cleaning cycles and to set defined mass flow rates for the different instruments during operation.

Furthermore, a formvar replicator was operated during measurement campaigns RICE01 and RICE03, which generated replicas of the ice particles on 35 mm plastic film strips. Details about the setup are found in [135]. Images of the formvar replicas are taken with an Imaging Source DFK41AU02 camera with a resolution of 1280 x 960 pixels in combination with a Zeiss IM35 inverted microscope with a magnification of up to 500. These images are used to derive additional information about the particle morphology, such as hollowness and air inclusions, which cannot be derived from the PPD-2K or SID-3 diffraction patterns. However, the replicator has a lower temporal resolution and inferior counting statistics in comparison to PPD-2K or SID-3.

In chapters 5 and 6 analyse measurement data of regrowth experiments performed at the AIDA cloud simulation chamber, using a similar procedure as in [135]. Regrowth experiments use the following procedure:

1. Preparation: The cloud chamber is evacuated and flushed multiple times to wash out remnants of previous experiments. Then, water is added to obtain a thin ice coating as a humidity reservoir on the inner chamber wall.

2. Aerosol addition: An aerosol generator is used to inject types of aerosol particles into the cloud chamber. Soot or mineral dust are effective ice-nucleating particles for heterogeneous freezing, while sulphuric acid is used for the homogeneous freezing experiments.

3. Initial cloud activation: The valve to the vacuum pumps below the chamber (see Fig. 3.11) is opened and the expansion starts. This is defined as reference time zero. The pressure and gas temperature in the cloud chamber decrease, while the relative humidity increases (see Fig. 3.12a and 3.12b). The freezing starts when the homogeneous freezing conditions are met or the relative humidity exceeds the aerosol-specific threshold for heterogeneous ice nucleation (see minute two in Fig. 3.12b). The growing ice particle take up water and thus the relative humidity starts to decrease again. This can be seen in the peak in relative humidity at approximately minute two in Fig. 3.12b.

4. Sublimation: The ice particles in the cloud chamber have different growth histories due to slightly different nucleation times. Therefore, the expansion is stopped and dry synthetic air is fed into the chamber increasing the gas pressure and decreasing the relative humidity (see Fig. 3.12a and 3.12b between minute five and seven approximately). This leads to a sublimation of the ice crystals and removes the ice crystal morphological complexity from the initial growth period.

5. Regrowth: The injection of dry air is stopped after a few minutes when the ice particles have reduced their size. The valve to the pumps is opened again and a second, controlled growth period is started. This can be seen in Fig. 3.12a and 3.12b between minute seven and minute 18 approximately. This time the relative humidity is kept at a constant, defined level. An experiment can consist of multiple sublimation and regrowth cycles of the same ice cloud.

6. Final sublimation: When the final pressure is reached the expansion is stopped. The humidity in the cloud chamber decreases due to the heat transfer from the chamber wall (see Fig. 3.12a and 3.12b after approximately minute 18). When the relative humidity with respect to falls below 100 % (ice saturation), the ice cloud starts to sublimate again. The experiment ends, when the ice cloud has sublimated completely, and the cloud chamber can be refilled.

The expansion experiments at the AIDA cloud simulation chamber are limited to growth times of several minutes to several tens of minutes due to loss from sedimentation of the ice particles. Larger ice particles sediment out faster due to increasing particle fall speeds.

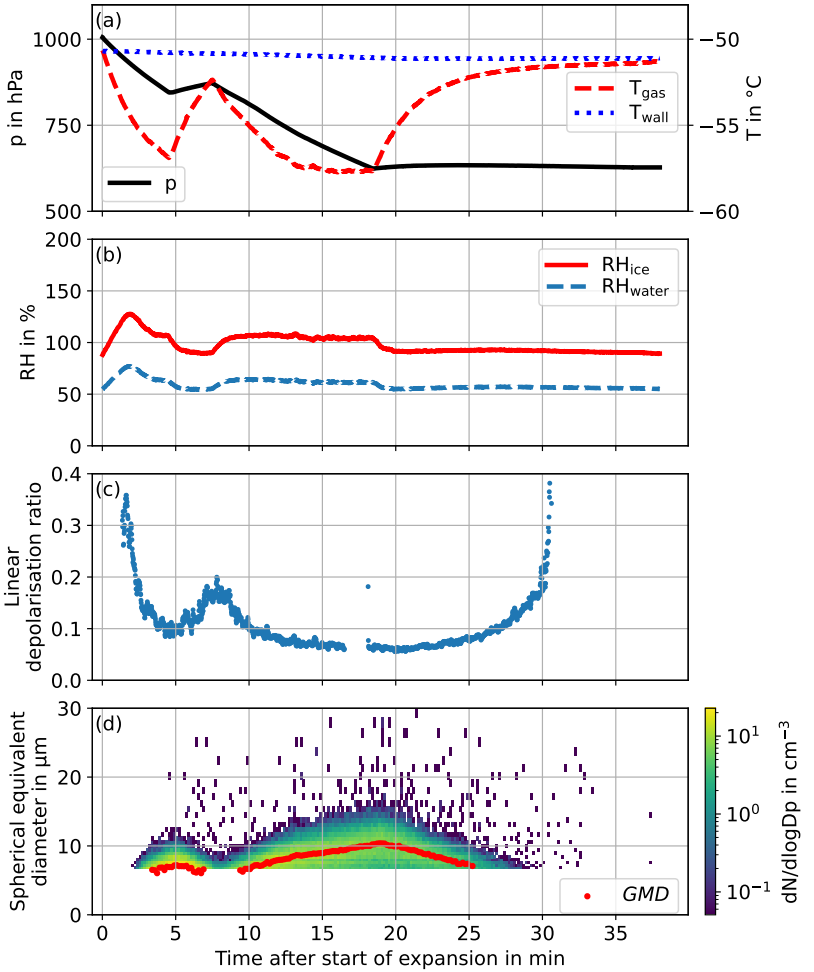

Figure 3.12.: Example expansion experiment 09 during the RICE02 campaign at the AIDA cloud simulation chamber. The different experiment phases of initial cloud activation, sublimation, regrowth, and final sublimation can be seen in the shown wall and gas temperatures (T_{wall} and T_{gas}), gas pressure (p), relative humidity (RH), linear depolarisation ratio (δ), and particle size distribution plots. GMD is the geometric mean diameter.

3.5. Measurement site at Concordia station, Antarctica

The Antarctic Italian-French Concordia station is located at 75°6′ S 123°21′ E, 1100 km inland from the nearest coast and 1670 km north of the geographic south pole on the ice dome Dome C. The station is situated at an altitude of 3233 m above sea level on top of an ice sheet of more than 3300 m thickness [63]. Concordia station is one of three Antarctic inland stations that are operated year-round. The summertime temperature at Concordia station ranges between -50 °C and -30 °C [63]. The wintertime temperature can drop down to -80 °C [63]. Access is only possible in the few summer months of the year, typically from early November to early February. The surrounding area is flat with no noticeable hills or valleys. The Antarctic plateau can be considered one of the cleanest environments on the planet according to a trace element analysis by [60]. The aerosol load at Dome C is low with observed median number concentrations of 260 m^{-3} in austral summer and 15 m^{-3} in austral winter for aerosol particle sizes between 20 nm and 600 nm [71]. The aerosol mass concentration at Dome C is approximately 0.1 $\mu m\, m^{-3}$ for particles with sizes smaller than 10 µm, which is a factor of approximately ten lower than at Antarctic coastal regions [4].

At Concordia station different atmospheric instruments are operated. This includes the Consiglio Nazionale delle Ricerche - Istituto Nazionale di Ottica (CNR-INO) depolarisation LIDAR that has been in operation since 2008 [24]. It probes the troposphere between heights of 10 m (AGL) and 12 km (AGL) with laser pulses from a linearly polarised laser at a wavelength of 532 nm and measures the backscattering signal intensity and the linear depolarisation ratio of clouds and aerosol [24]. The tropospheric profiles are produced with a temporal resolution of 5 min and a vertical resolution of 7.5 m. The linear depolarisation ratio δ yields information about the particle shape and phase because spherical particles (droplets) return δ close to 0, while non-spherical particles —for example ice particles— return non-zero δ [164]. The LIDAR signal is proportional to the particle scattering cross-section and the particle concentration.

An automated weather station (AWS) records ground temperature, relative humidity, wind speed and wind direction at Dome C [53]. Furthermore, temperature and relative humidity are recorded on a measurement tower near Concordia station at altitudes between 3 m (AGL) and 42 m (AGL) using

Vaisala HMP155 humidity probes with heated inlets [47]. The relative humidity with respect to liquid water and ice at ambient temperature are calculated from the measurements at the heated inlets. The parametrisation of [78] is applied. This setup avoids inaccurate measurements from ice deposition on the humidity sensor, which is a common issue in cold environments where high supersaturations (relative humidity >100 %) with respect to ice commonly occur. The measurement uncertainty for temperatures above -50 °C is 0.4 K in temperature, below 10 % for relative humidity measurements with respect to ice, and below 5 % for relative humidity measurements with respect to liquid water [154]. However, the systematic measurement uncertainty of the relative humidity measurements between November 2023 and January 2024, which are used in this work, is likely higher due to limited possibilities of instrument servicing at the extremely remote location.

The measurement site of the Dome C deployment of PPD-2K was the roof of the physics shelter (see Fig. 3.13), which is located approximately 500 m south of Concordia stations, upstream with regard to the local predominant wind direction. This is in a clean zone where no operation of motorized vehicles is allowed in order to minimise air pollution. During the measurement period between 21 November 2023 and 5 January 2024, PPD-2K was operated remotely with at least daily access during the first three weeks of the deployment and no access for the rest of the deployment. The sample inlet is a horn-shaped nozzle with a diameter of 39 mm designed to minimise sampling artefacts. The nozzle is upward facing and connected in a straight line to the measurement chamber of PPD-2K. A pump with a mass flow controller was used to set a mass flow rate of 5.4 standard L min^{-1}. The instrument operated in cycles of 170 min of measurement time separated by pauses of 10 min. The air temperature ranged between -45 °C and -22 °C at a mean air pressure of (646±6) hPa during the measurement period according to the automated weather station of Concordia station. The operational time of the instrument is shown in appendix A.2 where occasional downtimes can be seen mainly during the no access remote operation of the instrument. These occurred due to connection errors between the instrument and the computer. PPD-2K measurement data are removed from the analysis for wind speed and wind directions that could not rule out air pollution from Concordia station exhausts. The limits for the wind speed and wind direction can be seen in table 3.1 and are based on aerosol measurements by [155]. Drifting snow can occur at high wind speeds. At the measurement location and height of PPD-2K

Table 3.1.: Wind speed v and wind direction limits for data exclusion due to possible pollution from the exhausts of Concordia station. The wind speed limits and wind directions are based on aerosol measurements by [155], taking into account the different locations of the physics and atmospheric shelters at Dome C.

Wind speed v in $\mathrm{m\,s^{-1}}$	Lower excluded wind direction in °	Upper excluded wind direction in °
$v>2$	10	100
$1<v<2$	0 350	140 360
$v<1$	0	360

increasing particle concentrations due to drifting snow were recorded by a particle flatbed scanner when wind speeds exceeded $7\,\mathrm{m\,s^{-1}}$.

Figure 3.13.: Measurement site of PPD-2K on the roof of the physics shelter at Concordia station during the Dome C deployment between November 2023 and January 2024. This is in a clean zone where no operation of motorized vehicles is allowed to minimise pollution.

4. Boundary layer ice particles at Dome C, Antarctica

In this chapter, the microphysical properties of small boundary layer ice particles are presented, which were recorded at Concordia station (75°6′ S 123°21′ E) on the Antarctic plateau between November 2023 and January 2024. First, the fractions of different ice particle shapes are presented for different temperatures, relative humidity, and particle size ranges. Then, the temporal evolution of the microphysical properties of a three-day ice fog event is shown. The distinct LIDAR signature of the ice fog event motivates the analysis of the microphysical properties of all LIDAR-identified ice fog and cirrus precipitation/ diamond dust events during the measurement campaign. The results are compared to a study of ice fog in the urban, polluted environment of Fairbanks, Alaska, [133]. Furthermore, a homogeneous freezing event of supercooled fog is presented, which highlights homogeneous freezing as a possible origin of small boundary layer ice particles on the Antarctic plateau.

4.1. State of research of inland Antarctic boundary layer ice particles

The Antarctic plateau is a cold, dry, and clean region at an altitude of more than 3000 m above sea level (ASL), where essentially all precipitation is frozen [30]. Clear sky precipitation is abundant with a contribution of approximately 40 %. Ice crystals in this region commonly have sizes in the order of 10 µm and smaller [162]. However, atmospheric in situ measurements on the Antarctic plateau are scarce due to the remoteness and challenging weather conditions, which only allow access in the few summer months of the year. At the same time, Antarctica is one of the last places on the planet with very little

impact from human activity. On the Antarctic plateau, cirrus formation can be studied near the ground at low aerosol concentrations [71]. There have been several measurement campaigns, which studied ice crystals larger than 100 µm with optical array probes [85, 83], by imaging of precipitation on flat surface benches [162, 130] and using a flatbed scanner [21]. However, they cannot reliably determine particle shape, complexity, and size distribution for particle sizes below 50 µm [76, 152]. The microphysical properties of small ice particles in this size range have until now only been determined using scanning electron microscopy of formvar replicas. Furthermore, only some tens of formvar snapshots exist at the moment, covering a measurement time of approximately 30 s each [122]. Therefore, there is insufficient information about the microphysical properties of ice crystals with sizes smaller than 50 µm. The microphysical properties of small ice crystals are essential to accurately determine the cloud radiative impact of boundary layer ice crystals in polar regions [83, 91, 163].

Boundary layer ice particles are generally classified as diamond dust or ice fog [2, 170, 3, 171]. According to a commonly used parametrisation, ice fog has particle concentrations above $1 \cdot 10^3\,\mathrm{L}^{-1}$ and particle sizes smaller than 30 µm, while diamond dust has particle concentrations below $4 \cdot 10^3\,\mathrm{L}^{-1}$ and particle sizes larger than 30 µm [49]. However, the events cannot always be clearly separated, and reported ice fog particle sizes commonly fall outside of these ranges [55]. Wintertime simulations of downward infrared flux show an increase up to $60\,\mathrm{W\,m}^{-2}$ during falling diamond dust and of approximately $7.4\,\mathrm{W\,m}^{-2}$ during ice fog [50]. This leads to a simulated surface warming rate of $2.85\,\mathrm{K\,d}^{-1}$ and $2.57\ \mathrm{K\,d}^{-1}$ for a three-day event of diamond dust and ice fog, respectively. Due to its longer lifetime, in general, ice fog tends to have a higher impact. Homogeneous freezing of solution aerosol particles has been suggested as a nucleation mechanism for a locally formed ice fog event at Dome C [154]. But no direct proof was found, lacking in situ microphysical measurements at the site. The single particle counter and diffraction pattern imager PPD-2K has the capability to measure ice crystal size, complexity, and shape information for particle sizes down to a few microns [76], returning valuable microphysical information of ice fog (for more details on PPD-2K see section 3.2). This has been reported in previous studies of urban, polluted ice fog in Fairbanks, Alaska, [132, 133]. The in situ measurements with PPD-2K can add important information to the open question of the nucleation process of locally formed ice fog on the Antarctic plateau. In addition, in situ measurements are valuable for the validation of satellite remote sensing data

and atmospheric modelling of inland Antarctica, which presently relies on a small number of measurements [114].

During the measurement campaign at Dome C, PPD-2K was deployed between 21 November 2023 and 5 January 2024 near Concordia station at an altitude of 3233 m (ASL). The instrument recorded more than 700 000 particles with spherical equivalent diameters between 11 µm and 150 µm. PPD-2K had an uptime of 57.8 % during the 47-day measurement period. Approximately one quarter of the uptime wind speeds and directions prevailed, which did not rule out aerosol pollution from Concordia station (see table 3.1). Therefore, 25.1 % of the measurement data had to be excluded. The resulting overall data coverage between 21 November 2023 and 5 January 2024 is 43.3 %. Atmospheric measurement data that is year-round recorded at Concordia station is used for the analysis of the PPD-2K data. This includes temperature and humidity measurements at heights between 3 m and 42 m (AGL) at a measurement tower [46], wind speed and wind direction from an automated weather station (AWS) [53], and a LIDAR measuring the backscattering signal and linear depolarisation ratio of the troposphere [24]. In addition, the measurement data collected at Dome C is compared to previous measurements of urban ice fog at Fairbanks, Alaska, with PPD-2K between 2020 and 2022 [132, 133]. At Fairbanks, there are strong influences from anthropogenic water vapour and combustion particle emissions [134].

4.2. Effects of atmospheric conditions on particle habits

In this section, the particle shape fractions for different temperature, temperature inversion, relative humidity, and particle size are shown. The particle shape classification is done using the machine learning method [132] and the Fourier analysis method [156] (see section 3.2). Fig. 4.1 shows the habit classification using the machine learning method for different temperatures at 3 m above ground level (AGL), relative humidity with respect to ice (RH_{ice}), temperature inversion, and particle size ranges. The temperature inversion is defined as the difference in temperature at an altitude of 42 m (AGL) and an altitude of 3 m (AGL).

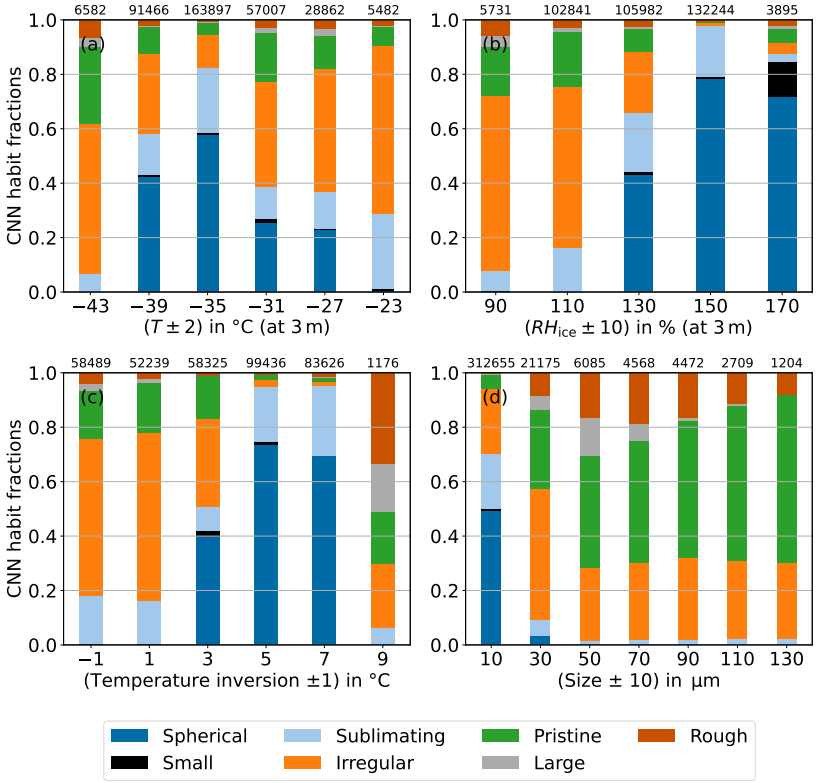

Figure 4.1.: Particle habit fractions for different temperature (T) **(a)**, relative humidity with respect to ice (RH_{ice}) **(b)**, temperature inversion **(c)**, and particle size **(d)** ranges according to the machine learning method [132]. T is measured 3 m (AGL) by an AWS [53] and RH_{ice} at the meteorological tower at Dome C 3 m (AGL). The temperature inversion strength is defined as the difference between the temperature measured at 3 m (AGL) and 42 m (AGL) at the meteorological tower at Concordia station. The data are shown for wind speeds and directions when no pollution from Concordia station was possible. The numbers above the bars give the number of investigated diffraction patterns per range.

The fraction of machine learning classified particle shapes for different temperature ranges at 3 m (AGL) is shown in Fig. 4.1a. The fraction of sublimating particles increases and the fraction of pristine particles decreases with increasing temperature. This finding is consistent with previous laboratory experiments that observed more pristine ice particles at colder growth con-

ditions [6, 135]. In the temperature range between -40 °C and -34 °C, the largest particle fraction is supercooled liquid droplets. This is due to two high concentration events of supercooled liquid droplets on 17 and 18 December 2023 that dominate the total number of recorded particles at this temperature range.

Fig. 4.1b shows the effect of RH_{ice} on the machine learning method habit fractions. The fraction of rough particles is below 5 % for all ranges of RH_{ice}. This shows that small boundary layer ice particles on the Antarctic plateau rarely have rough surfaces, which indicates that they grew at low levels of available water vapour because increased water vapour availability was found to increase ice particle roughness [135]. Unexpectedly, the fraction of sublimating particles increases with increasing relative humidity because this type of diffraction pattern is expected for ice particles at relative humidity below or close to saturation with respect to ice [135, 133]. A possible explanation can be that not only sublimating ice particles show this type of diffraction pattern. Frozen droplets in cloud chamber experiments have been observed to show similar diffraction patterns [68]. However, it needs to be taken into account that ice particles, which sedimented or were advected to the measurement site, could have had different particle growth conditions than the growth conditions observed at the measurement site. The largest fraction of spherical particles (droplets) was observed for RH_{ice} between 140 % and 160 % . This is consistent with the RH_{ice} at water saturation at temperatures between -40 °C and -30 °C, which is the predominant temperature range during the measurement period at Dome C [78, 138].

In Fig. 4.1c, the particle shape fractions are shown for different temperature inversion ranges. The trends look similar to the trend with RH_{ice} in Fig. 4.1b. This can be attributed to the increase in RH during temperature inversions. The increase of RH is caused by the cooling in the stable inversion layer with a simultaneous suppression of vertical mixing. This is supported by the data, which has a moderate correlation with a Pearson correlation coefficient of 0.66 between RH_{ice} and the temperature inversion (p-value < 0.01).

Fig. 4.1d shows the size-dependent particle fractions. Spherical (liquid) particles and sublimating particles only occur at fractions higher than 10 % for particle sizes below 20 µm. With 48 %, the largest fraction of irregular particles is found for particle sizes between 20 µm and 40 µm. The fraction of pristine particles increases with increasing particle size from a fraction of 5 %

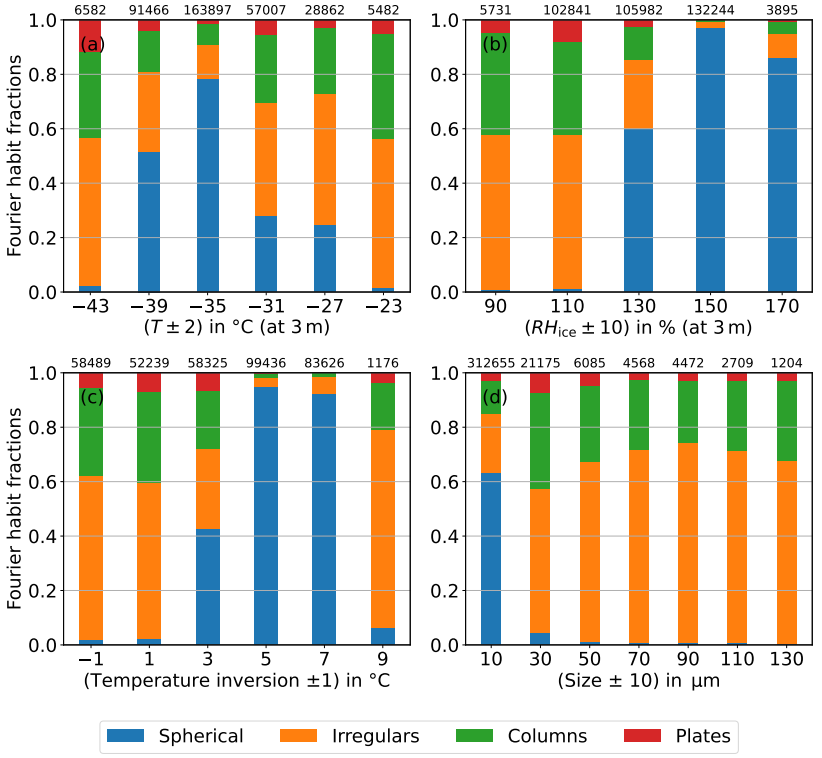

Figure 4.2.: Particle habit fractions for different temperature (T) **(a)** and relative humidity with respect to ice (RH_{ice}) **(b)**, temperature inversion **(c)**, and particle size **(d)** ranges according to the Fourier method [156]. T is measured 3 m (AGL) by an automated measurement station [53] and RH_{ice} at the meteorological tower of Dome C 3 m (AGL). The temperature inversion strength is defined as the difference between the temperature measured at heights of 3 m (AGL) and 42 m (AGL) at the meteorological tower at Concordia station. The data are shown for wind speeds and directions when no pollution from Concordia station was possible. The numbers above the bars give the number of investigated diffraction patterns per range.

at particle sizes below 20 µm to a fraction of 61 % at particle sizes between 120 µm and 140 µm.

In Fig. 4.2 the habit classification using the Fourier method is shown. There is good agreement between the two methods. For example, spherical particles have the largest fractions in the temperature bins of (−35 ± 2) °C and

(−39 ± 2) °C, for relative humidity with respect to ice exceeding 120 %, for temperature inversions between 2 °C and 8 °C, and for particle sizes smaller than 20 µm. But there are also differences seen between the two methods. For instance, the machine learning method generally shows a slightly lower fraction of spherical particles. This can be caused by a misclassification of slightly elliptical scattering patterns as spherical by the Fourier analysis method, whereas slightly elliptical scattering patterns tend to be correctly classified as sublimating by the machine learning method [132]. Furthermore, the machine learning method identifies a higher fraction of pristine particles for all particles with sizes larger than 40 µm in comparison to the combined fraction of columns and plates identified by the Fourier method. This is probably caused by particles, which do not show the distinct diffraction patterns of columns or plates, but still exhibit a distinct intensity maximum at the 22° halo angle. Therefore, these particles are classified as irregular according to the Fourier method and pristine according to the machine learning method, which is sensitive on the 22° halo peak. In the following section, the temporal evolution of the ice particle microphysical properties during a multi-day ice fog event is presented.

4.3. Temporal evolution of an ice fog event starting on 25 November 2023

In this section, the temporal evolution of the microphysical properties and atmospheric conditions of an ice fog event at Dome C is presented. The PPD-2K measurements of the ice particle microphysical properties between 25 November 2023 and 28 November 2023 are shown in Fig. 4.3 together with the atmospheric conditions.

Before the onset of the ice fog event, a period of high-level streaks of ice crystal precipitation from altitudes of more than 1000 m (AGL) occurred until approximately 15:00 UTC on 25 November 2023, followed by a short period of clear sky. This can be seen in the temporal LIDAR plots of the backscattering signal in Fig. 4.3a and the linear depolarisation ratio in Fig. 4.3b, which show the vertical profiles of the troposphere above Concordia station. A thin fog layer started forming at approximately 18:00 UTC on 25 November 2023 with a linear depolarisation ratio larger than 0.1, indicating the presence of ice [164]. The layer had a vertical extent of a few tens of meters. At the same

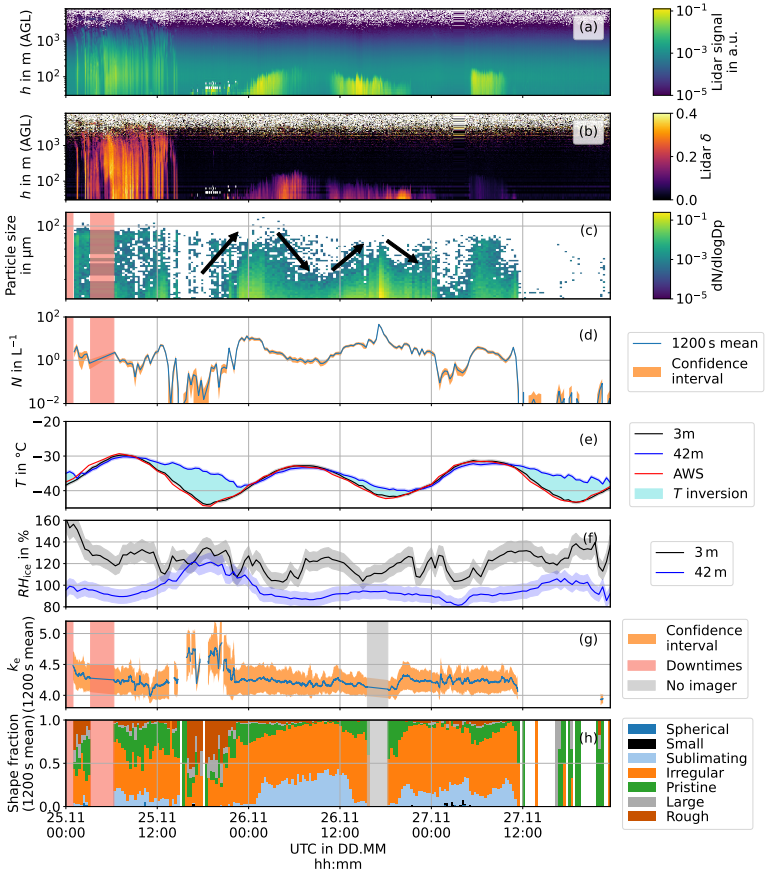

Figure 4.3.: Temporal evolution of an ice fog event at Dome C starting on 25 November 2023 with LIDAR backscattering signal **(a)**, LIDAR linear depolarisation ratio (δ) **(b)**, PPD-2K particle size distribution **(c)**, and PPD-2K particle concentration (N) integrated over 1200 s between 11 µm and 150 µm **(d)**. The particle growth and sublimation phases are highlighted with up- and downward pointing arrows, respectively. PPD-2K downtimes are highlighted in red. The temperature (T) and relative humidity (RH_{ice}) with respect to ice measured at the meteorological tower at Concordia station at altitudes of 3 m (AGL) and 42 m (AGL)d are shown in **(e)** and **(f)**. Temperature inversions are shaded in blue. The mean small-scale complexity parameter k_{e} derived from the Fourier PPD-2K diffraction pattern analysis [135] and the particle shape fractions from the machine learning method [132] are shown in **(g)** and **(h)** for time periods of 1200 s [156].

time, a pronounced temperature inversion of 10 K between the temperature at 3 m (AGL) ($T = -44\,^{\circ}\mathrm{C}$) and at 42 m (AGL) ($T = -34\,^{\circ}\mathrm{C}$) occurred. This can be seen in the temperature data from the tower measurements near Concordia station in Fig. 4.3e. The temperature inversion is highlighted with a light blue shade. At these low temperatures near the ground, no supercooled liquid droplets could exist [61]. This is confirmed in the particle habit fractions from the machine learning method and Fourier PPD-2K diffraction pattern analysis in Fig. 4.3h and Fig. 4.5c, which showed a very low fraction of spherical particles at this time. The particle concentration measured with PPD-2K is shown in Fig. 4.3d. It is the concentration of ice particles with sizes larger than the lower size detection limit of PPD-2K of 11 µm. The confidence interval includes the systematic measurement uncertainty from the uncertainty in pump flow and the statistical uncertainty of the mean. The particle concentration increased gradually from approximately $10^{-2}\,\mathrm{L}^{-1}$ at 18:00 UTC to approximately $10^{1}\,\mathrm{L}^{-1}$ at 22:00 UTC.

During the appearance of the ice fog layer, the small-scale complexity parameter k_e increased from approximately 4.2 to 4.9 before dropping back to approximately 4.3. This can be seen in the rolling mean with a centered window of 300 s of k_e in Fig. 4.3g. The confidence interval is one rolling standard deviation with a centered window of 300 s. To be statistically robust, both are only shown for particle concentration exceeding $10^{-1}\,\mathrm{L}^{-1}$. The statistical relevance of the increase in k_e has been confirmed with a two-sample Welch t-test ($p < 0.01$), performed for the k_e values measured between 15:00 UTC and 21:00 UTC on 25 November 2023 (315 particles with mean k_e of 4.69) in comparison to the k_e values recorded in six-hour time periods before 15:00 UTC (1562 particles with mean k_e of 4.18) and the six-hour period after 21:00 UTC (9784 particles with mean k_e of 4.26). The used null hypothesis is that the particles recorded in the six-hour periods before and after the increase have the same mean k_e as during the six-hour period of the increase. The Welch t-test is chosen because it is more reliable for two samples with different sizes and variances [182]. The fraction of rough particles using the machine learning method increased simultaneously to k_e (see Fig. 4.3h). The sudden increase in ice particle small-scale complexity can be interpreted as a sign of homogeneous nucleation [150]. This is further discussed in section 4.7.

The LIDAR backscattering signal after 00:00 UTC on 26 November 2023 was higher than during the fall streaks of high-level precipitation before 15:00 UTC on 25 November 2023 (see Fig. 4.3a). This is consistent with the higher particle

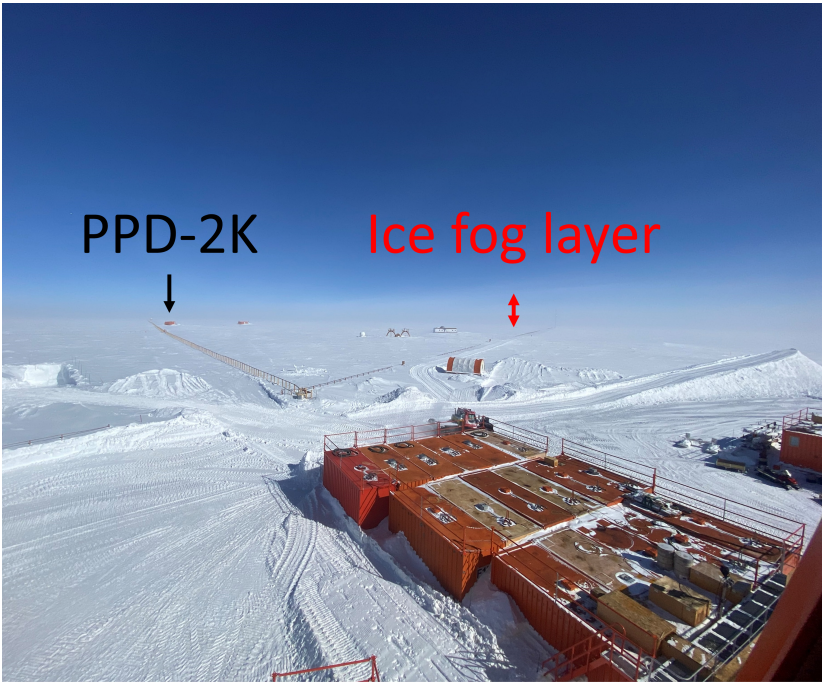

Figure 4.4.: Photo of the PPD-2K measurement site during the ice fog event starting on 25 November 2023 at a time when the ice fog layer was increasing in depth. The photo is taken at 00:19 UTC on 26 November 2023 from the main building of Concordia station. The ice fog layer is visible above the horizon and marked with a red arrow. The measurement site of PPD-2K is marked with a black arrow.

concentration measured with PPD-2K during the event of low-level boundary layer ice particles after 00:00 UTC on 26 November 2023 in comparison to the ice particle fall streaks before 15:00 UTC on 25 November 2023. A thin fog layer is visible above the horizon in a photo taken from the main building of Concordia station at 00:19 UTC on 26 November 2023 (see Fig. 4.4). The event of boundary layer ice particles can be classified as ice fog due to the decreased visibility [171, 3]. The classification of the event as ice fog is supported by the absence of higher possibly seeding clouds on the LIDAR backscattering signal.

The layer of ice crystals developed to a maximum vertical extent of approximately 200 m (AGL) at approximately 07:00 UTC on 26 November 2023. The time of the maximum vertical extent coincides with the diurnal temperature maximum and is likely caused by an increase in the boundary layer height. After 07:00 UTC on 26 November 2023, the vertical extent of the ice fog layer started to decrease again in height. Simultaneously, the LIDAR backscattering signal dropped until approximately 10:00 UTC on 26 November 2023. Then, the backscattering signal and the particle concentration started to increase again (see Fig. 4.3a,c,d). Simultaneously, due to the diurnal cycle, a temperature inversion built up again. This is seen in Fig. 4.3e. The vertical extent, LIDAR backscattering signal and particle concentration of the ice fog layer seem to be affected by the diurnal cycle between 00:00 UTC on 26 November 2023 and 00:00 UTC on 27 November 2023. The ice fog layer quickly weakened at approximately 00:00 UTC on 27 November 2023 so that it was not visible on the LIDAR backscattering signal until approximately 06:00 UTC (see Fig. 4.3a,b). This coincides with a simultaneous local minimum in particle concentration with approximately $10^{-1}\,\mathrm{L}^{-1}$ (see Fig. 4.3d) before the ice fog layer reappeared between 04:00 UTC and 11:00 UTC on 27 November 2023. At this final reappearance, the ice fog layer reached again a vertical extent of approximately 200 m (AGL) with a particle concentration of approximately $10^{1}\,\mathrm{L}^{-1}$. Advection can explain the relatively abrupt reappearance of the ice fog at approximately 06:00 UTC on 27 November 2023, when no inversion existed. At this time, δ was with a value of approximately 0.1 lower than earlier during the ice fog event when it reached values above 0.3. At approximately 11:00 UTC on 27 November 2023, the ice fog layer finally decayed with a drop in particle concentration from approximately $1\,\mathrm{L}^{-1}$ to approximately $10^{-2}\,\mathrm{L}^{-1}$. The LIDAR backscattering signal simultaneously dropped to the typical background level.

Ice fog was not initiated during the strong temperature inversion at approximately 18:00 UTC on 27 November 2023, which had similar conditions as the ice fog initiating temperature inversion at approximately 18:00 UTC on 25 November 2023. A possible reason can be the lower relative humidity at a height of 42 m or different aerosol conditions in the atmosphere.

The wind speed mainly ranged between $6\,\mathrm{m\,s}^{-1}$ to $8\,\mathrm{m\,s}^{-1}$ during the ice fog event in comparison to approximately $4\,\mathrm{m\,s}^{-1}$ to $6\,\mathrm{m\,s}^{-1}$ before and after (see Fig. 4.5a). The wind direction is shown in Fig. 4.5b. It changed from approximately 320° before to approximately 250° during and after the ice fog event. The approximately westerly winds transported clean air, which was

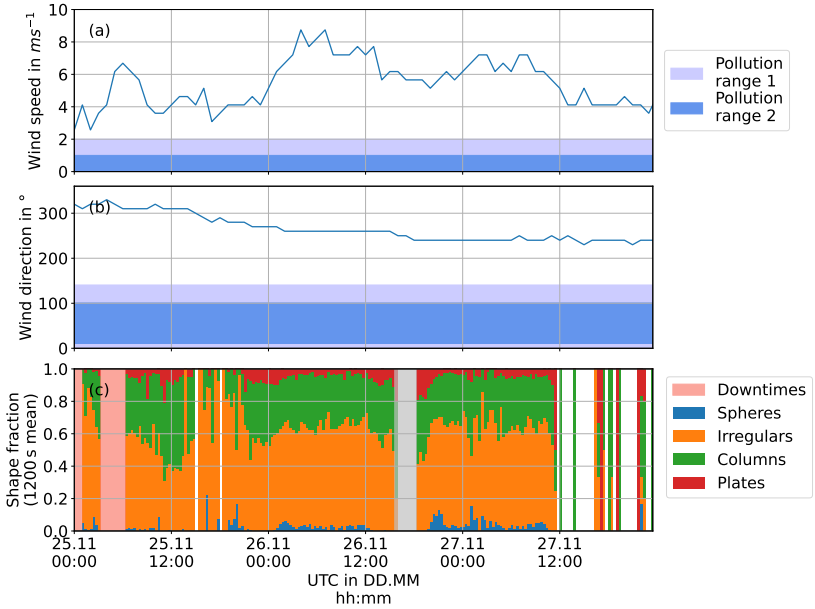

Figure 4.5.: Wind speed **(a)** and wind direction **(b)** from the AWS at Concordia station [53]. Pollution from the station's exhausts is possible when wind speed and direction are in range 1 (light blue shaded) or when wind speed or direction are in range 2 (dark blue shaded) [155]. Pollution from the station does not affect the measurements of the ice fog event starting on 25 November 2023. **(c)** shows the particle shape fractions from the Fourier PPD-2K diffraction pattern analysis [156].

not affected by air pollution from Concordia station, to the measurement site. Pollution from the station's exhausts is possible when wind speed and direction are in range 1 (light blue shaded) or when wind speed or direction are in range 2 (dark blue shaded in Fig. 4.5a,b) [155]. Drifting snow was unlikely to impact the measurements because at approximately 02:00 UTC on 27 November 2023 the particle concentration drops below $10^{-1}\,\mathrm{L}^{-1}$, while simultaneously the wind speed is at a relatively high level of approximately $7\,\mathrm{m\,s}^{-1}$. This shows that the increased background concentration due to drifting snow ($< 10^{-1}\,\mathrm{L}^{-1}$) at the given wind speed is much lower than the particle concentration during the ice fog event ($> 1\,\mathrm{L}^{-1}$).

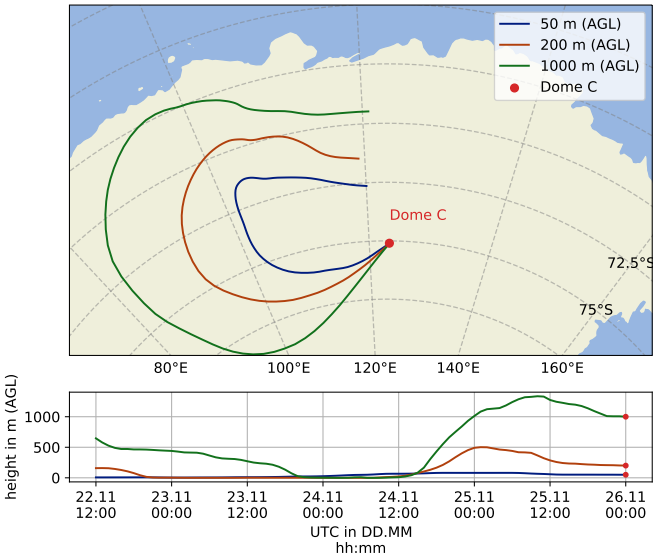

Figure 4.6.: 84 h back-trajectories at altitudes of 50 m (AGL), 200 m (AGL), and 1000 m (AGL), calculated with PySPLIT, a python-based tool for trajectory analysis with the Hybrid Single-Particle Lagrangian Integrated Trajectory model (HYSPLIT) [18, 144]. It shows that the air masses originated from inland Antarctica and the ice fog event was therefore locally formed.

To investigate the origin of the airmasses, a back-trajectory analysis was performed using PySPLIT, a python-based tool using the Hybrid Single-Particle Lagrangian Integrated Trajectory model (HYSPLIT) [18, 144]. The air-parcel back-trajectories were calculated based on Global Data Assimilation System (GDAS) data with a grid size of 1° x 1° (see `https://www.ready.noaa.gov/data/archives/gdas1/`, last accessed on 21 September 2025). 84 h back-trajectories at altitudes of 50 m (AGL), 200 m (AGL) and 1000 m (AGL) are shown in Fig. 4.6b for the ice fog event starting on 25 November 2023. They confirm that the ice fog event is locally formed on the Antarctic plateau because the air masses originated from inland Antarctica and not, for example, from maritime-influenced regions.

The 12 h mean particle size distributions measured with PPD-2K before, during, and after the ice fog event are shown in Fig. 4.7. The 12 h time periods start at the labelled time. The mean relative standard deviation over all particle event size and time bins is 1.5 using an integration time of 30 minutes.

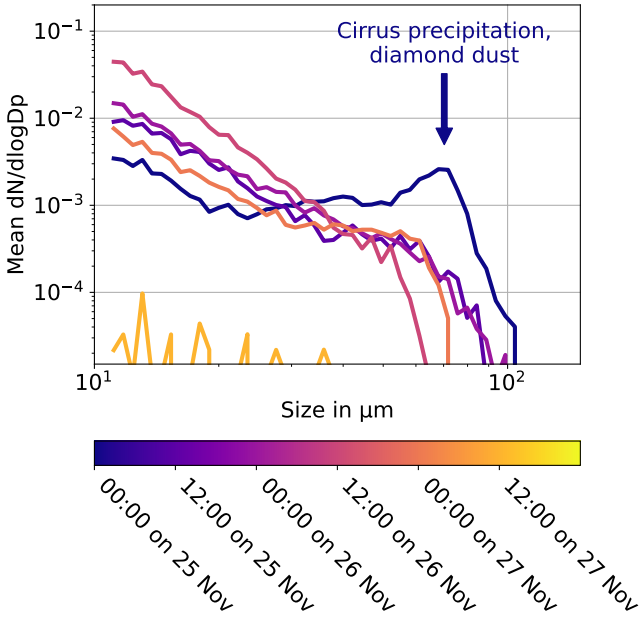

Figure 4.7.: 12 h mean particle size distributions (dN/dlogDp) recorded before, during and after the ice fog event starting on 25 November 2023. Only at 00:00 UTC on 25 November 2023 a particle size mode with a mean spherical equivalent diameter of approximately 70 µm is seen. This was a time of streaks of frozen clear sky precipitation and scattered cirrus precipitation. All 12 h mean particle size distributions from the ice fog event show a particle size distribution maximum at the lower size detection limit of PPD-2K at 11 µm. At 12:00 UTC on 27 November 2023 a two to three orders of magnitude lower particle concentration is recorded during clear sky conditions after the ice fog event.

The particle size distributions of streaks of ice crystals falling from altitudes of more than 1000 m (AGL) are shown in Fig. 4.7 at 00:00 UTC on 25 November 2023. These streaks of frozen precipitation are cirrus precipitation, or diamond dust when falling in clear sky conditions [170, 2]. During the event of high-level streaks, which occurred before the onset of the ice fog event, the particle size distribution is bi-modal with one peak at the lower detection size limit of PPD-2K at spherical equivalent diameters of 11 µm and a second peak at approximately 70 µm. The first mode with the peak at the lower detection limit of PPD-2K is also observed in the particle size distributions of the ice fog event in Fig. 4.7 between 12:00 UTC on 25 November 2023 and 00:00 UTC

on 27 November 2023. This size mode is hereafter called ice fog mode. The second mode at spherical equivalent diameters of approximately 70 µm is only observed in Fig. 4.7 at 00:00 UTC on 25 November 2023 when streaks of ice particles from high altitudes occurred. Hereafter, the second mode is called cirrus precipitation and diamond dust (cpdd) mode. The low particle concentration at 12:00 UTC on 27 November 2023 is a typical background level for clear sky conditions without diamond dust.

The distinct difference between the ice fog mode and the cpdd mode motivates the separate analysis of the microphysical properties of all ice fog and cpdd events that can be identified on the LIDAR signals at Dome C during the measurement period.

4.4. Microphysical properties of different precipitation events

In this section, the particle size, concentration, shape, and small-scale complexity (k_e) of the boundary layer ice particles at Dome C are analysed. Fig. 4.8 shows the measurement data of PPD-2K separately for LIDAR-based manually classified ice fog and cpdd events. Time periods looking similar to Fig. 4.3a,b between 00:00 UTC on 26 November 2023 and 00:00 UTC on 27 November with relatively stable low-level ice clouds are classified as ice fog (labelled: if). Time periods looking similar to Fig. 4.3a,b between 00:00 UTC and 14:00 UTC on 25 November 2023 with streaks of ice crystals falling from high altitudes with no dense or liquid clouds present are classified as cpdd events. When ice fog and cpdd events occurred at the same time, the data are not classified (2.0 % of the non-polluted operation period). 11.9 % of the non-polluted operational period are classified as cpdd events and 11.1 % are classified as ice fog events. The remaining fraction was mainly clear sky with occasional liquid cloud cover. The full data set from Dome C between 21 November 2023 and 09 January 2024 (excluding times when pollution from the station due to wind conditions was possible, labelled: all) and a PPD-2K data set of a three-year ice fog measurement campaign in an urban, polluted environment at Fairbanks, Alaska, (labelled: FB) are added for comparison [133].

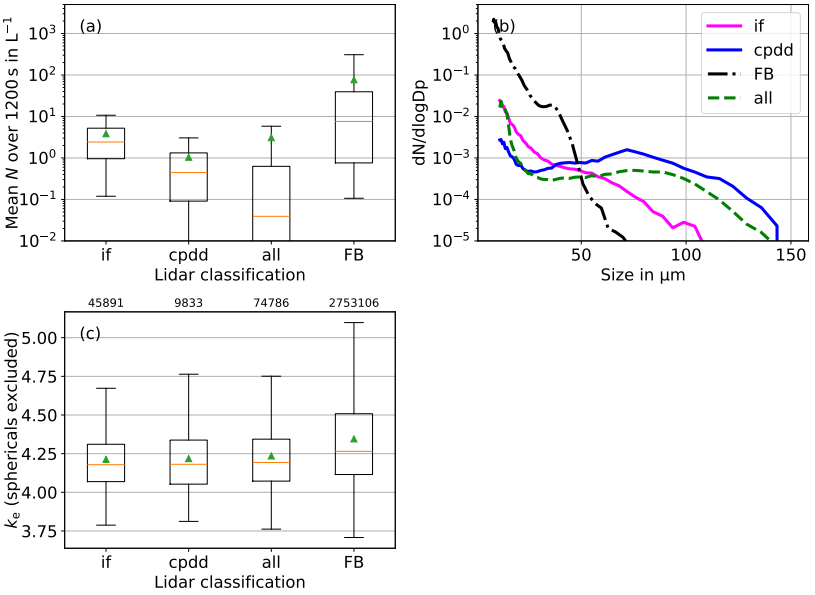

Figure 4.8.: Microphysical properties of boundary layer ice particles measured with PPD-2K for periods with low-level ice clouds (ice fog, labelled: if), for periods with high-level streaks of cirrus precipitation, and for diamond dust (labelled: cpdd) and for the complete non-polluted measurement period between 21 November 2023 and 09 January 2024 (labelled: all). PPD-2K data from a three-year ice fog study in an urban, polluted environment at Fairbanks, Alaska, between 2020 and 2022 is added for comparison (labelled: FB) [133]. **(a)** shows the mean particle concentration (N) over 1200 s, **(b)** shows the particle size distribution (dN/dlogDp), and **(c)** shows the small-scale complexity parameter k_e derived from the speckle pattern analysis of the diffraction patterns (sphericals are excluded) [135]. cpdd events at Dome C have an additional size mode that is not present for the ice fog events. The urban, polluted ice fog at Fairbanks has a higher concentration and more complex particles than the ice fog at Dome C.

Fig. 4.8a shows a boxplot of the particle mean concentration of the different events of boundary layer ice particles, integrated over 1200 s. The particle concentration includes ice particles with sizes between 11 µm and 150 µm, which is the size detection range of PPD-2K. The mean particle concentration of all ice fog events (labelled: if) is with 3.8 L^{-1} approximately four times higher than the mean particle concentration of all cpdd events with 1.0 L^{-1}. The mean particle concentration of all measurement times (labelled: all) is 3.1 L^{-1}. The findings align well with previous observations of generally

	Maximum particle concentration in L^{-1}			
Averaging period	Ice fog	cpdd	All	Fairbanks ice fog
60 s	$6.0 \cdot 10^1$	$4.2 \cdot 10^1$	$1.1 \cdot 10^3$	$2.5 \cdot 10^4$
1200 s	$4.8 \cdot 10^1$	$2.2 \cdot 10^1$	$5.6 \cdot 10^2$	$9.8 \cdot 10^3$

Table 4.1.: Maximum particle concentration measured with PPD-2K during LIDAR classified ice fog events, cirrus precipitation and diamond dust (cpdd) events, and the complete data set (all) recorded at Dome C. Averaging periods are 60 s and 1200 s. Maximum concentrations for urban, polluted ice fog measured with PPD-2K at Fairbanks during a three-year study between 2020 and 2022 are added for comparison. The measurement data from the urban site at Fairbanks can be attributed to high anthropogenic aerosol pollution and water vapour emissions.

higher ice fog particle concentrations in comparison to diamond dust particle concentrations [49].

The ice fog in Fairbanks has the highest mean particle concentration with $7.7 \cdot 10^1\,L^{-1}$. This is attributed to anthropogenic water vapour and combustion aerosol emissions in the urban environment of Fairbanks [134], which increase the ice particle concentrations. The maximum observed particle concentrations, measured over 60 s and 1200 s integration times, are presented in table 4.1. The complete Dome C data set has a maximum particle concentration of $1.1 \cdot 10^3\,L^{-1}$ over 60 s, the LIDAR classified ice fog events of $6.0 \cdot 10^1\,L^{-1}$ over 60 s, and the LIDAR classified cpdd events of $4.2 \cdot 10^1\,L^{-1}$ over 60 s. The higher peak concentration during the complete dataset is due to high-concentration, low-level supercooled liquid fog events on 17 and 18 December 2023 (see section 4.5). The peak particle concentration of the urban ice fog event in Fairbanks is multiple orders of magnitude higher than the Antarctic ice fog measurements. This again reflects the influence of anthropogenic water vapour and combustion aerosol emissions at Fairbanks, which can fluctuate due to advection and anthropogenic emission activity. Furthermore, the smallest difference between the maximum particle concentration averaged over 60 s and over 1200 s is observed for the ice fog events at Dome C. The higher fluctuation in particle concentration in time scales of minutes is inherent to fall streaks, which dominate the cpdd events. The urban, anthropogenically influenced ice fog can be affected by fluctuations of local aerosol or water vapour emissions.

Particle size distributions of the different particle events are shown in Fig. 4.8b. The particle size distributions of all events show the ice fog mode with a modal maximum at the lower detection limit of PPD-2K at spherical equivalent diameters of 11 µm. The cpdd mode at spherical equivalent diameters of approximately 70 µm can be seen in the particle size distributions of the cpdd events and less pronounced also in the particle size distributions of the complete non-polluted dataset of Dome C. Only when particles fall in streaks from higher altitudes is the cpdd mode observed. Cirrus precipitation and diamond dust particles dominate for sizes larger than approximately 50 µm and ice fog particles dominate for sizes smaller than approximately 40 µm during the austral summer at Dome C.

Furthermore, it can be noted that the particle size distribution of the ice fog at Fairbanks drops sharply for sizes larger than 50 µm, unlike the ice fog particle size distribution from Dome C, which gradually decreases for sizes between 50 µm and 100 µm. The sharp drop in the Fairbanks ice fog particle size distribution can be caused by the higher aerosol concentration that leads to higher particle concentrations and thus prevents the particle growth to larger sizes due to water vapour competition.

Fig. 4.8c shows the small-scale complexity parameter k_e, derived from the speckle pattern analysis of the PPD-2K diffraction patterns [135]. Spherical particles are excluded from the analysis because k_e is only defined for solid particles. The mean k_e of the cpdd periods, ice fog periods, and the complete Dome C measurement period are 4.21, 4.24, and 4.26, respectively. All three periods consist of relatively pristine ice particles according to the threshold for complex particles of 4.6 defined by [135]. A low degree of morphological complexity is expected for ice particles in the cold and dry environment at Dome C, which favours slow and pristine growth conditions. The ice fog particles from Fairbanks have a higher complexity with a mean small-scale complexity parameter of 4.35. This can be attributed to the large amounts of water vapour that are emitted in the atmosphere in Fairbanks. Higher water vapour increases particle growth speed, which favours a more complex crystal growth [6, 135].

Fig. 4.9a shows the particle shape fractions derived from the Fourier analysis method of the PPD-2K diffraction patterns [156]. For the ice fog and cpdd events, the fractions were relatively similar with 58 % and 54 % irregulars, 32 % and 40 % columnar particles, 8 % and 5 % plates, and 2 % and 1 % spherical particles, respectively. This finding is unexpected because ice particles

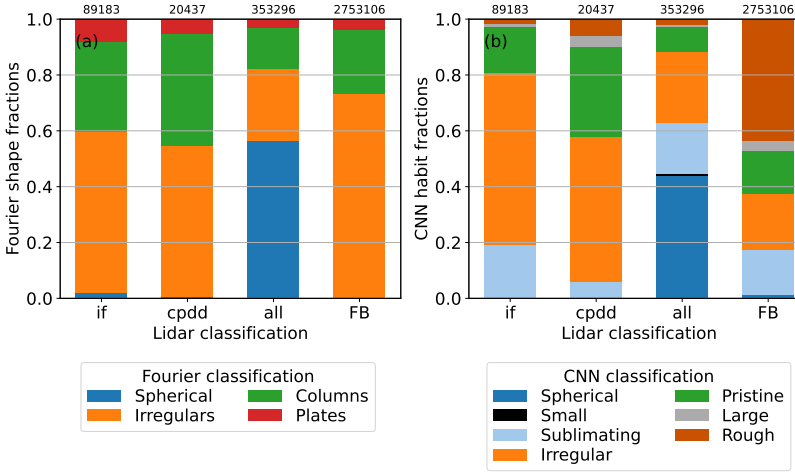

Figure 4.9.: Particle shape fractions of boundary layer ice particles measured with PPD-2K for periods with low-level ice clouds (ice fog, labelled: i), for periods with high-level streaks of ice crystals falling during clear sky conditions (labelled: cpdd), and for the complete non-polluted measurement period between 21 November 2023 and 09 January 2024 (labelled: all). PPD-2K data from a three-year ice fog study in an urban, polluted environment at Fairbanks between 2020 and 2022 is added for comparison (labelled: FB) [133]. **(a)** shows the particle fractions determined from the diffraction patterns with the Fourier analysis method [156] and **(b)** shows the particle habits derived from the diffraction patterns with the machine learning method [132]. The numbers above the bars give the number of investigated diffraction patterns per range. The urban, polluted ice fog at Fairbanks has a higher fraction of rough particles than the Antarctic boundary layer ice particles.

falling in streaks from higher altitudes and low-level ice fog particles have different growth regions. In the complete dataset from Dome C spherical particles make up the highest particle fraction with 54 %. The high fraction of spherical particles is predominantly due to two supercooled liquid fog events of 17 December 2023 and 18 December 2023 (see section 4.5). Furthermore, the complete dataset had 28 % irregular, 15 % columnar, and 3 % plate-like diffraction patterns. During the ice fog events at Fairbanks, ice particles with irregular diffraction patterns dominate with a fraction of 73 %. It furthermore has 23 % columnar, 4 % plate-like, and 0 % spherical diffraction patterns. The high fraction of irregular diffraction patterns is consistent with the higher k_e and likely caused by fast particle growth conditions due to high water vapour availability from anthropogenic emissions at Fairbanks. The low number of

spherical particles at Fairbanks, in comparison to Dome C, is likely caused by the high concentration of aerosol particles that lead to a higher ice nucleation particle (INP) concentration, which prevents the persistence of supercooled liquid droplets due to heterogeneous freezing.

The particle shape fractions from the machine learning method by [132] are shown in Fig. 4.9b. Using the machine learning method, additional information about the particle shape is gained from additional habit classes in comparison to the previously shown Fourier method. The cpdd events at Dome C have a lower sublimating particle fraction of 10 % in comparison to the ice fog observed at Dome C and at Fairbanks, with fractions of sublimating particles of 19 % and 16 %, respectively. The class of pristine particles varies between the particle events. The ice fog events at Dome C have a fraction of 17 % pristine particles, while Dome C cpdd events have a fraction of 31 % pristine particles. Therefore, the machine learning diffraction pattern classification reveals a difference between the ice particles from ice fog and cpdd events at Dome C, which was not possible with the Fourier diffraction pattern analysis. The differences are likely caused by the different growth conditions of the ice particles falling in streaks from high altitudes in comparison to the low-level grown ice fog ice particles. When growing in fall streaks, the ice particles likely grow slower due to lower water vapour availability, resulting in a higher fraction of ice particles showing the halo intensity maxima at the 22° polar scattering angle. The urban ice fog at Fairbanks has a higher fraction of rough particles (43 %) in comparison to the ice fog at Dome C (2 %). This supports the hypothesis that the ice fog ice particles at Fairbanks grow to more complex shapes due to more available water vapour from anthropogenic water vapour emissions. The higher fraction of rough ice particles in Fairbanks ice fog is consistent with the higher small-scale complexity k_e.

In the following, the measurements at Dome C are linked to the previous chapter 5 calculating the mean δ from the LIDAR measurements of the different events of boundary layer ice particles. The signal weighted mean δ is shown in table 4.2. All data are used where $0 \leq \delta \leq 1$ and the LIDAR signal is higher than the background of 10^2 a.u. The observed mean δ of 0.16 ± 0.14 is in good agreement with previous LIDAR observations of polar cirrus, which were in the range between 0.1 and 0.3 [22, 23, 125]. Furthermore, it can be noted that the mean δ of cpdd periods is with 0.28 ± 0.01 larger than the ice fog mean δ of 0.11 ± 0.08. A possible explanation can be the larger ice particle sizes of cpdd events with a modal mean *GMD* of about 70 µm in comparison to the ice fog events with a modal mean *GMD* smaller than 11 µm. An increasing δ

	Ice fog	cpdd	all
δ	0.11 ± 0.08	0.28 ± 0.01	0.16 ± 0.14

Table 4.2.: Mean linear depolarisation ratio of different boundary layer ice particle events at Dome C. All data are used where the LIDAR signal is higher than the background of 10^2 a.u. and $0 \leq \delta \leq 1$. δ of cpdd events is much higher than δ of ice fog.

with particle size was also found in the AIDA cloud simulation chamber at temperatures higher than -45 °C (see chapter 5.

4.5. Homogeneous freezing of local liquid fog event of 17 December 2023

The section analyses the freezing of locally formed low vertical extent supercooled liquid fog on 17 November 2023 at Dome C. Fig. 4.10 shows the temporal evolution of the boundary layer particle microphysical properties of 17 December 2023, together with the atmospheric conditions. The event started shortly after local solar midnight (15:42 UTC on 17 December 2023 at Concordia station) and lasted for approximately two hours. The liquid fog developed during clear sky conditions, which is seen in the low LIDAR backscattering signal in Fig. 4.10a. Wind speed and wind direction were in a range where no pollution from Concordia station altered the measurements and clear air from the Antarctic plateau was transported to the measurement site (see Fig. 4.11a and 4.11b). Pollution from the station's exhausts is possible when wind speed and direction are in range 1 (light blue shaded) or when wind speed or direction are in range 2 (dark blue shaded) [155]. The temperature at 3 m (AGL) decreased from -37 °C to -39 °C during the event (see Fig. 4.10e). Temperature data from the measurement tower as well as the AWS at Dome C are shown for redundancy. The two temperature measurements taken at a distance of a few hundred meters are in good agreement. Due to servicing, PPD-2K was not operating during the onset of the event. From webcam photos taken at the measurement site, it can be seen that the event started less than 20 minutes before the start of the data acquisition of PPD-2K, because no fog was seen on the webcam photo taken at 16:00 UTC (see Fig. 4.12). Between 16:20 UTC and 16:30 UTC, the concentration of particles with sizes larger than 11 µm increased to over 10^2 L^{-1} and stayed in this range until approximately 18:15 UTC (see Fig. 4.10d). Then the particle concentration

dropped again below 1 L^{-1}. The vertical extent liquid fog layer was shallower than the lowest LIDAR height bin of 30 m (AGL) (see Fig. 4.10a and Fig. 4.10b). This agrees well with the shallow fog layer seen on the webcam photos in Fig. 4.12. The machine learning method showed that the majority of the particles had spherical diffraction patterns and were thus liquid (see Fig. 4.10h). The machine learning method is used for this event because it is more sensitive on the detection of slightly non-spherical particles in comparison to the Fourier analysis method. When a diffraction pattern is not exactly spherical, the particle is classified as a sublimating ice particle [132]. This separation is important for an accurate distinction between frozen and liquid particles.

The supercooled liquid droplets grew to a maximum modal size of approximately 13 µm, which is shown in the temporal evolution of the particle size distributions in Fig. 4.10c. The relative humidity with respect to liquid water was close to saturation near ground (see Fig. 4.10f). Parts of the supercooled droplets existed for more than one hour while the air temperature drops from -37 °C at approximately 16:00 UTC to -39 °C at approximately 18 UTC. This is a surprising finding because at this temperature range the sudden homogeneous freezing of supercooled droplets is expected [61]. The fraction of frozen particles during the supercooled liquid fog event ranged between 10 % and 50 % but did not increase continuously. This is likely due to inhomogeneities of the fog that is advected to the measurement site at the wind speeds of approximately 2 m s^{-1} near ground level (see Fig. 4.11b).

The fraction of frozen particles rapidly increased from approximately 20 % at 17:15 UTC to approximately 50 % at 17:30 UTC at a temperature of approximately -38 °C. With a relatively constant particle concentration, this likely is an in situ observation of homogeneously freezing supercooled liquid droplets. The freezing of only approximately 50 % of the particle population highlights the selective nature of the homogeneous freezing process, which depends on the water composition and droplet size [78]. Between 17:30 UTC and 18:15 UTC, the fraction of liquid particles increased again. This can be explained by advection to the measurement site with a wind speed of approximately 2 m s^{-1} near ground level. The advection transported fog with different formation regions and conditions and thus possibly also different droplet compositions to the measurement site, affecting the droplet freezing temperature.

The particle concentration and the fraction of liquid particles dropped quickly after approximately 18:00 UTC. Liquid particles almost disappeared com-

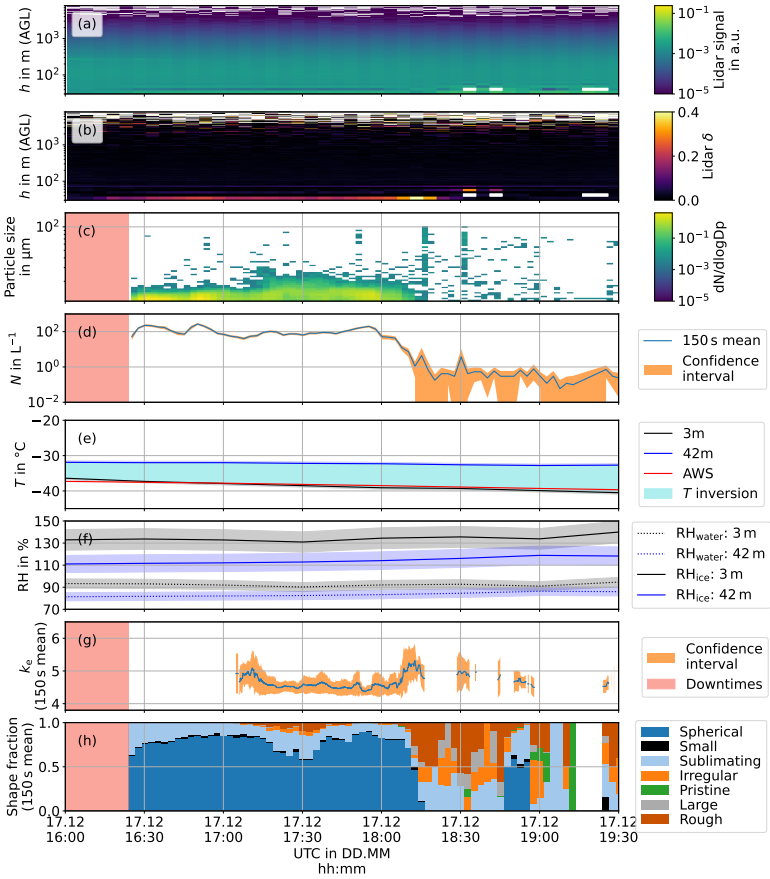

Figure 4.10.: Dome C supercooled liquid fog event of 17 December 2023 with temporal evolution of the LIDAR backscattering signal **(a)**, LIDAR linear depolarisation ratio (δ) **(b)**, PPD-2K particle size distribution **(c)**, and PPD-2K particle concentration (N) integrated over 150 s between 11 µm and 150 µm **(d)**. PPD-2K downtimes are highlighted in red. The temperature (T) and relative humidity (RH) with respect to liquid water and ice from the meteorological tower at Concordia station at altitudes of 3 m (AGL) and 42 m (AGL) are shown in **(e)** and **(f)**. The temperature data from the AWS at Concordia station at 3 m (AGL) is added for redundancy. Temperature inversions are shaded in blue. CNN classified particle shape fractions [132] and median small-scale complexity parameter (k_e) [156] derived from the PPD-2K diffraction patterns are shown in **(g)** and **(h)** for time periods of 150 s.

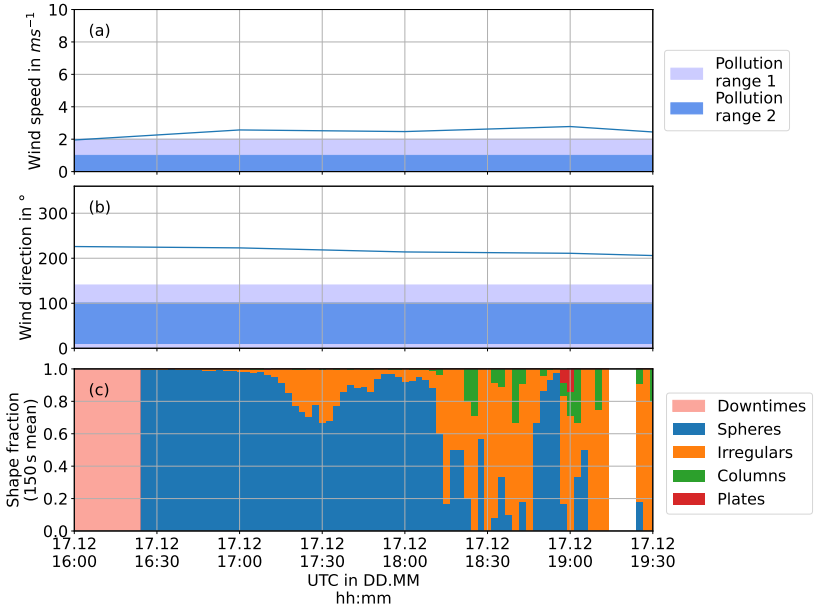

Figure 4.11.: Wind speed **(a)** and wind direction **(b)** from the AWS at Concordia station [53]. Pollution from the station's exhausts is possible when wind speed and direction are in range 1 (light blue shaded) or when wind speed or direction are in range 2 (dark blue shaded) [155]. Pollution from the station does not affect the measurements of the ice fog event starting on 25 November 2023. **(c)** shows the particle shape fractions from the Fourier PPD-2K diffraction pattern analysis [156].

pletely at approximately 18:15 UTC according to the machine learning method (see Fig. 4.10h), while the temperature kept dropping to -40 °C at approximately 19:00 UTC.

After the freezing, the largest fraction of the remaining ice particles was classified as rough particles. The small-scale complexity parameter was mainly above 4.6, the threshold of complex ice particles defined by [135]. This is in agreement with a previous finding that homogeneously frozen ice particles have an increased small-scale complexity parameter [150]. In addition, k_e is in a similar range as during the initiation of the ice fog event starting on 25 November 2023 at Dome C. Between approximately 18:40 UTC and 18:55 UTC, there is a final short period of spherical particles at approximately

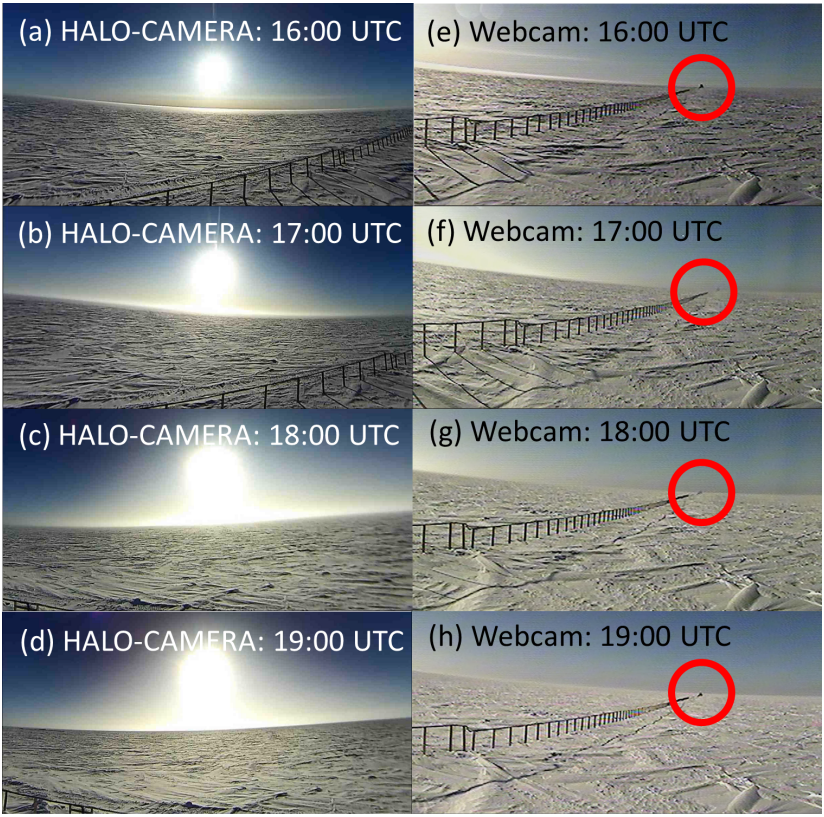

Figure 4.12.: Hourly photos are taken in the direction of the sun before **(a)**, during **(b)** and **(c)**, and after **(d)** the liquid fog event of 17 December 2023 taken with HALO camera [26]. Furthermore, hourly photos in the direction of a distant building before **(e)**, during **(f)** and **(g)**, and after **(h)** the liquid fog event are taken with a LIDAR supporting webcam by Massimo del Guasta. The red circle highlights a distant building that is visible before and after the liquid fog event and disappears during the event due to reduced visibility.

-40 °C. The Fourier classification Fig. 4.11c shows a generally higher fraction of spherical particles than the machine learning method. This is because it tends to falsely classify slightly elliptical frozen droplets as spherical particles. On 18 November 2023, at approximately local midnight, a similar event of homogeneously freezing supercooled liquid droplets was observed, which is shown in appendix A.4.

4.6. Comparison to previous studies of boundary layer ice particles

In this chapter, the microphysical properties at Dome C were compared for different types of boundary layer ice particle events. Existing definitions of ice fog and diamond dust events do not clearly separate their microphysical properties. Therefore, we used a LIDAR to manually identify low-level ice fog events and streaks of ice particles from higher altitudes that can be cirrus precipitation or diamond dust. This classification is based on the definitions of the American Meteorological Society and the World Meteorological Organisation, which both define ice fog as a fog of suspended ice particles and diamond dust as ice crystals falling from a cloudless sky [3, 2, 171, 170]. This type of classification is supported by the distinct differences that were found between the microphysical properties of ice fog and cpdd events.

The found modal maximum at approximately 70 µm of the cpdd mode agrees well with the diamond dust size parametrisation by [49]. Our findings of cpdd particle sizes furthermore agree well with the particle size distributions of diamond dust particles measured with the Cloud Particle Imager (CPI) at South Pole station by [85], taking into account that the particle maximum dimension measured with CPI can be 1 to 2.5 times the spherical equivalent diameter measured with PPD-2K (see appendix A.2). Here we note that the classification of diamond dust during the observations at South Pole station also included events of particle precipitation, when scattered, thin clouds were present, similar to the cpdd class in this work.

The mean particle concentration of $1.04\,\mathrm{L}^{-1}$ during cpdd events recorded at Dome C is in good agreement with the particle concentration of the diamond dust parametrisation by [49]. Nonetheless, it is lower than particle concentrations of diamond dust measured with CPI at South Pole Station by [85], which showed concentrations of up to $10^3\,\mathrm{L}^{-1}$. Altogether, the microphysical properties of the cpdd class ice particles mostly align with previous measurements of diamond dust. This shows that the potential cirrus seeding of the diamond dust during the cpdd events only has a minor contribution to the microphysical properties of ice particles in the measurement size range of PPD-2K.

The ice fog size mode with a modal maximum below the lower size detection limit of PPD-2K of 11 µm is consistent with the ice fog size parametrisation of

[49], which states that ice fog particle sizes are smaller than 30 µm. However, the mean particle concentration of ice fog events at Dome C of $3.8\,L^{-1}$ is lower than the minimum particle concentration of ice fog events of $1 \cdot 10^3\,L^{-1}$, according to the parametrisation of [49]. There are multiple reasons that can explain why the observed ice fog particle concentration is lower than expected.

One reason is that the ice fog particle size distribution increases down to the lower size detection limit of PPD-2K at 11 µm. Therefore, the ice fog modal maximum is likely at smaller diameters than 11 µm. However, particles that are smaller than 11 µm are not considered in the particle concentration measured with PPD-2K. This means that the overall ice fog particle concentration, including the particle sizes smaller than 11 µm, is likely higher than the PPD-2K measurements. This is supported by the lower observed particle concentrations of ice fog at Fairbanks with PPD-2K by [133] in comparison to previous concentration measurements using formvar replicas and video imaged particles [134]. Nonetheless, the mean ice fog particle concentration at Fairbanks is with $7.7 \cdot 10^1\,L^{-1}$ approximately twenty times the ice fog particle concentration at Dome C with $3.8\,L^{-1}$.

A second reason for the low ice particle concentrations is the dry atmosphere with low aerosol concentration on the Antarctic plateau, where almost no local aerosol emission from anthropogenic or biological activity exists [60, 71]. The polar vortex is much stronger than in the Arctic, limiting intrusions of non-polar air masses with higher aerosol load [165]. The low aerosol concentration on the Antarctic plateau causes a low INP concentration, which leads to reduced heterogeneous nucleation of ice particles.

The mean summer particle mass concentrations of particles with aerodynamic sizes of up to 10 µm (PM_{10}) at Dome C is approximately is with $0.1\,\mu g\,m^{-3}$ [4] much lower than at Fairbanks, where during ice fog periods PM_{10} regularly exceeds $5 \cdot 10^4\,\mu g\,m^{-3}$ [89]. This is caused by anthropogenic aerosol and water vapour emissions from fossil fuel burning for heat and power generation in Fairbanks [134, 133]. Consequently, the measured INP concentrations on the Antarctic plateau of approximately $10^{-6}\,L^{-1}$ to $10^{-3}\,L^{-1}$ at -20 °C [174, 166, 128] are lower than Arctic INP concentrations of approximately $10^{-1}\,L^{-1}$ to $10^3\,L^{-1}$ at -20 °C [119, 11, 89].

During ice fog at Fairbanks, morphologically more complex ice particles were found with a mean k_e of 4.35 and a high fraction of rough particles of 43 % in comparison to ice fog at Dome C with a mean k_e of 4.26 and a fraction of

rough particles of 2 %. Similarly rough ice particles at high concentrations were only observed at Dome C during test operation of PPD-2K in the vicinity of the exhaust plumes ofConcordia station's generators (not shown). The higher morphological complexity observed in Fairbanks can be attributed to the high water vapour emissions. Higher relative humidity during growth conditions increases the particle growth speed, which leads to a more complex growth regime [6, 135].

It can be concluded that a different concentration definition of Antarctic ice fog is needed, because lower particle concentrations persist for ice fog on the Antarctic plateau. For an exact definition, long-term measurements with a size range down to a few micrometers are required. Furthermore, year-round measurements would be valuable to analyse the effect of different seasons and to limit the effect of the sun's radiation on the ice particles. The analysis in this work is limited by continuous (polar day) sunlight during the measurements at Dome C in contrast to a daily maximum of seven sun hours during the wintertime measurements at Fairbanks. For wintertime measurements at Dome C an instrument is needed that can withstand the harsh conditions with temperatures down to -80 °C and limited access.

4.7. Nucleation of Antarctic ice fog

The nucleation of ice fog on the Antarctic plateau is an open question [55, 154]. Heterogeneous nucleation and homogeneous freezing are possible pathways for the nucleation of ice fog. [55] suggests that ice fog is often nucleated heterogeneously because of high ice fog occurrence at temperatures higher than -30 °C. In contrast, it was concluded from LIDAR, temperature, and humidity measurements that a local ice fog event at Dome C likely originated from homogeneous freezing, but no direct proof was found [154]. Homogeneous freezing of supercooled fog has been observed indirectly with radar and temperature measurements on the ice sheet of Greenland when the air temperature dropped below -40 °C near ground level [17]. Therefore, this can possibly also occur at similar conditions on the Antarctic ice sheet. Our in situ observations with PPD-2K support the hypothesis of homogeneous freezing as a common pathway for the formation of local ice fog on polar ice sheets. The observed sudden increase in the fraction of frozen particles during the liquid fog event of 17 and 18 December 2023 at temperatures of

approximately -38 °C is the first in situ observation of homogeneous freezing of liquid fog near ground level. The observations show that homogeneous freezing is a pathway for the formation of locally formed ice fog on the Antarctic plateau.

The freezing of supercooled liquid cloud droplets has been simulated in the AIDA cloud simulation chamber in similar conditions to the observed freezing event at Dome C. The homogeneous freezing temperature for experiment 17 in [70] is at -36 °C and thus approximately 3 °C higher than the natural observations at Dome C. The lower freezing temperature at Dome C can be caused by a lower water activity in the fog droplet. Aerosol measurements at Dome C showed that the main component of the aerosol fine and coarse mode is sulfate with a weight fraction of non-sea salt SO_4^{2-} of 99.5 % in the fine mode and 92.3 % in the coarse mode [35]. The sulfate can be the reason for a lower water activity and reduced temperature of homogeneous freezing at Dome C in comparison to the laboratory experiments at the AIDA cloud simulation chamber. To investigate this further, a chemical analysis of supercooled liquid droplets at Dome C is needed.

A second sign of homogeneous freezing was the short, significant increase in ice particle morphological complexity during the initiation of the ice fog event starting on 25 November 2023 at Dome C at temperatures near ground level below -40 °C. The high fraction of rough ice particles is an indicator of homogeneous freezing [150].

Both findings support the hypothesis of [154] that homogeneous freezing is a common pathway for the nucleation of locally formed ice fog on the Antarctic plateau. For more detailed information, ice particle measurements down to smaller sizes, as well as simultaneous measurements of the INP concentration, are needed.

4.8. Summary

The in situ measurements of boundary layer ice crystal size and concentration at Dome C showed a particle size mode at approximately 70 µm for cirrus precipitation and diamond dust events, which was not present during ice fog events. Ice fog events were dominated by a smaller particle size mode with modal maximum diameters below the lower size detection limit of 11 µm

of PPD-2K. The particle size modes measured at Dome C are in agreement with a size parametrisation of ice fog and diamond dust in Arctic regions by [49].

The mean particle concentration of ice fog events at Dome C ($3.8\,L^{-1}$) was higher than that of cpdd events at Dome C ($1.0\,L^{-1}$). Furthermore, the mean particle concentration of ice fog events at Dome C ($3.8\,L^{-1}$) was found to be lower than for ice fog events at Fairbanks, Alaska, ($7.7 \cdot 10^{1}\,L^{-1}$), and also lower than a common concentration parametrisation of Arctic ice fog ($>10^{3}\,L^{-1}$) [49]. These findings can prove useful for the validation of satellite remote sensing data of ice particle sizes and concentrations on the Antarctic plateau.

Investigating the ice particle morphological complexity, it was found that ice fog particles at Dome C are more pristine than ice fog particles observed at Fairbanks. This emphasises the need for a separate microphysical parametrisation of inland Antarctic ice fog. It also highlights the difference between ice fog that forms on the clean and dry Antarctic plateau and ice fog formed in an urban, polluted environment.

Signs of homogeneous freezing as a nucleation pathway of Antarctic ice fog were observed in situ during a multi-day ice fog event initiated at -44 °C and a freezing supercooled fog event at air temperatures down to -39 °C.

Our findings of boundary layer ice particle microphysics on the Antarctic plateau are important to improve the ice particle parametrisation in climate models of Antarctica, adding to the few in situ measurements that exist in the remote region. A next step would be to implement the findings of microphysical properties into a radiative transfer model, e.g. ecRAD. Additionally, an analysis of the radiative effect of the events of supercooled liquid fogs is necessary because both have been shown to have high radiative impacts [83, 118, 50].

A depolarisation LIDAR was used in this chapter to identify different ice particle events in the atmosphere. Yet, the link between the ice particle microphysical properties and the LIDAR measured backscattering linear depolarisation ratio (δ) is unclear. In the next chapter, we will investigate in laboratory experiments under controlled particle growth conditions how the ice particle microphysical properties affect δ.

5. Depolarisation properties of small cirrus ice crystals

In this chapter, the link between the near-backscattering linear depolarisation ratio δ and the microphysical properties —such as the particle size, shape, and small-scale complexity— of small ice crystals is investigated using 47 cloud chamber-grown cirrus clouds. With sizes below approximately 70 µm the ice particles were in a similar size range as the Antarctic ice fog particles that were studied in chapter 4. The analysis uses all available data from measurement campaigns HALO06, RICE01, RICE02 and RICE03, which took place at the AIDA cloud simulation chamber facility in Karlsruhe between January 2011 and December 2014 at temperatures between -75 °C and -39 °C. During the experiments, the particle size was measured with PPD-2K as the spherical equivalent diameter. The particle complexity was detected with SID-3 as the small-scale complexity parameter k_e and the particle shapes are derived from the SID-3 diffraction patterns. Additional information about the fraction of columns and the fraction of columns that have hollow basal faces is obtained from a manual analysis of microscope images of formvar replicas, which were captured during the cloud chamber experiments. The near-backscattering linear depolarisation ratio δ is measured with the SIMONE instrument. The measurement data of δ is compared to geometrical optics ray tracing and numerically exact T-matrix light scattering simulations, taking into account different methods to model ice crystal complexity, including surface roughness, different aspect ratios, air inclusions, and hollowness on the basal faces.

5.1. Previous studies on the link between ice crystal morphology and depolarisation lidar measurements

Ice cloud can easily be identified on atmospheric LIDAR measurements because non-spherical ice particles alter the polarisation of the incident light during the backscattering process [90]. The relation between the backscattering linear depolarisation ratio and the ice particle size and shape is highly complex, which makes the retrieval of the ice crystal morphology from lidar measurements challenging [123]. Using two-year global data measured with the CALIPSO satellite, a decrease in backscattering linear depolarisation ratio for increasing cloud altitude and decreasing temperature was observed [127]. A strong correlation between temperature and linear depolarisation ratio was found by [125]. This highlights that models that use a vertically homogeneous ice crystal habit distribution are inappropriate for radiative transfer calculations.

Numerical models can reproduce the atmospheric findings. A shape classification technique for hexagonal ice crystals has been introduced that identified higher depolarisation ratios with higher aspect ratios (columns) and lower depolarisation ratios with lower aspect ratios (plates) [113]. Four different classes of hexagonal ice crystals with different aspect ratio ranges were identified from LIDAR measurements based on ray tracing simulations of pristine hexagonal ice particles. Furthermore, geometrical optics simulations show that the backscattering linear depolarisation ratio oscillates with size for pristine columns in a size range between 10 µm and 1000 µm, which may enable the retrieval of size information from backscattering linear depolarisation measurements [82].

However, it is highly uncertain if these results of idealised pristine crystal geometries are applicable to atmospheric observations. Recent studies show that cirrus clouds rarely consist of ice crystals with idealised hexagonal shapes but almost always contain some degree of morphological complexity [69]. The effect of particle size and surface roughness on the backscattering linear depolarisation ratio has been simulated using improved geometrical optics and IITM simulations of hexagonal ice crystals with an aspect ratio of one [120]. It was found that ice crystal surface roughness strongly affects the linear depolarisation ratio of the backscattered light, and that ice crystal

surface roughness is needed to reproduce atmospheric observations. A lower backscattering linear depolarisation ratio was also found for bullet rosette ice crystals with hollow basal faces in comparison to solid ones, using improved geometrical optics ray tracing simulations [178]. The hollow bullet rosettes furthermore showed a decreasing trend in linear depolarisation ratio with particle size in contrast to the solid ones. For columnar ice particles, hollowness on the basal faces has been shown to decrease the linear depolarisation ratio in ray tracing simulations [143], but also to increase it when averaged over an ensemble of particles with different sizes and lengths of hollowness [181].

Cloud chamber experiments are useful to study the linear depolarisation ratio of ice crystals for well-defined particle growth conditions and to validate the numerical simulations. It has been shown that the linear depolarisation ratio in the near-backscattering direction (178°) reaches high values of up to 0.4 for sublimating small ice crystals (< 10 µm) in a temperature range between -50 °C and -70 °C [136]. Moreover, large differences between the linear depolarisation ratio from ray tracing simulations of pristine hexagonal ice particles and cloud chamber measurements in the near-backscattering (178°) and backscattering (180°) have been observed for ice particles with sizes between 20 µm and 200 µm at temperatures between -30 °C and -7 °C [143].

5.2. Data processing

Particle size distributions with 50 size bins are calculated from the PPD-2K particle size measurements. The size bins range from approximately 7 µm to approximately 70 µm, with small differences between the campaigns, due to the campaign-specific size calibrations and amplification gain settings. Log-normal particle size distributions n are fitted to the data [37, 148]:

$$n(d) = \frac{n_0}{\sqrt{2\pi} \cdot d \cdot \log \sigma} \cdot e^{\left(-\frac{\log^2 \frac{d}{GMD}}{2 \log^2 \sigma}\right)} \tag{5.1}$$

with particle diameter d, geometric mean diameter GMD, standard deviation σ of the logarithm of the particle diameter, and total concentration n_0. For the investigated AIDA measurement campaigns, the mean σ of all GMD is 1.26 ± 0.13. For all $GMD < 10$ µm the mean σ is 1.21 ± 0.07.

Table 5.1.: AIDA measurement campaigns used for the analysis of the link between ice crystal morphology and linear depolarisation ratio.

Campaign	Time	SIMONE wavelength	Size from	Number of experiments analysed
HALO06	Jan–Feb 2011	488 nm	FTIR	11
RICE01	Nov 2012	488 nm	PPD-2K	9
RICE02	Apr–May 2014	488 nm	PPD-2K	14
RICE03	Dec 2014	552 nm	PPD-2K	13

During the HALO06 campaign instead of PPD-2K and SID-3 a Fourier transform infrared spectrometer (FTIR) was operated to determine the particle sizes down to a maximum particle dimension of approximately 1 µm [159]. The FTIR measured the spectral extinction of the ice particles in the spectral range between 800 cm^{-1} and 6000 cm^{-1}. Similar to the procedure in [136], for the retrieval of the *GMD* from the measured extinction spectra a log-normal particle size distribution was assumed and T-matrix calculations of cylindrical particles with an aspect ratio of 0.7 were used. With the exemption of highly irregular particle shapes, the extinction spectra at mid-infrared wavelengths only vary slightly with particle shape. Details of the investigated measurement campaigns are shown in table 5.1. The subsequent analysis uses 10 s averaged data from SIMONE, FTIR, PPD-2K, and SID-3 where the following criteria are met:

- The gas temperature in the AIDA cloud simulation chamber is below -39 °C.
- The expansion has started.
- The SIMONE forward scattering intensity is high enough that δ can be retrieved accurately. The threshold values are 10^6 counts for SIMONE and 10^4 counts for SIMONE-Junior. An automated neutral density filter system is used in both SIMONE instruments to avoid saturation of the detector and obtain measurements in an increased intensity range. The counts measured with a neutral density filter are normalised to the measurements without neutral density filters.
- The *GMD* determined from the log-normal fit is at most 20 % smaller than the center of the smallest PPD-2K size bin: $1.2 \cdot d_{\min} \leq GMD$. This

conditions ensures a reliable *GMD* retrieval. The center of the smallest size is between 6.4 µm and 7.9 µm depending on the photomultiplier gain setting and the campaign specific size calibration.

- The particle concentration is higher than 0.3 cm^{-3} to ensure that the particle size distribution consists of enough particles for an accurate log-normal function fit.

Thus, 24 % of the data are omitted due to PPD-2K limitations. This is predominantly due to low particle concentrations during the sublimation phases of the regrowth experiments (for more details about the cloud chamber experiment procedure see section 3.4).

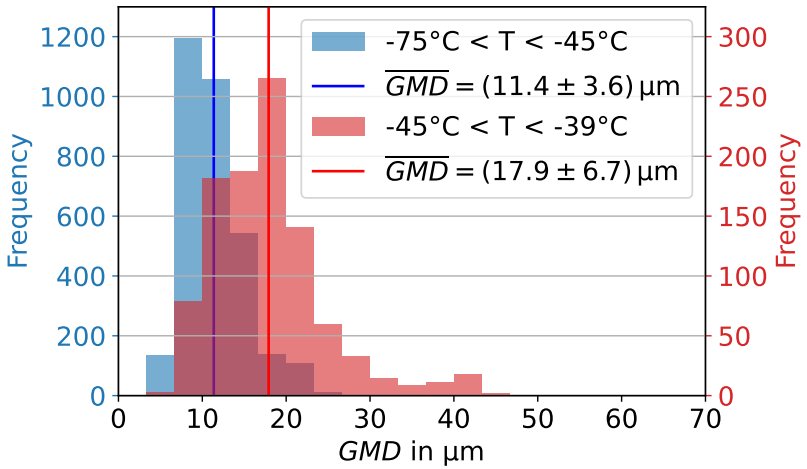

Figure 5.1.: Histograms of geometric mean diameter (*GMD*) for AIDA experiments with initial gas temperatures between -75 °C and -45 °C (blue) and between -45 °C and -39 °C (red). The mean *GMD* of ice particles grown in the lower cirrus temperature range is 39 % smaller than of ice particles grown in the higher cirrus temperature range.

5.3. Microphysical properties of the cloud chamber grown ice clouds

Ice particles with spherical equivalent diameters of up to 70.5 µm were grown during expansion experiments in the AIDA cloud simulation chamber at gas temperatures below -39 °C. A histogram of the particle size for initial gas temperatures ($T_{gas,i}$) between -75 °C and -45 °C (blue) and between -45 °C and -39 °C (red) is shown in Fig. 5.1. In the lower cirrus temperature range the mean *GMD* is (11.4 ± 3.6) µm. This is 36 % smaller than the mean *GMD* of the ice particles grown at the higher cirrus temperature range with (17.9±6.7) µm. Larger particle sizes at higher temperatures are expected because the growth rate of ice crystals increases with increasing temperature at constant relative humidity [6]. The upper size limit of approximately 70 µm of ice particles observed during the experiments is due to increasing sedimentation loss in the cloud chamber with increasing particle sizes caused by higher fall speeds.

Microscope images of the formvar replicas were taken during regrowth phases with constant relative humidity. The aim was to investigate differences in ice crystal growth characteristics during constant growth conditions. The subsample of expansion experiments with regrowth phases with constant relative humidity is shown in table 5.2 and table 5.3. The analysis consists of nine regrowth experiments from measurement campaigns RICE01 and RICE03 with $T_{gas,i}$ of -40 °C and -50 °C and relative humidity with respect to ice (RH_{ice}) between 105 % and 120 % during the regrowth phases. For each image that usually contained some tens of ice crystals, the number of columnar and hollow columnar ice crystals was counted manually. In total, on 324 microscope images, 11096 ice crystals were visually analysed. 29.4 % of the ice crystals had columnar shapes, and 70.6 % of the ice crystals had other, mainly irregular shapes. The fraction of columns needs to be considered as a lower limit because it is not always possible to visually clearly identify the particle shape from the microscope images of the formvar replicas due to blurriness or possible artifacts in the replica. Exemplary replicator images are shown in Fig. 5.2a-e. The other shapes were predominantly compact crystals. Some ice crystals also resembled budding bullet rosettes with several c-axes radiating from a center point (e.g. Fig. 5.2c,e).

The fraction of replicas classified as columnar is shown in table 5.2 and table 5.3. The column fraction at -40 °C ranged between 12 % and 25 %. No clear

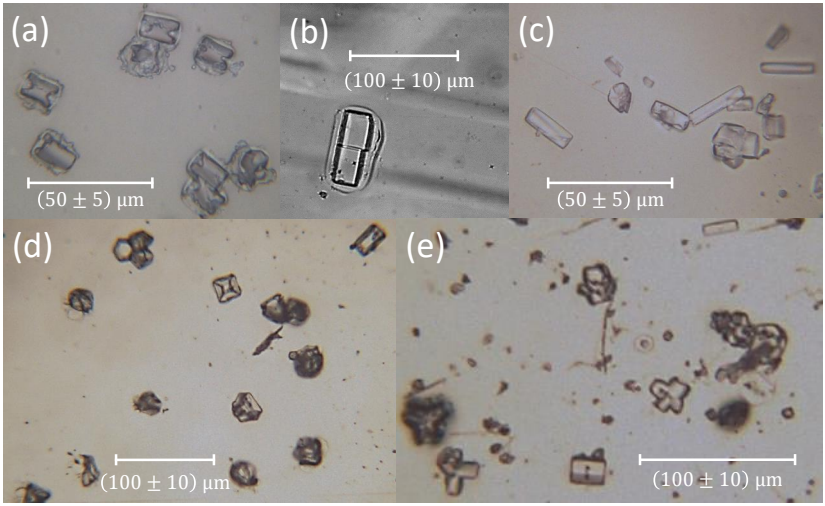

Figure 5.2.: Microscopic images of formvar replicas of the cloud chamber grown ice particles showing different types of ice crystal complexity. The ice crystals in **(a)** are hollow on the basal faces or have air inclusions. In **(b)** a columnar particle with a central dislocation can be seen. **(c)** and **(d)** show columnar and irregular shaped ice crystals. In **(e)** (budding) bullet rosettes can be seen. **(a)** and **(c)** were captured during RICE03 experiments 40 and 38 at supersaturations of 16 % and 12 % with respect to ice, respectively, and initial gas temperatures ($T_{gas,i}$) of -50 °C. **(b)** was captured during RICE01 experiment 22 at $T_{gas,i}$ of -50 °C and a supersaturation of 4 % with respect to ice. **(d)** and **(e)** were captured between during RICE03 experiments 29 and 32 at supersaturations of 4 % and 10 % with respect to ice, respectively, and $T_{gas,i}$ of -40 °C.

trend between the relative humidity with respect to ice and the fraction of columnar particles was seen. The columnar growth regime at temperatures below -40 °C is expected by previous studies. For example, for supersaturations below 25 % mainly single columns and for higher ice supersaturation (budding) rosettes were reported by [6]. The supersaturation is the relative humidity exceeding saturation at $RH = 100\,\%$.

At -50 °C the fraction of columnar ice crystals was higher than at -40 °C. It ranged from 23 % at $RH_{ice} = 105\,\%$ to 59 % at $RH_{ice} = 120\,\%$ increasing with rising supersaturation. Our measurements are in agreement with [6], who reported more columnar ice crystals at -50 °C in comparison to the transition region between columnar and plate-like particle growth at -40 °C. Furthermore, we observed a transition towards more columnar particles with increasing relative humidity at -50 °C for $RH_{ice} < 130\,\%$, which is also in

Table 5.2.: The total number of investigated ice particle relica (N_{tot}), the fraction of columnar particles of the total number of replicas (f_{col}) and the fraction of hollow columnar particles of all columnar particles (f_{hollow}) are given. They are determined from visual analysis of the microscope images of formvar replicas taken during the regrowth phases with constant relative humidity with respect to ice (RH_{ice}) at initial gas temperatures of -40 °C. The fraction of columnar particles during the regrowth phases of the experiments derived from the SID-3 diffraction patterns f_{col} (SID-3) are added as a comparison.

Campaign	RICE01	RICE03		
Experiment	27	29	30	32
T_{gas} in °C	-40	-40	-40	-40
N_{tot}	508	787	764	1516
f_{col}	25 %	22 %	12 %	17 %
f_{col} (SID-3)	42 %	24 %	23 %	19 %
f_{hollow}	45 %	33 %	73 %	36 %
RH_{ice} mean	120 %	105 %	107 %	111 %

Table 5.3.: The total number of investigated ice particle relica (N_{tot}), the fraction of columnar particles of the total number of replicas (f_{col}) and the fraction of hollow columnar particles of all columnar particles (f_{hollow}) are given. They are determined from visual analysis of the microscope images of formvar replicas taken during the regrowth phases with constant relative humidity with respect to ice (RH_{ice}) at initial gas temperatures of -50 °C. The fraction of columnar particles during the regrowth phases of the experiments derived from the SID-3 diffraction patterns f_{col} (SID-3) are added as a comparison.

Campaign	RICE01	RICE03			
Experiment	20	38	39	40	41
T_{gas} in °C	-50	-50	-50	-50	-50
N_{tot}	424	1350	1113	638	406
f_{col}	23 %	4 %	39 %	42 %	59 %
f_{col} (SID-3)	39 %	25 %	43 %	43 %	47 %
f_{hollow} %	12 %	4 %	36 %	70 %	29 %
RH_{ice} mean	105 %	109 %	108 %	112 %	120 %

agreement with [6]. The fraction of columnar particles derived from the Fourier analysis of the SID-3 diffraction patterns is added in table 5.2 and table 5.3.

The analysis of the SID-3 diffraction patterns with the method by [156] allows a statistically more robust investigation of the ice crystal shapes. 0 % of the particles detected at cirrus temperatures during the expansion experiments

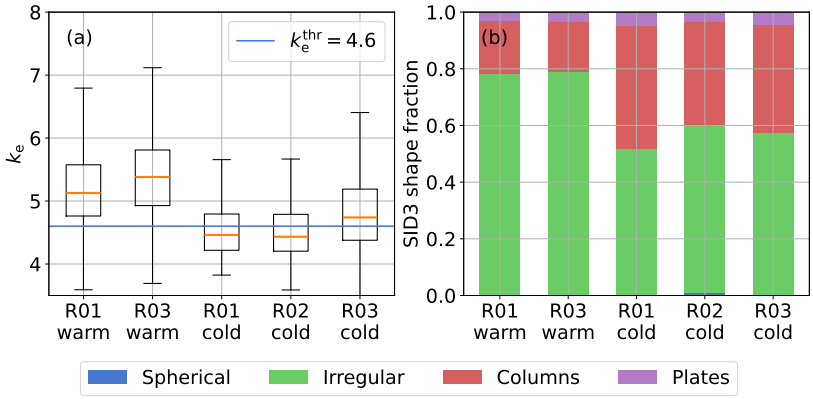

Figure 5.3.: Small-scale complexity parameter k_e derived from the GLCM speckle pattern analysis for the different RICE campaigns (R) and temperature ranges **(a)**. Cold refers to AIDA initial gas temperatures between -75 °C and -45 °C and warm refers to AIDA initial gas temperatures between -45 °C and -39 °C. In **(b)** the particle shape fractions are shown for the different cirrus temperature ranges and measurement campaigns. They are determined using the method by [156] for forward scattering images taken with the SID-3 instrument.

show diffraction patterns of spheres, 4 % of plates, 35 % of columns, and 61 % of irregular particles. This agrees well with the fraction of columnar and irregular particles that were determined by visual analysis of the ice crystal replicas during the regrowth phases of a subsample of the experiments. Fig. 5.3b shows the habit fractions for the different measurement campaigns and the two cirrus temperature groups. The fraction of columns between -75 °C and -45 °C (labelled 'cold') is with 44 % (RICE01), 36 % (RICE02) and 38 % (RICE03) higher than between -45 °C and -39 °C (labelled 'warm') with 15 % (RICE01) and 18 % (RICE03). This increasing trend of the fraction of columnar particles with decreasing temperature was already seen in the visual analysis of the formvar replicas.

The formvar replicas show different types of morphological complexity. The most abundant are hollowness on the basal faces and occasional air inclusions. These can be seen in Fig. 5.2a and in Fig. 5.2d, respectively. The fraction of columnar formvar replicas that show hollowness on the basal faces for $T_{gas,i}$ of -40 °C is given in table 5.2. It ranges between 33 % at RH_{ice} = 105 % and 73 % at RH_{ice} = 107 %. The mean fraction of columns that show hollowness at an $T_{gas,i}$ of -40 °C is 46 %. The fraction of columnar ice crystal replicas

that show hollowness on the basal faces at $T_{gas,i}$ of -50 °C is shown in table 5.3. It varies between 4 % at RH_{ice} = 109 % and 70 % at RH_{ice} = 112 % with a mean of 40 %. Only for experiments with $T_{gas,i}$ of -50 °C do the fractions of columnar ice crystal replicas that show hollowness fall below 30 %. The observation of a substantial fraction of hollow columns at both investigated cirrus temperatures is in contrast to a laboratory study by [59]. They estimated a critical supersaturation of at least 20 % for ice crystals to develop hollowness on the basal faces at temperatures below -40 °C. The fraction of columns that show hollowness in this study needs to be considered as a lower limit because it is not always possible to visually identify hollowness in the microscope images of the formvar replicas. Previous studies of atmospheric cirrus also observed hollowness in columnar ice particles. An analysis of microscope images of ice crystal precipitation at South Pole station between -73 °C and -35 °C found all bullets but only a few columns to be hollow [162]. Formvar replicas from balloon-borne mid-latitude cirrus observations between -46 °C and -33 °C showed hollow ends on 50 % to 80 % of all bullet-rosettes and columnar ice particles [131]. Our cloud chamber observations show a smaller fraction of hollow columnar particles in comparison to the atmospheric observations.

A dislocation is another type of ice crystal complexity that was observed on the formvar replicas. An example can be seen in Fig. 5.2. A dislocation can form from thermal stress caused by the changing growth conditions during the experiments [7].

The microscope analysis of the formvar replicas does not allow for conclusions about sub-micron scale complexity like surface roughness. Limiting factors are the optical resolution of the microscope and the replication technique. The complexity information derived from the SID-3 diffraction patterns can yield additional information. A statistical analysis of the small-scale complexity parameter k_e can be seen in Fig. 5.3a for the different measurement campaigns and temperature groups. In the lower cirrus temperature range between -75 °C and -45 °C the median k_e is with 4.54 below the threshold of k_e^{thr} = 4.6 defined for ice particles with a high degree of small-scale complexity ('rough') by [135]. The median k_e of 5.22 at the higher cirrus temperature range between -45 °C and -39 °C is above the threshold of ice particles with a high degree of small-scale complexity. This is in good agreement with [135] who suggested that higher growth rates at higher temperatures promote the growth of ice particles with a higher degree of small-scale complexity. There are also minor differences seen in median k_e and in the fraction of shapes be-

tween the different measurement campaigns at the same temperature groups. The median k_e is higher during RICE03 in comparison to RICE02 in both temperature ranges. Different relative humidity during the expansion experiments of the different measurement campaigns can cause this. Hereafter, the size-dependent linear depolarisation ratio (δ) of the cloud chamber grown cirrus clouds is analysed separately for the two temperature ranges.

5.4. The link between particle size and the linear depolarisation ratio

Fig. 5.4 shows the linear depolarisation ratio δ as a function of the *GMD* for the two different temperature ranges that were defined in the previous section. For the temperature range between -45 °C and -39 °C a minimum in δ is observed at a *GMD* of approximately 12 µm (see Fig. 5.4a). δ increases for smaller and larger *GMD* to values up to 0.3. For AIDA $T_{gas,i}$ between -75 °C and -45 °C (see Fig. 5.4b) a constant δ between 0.05 and 0.10 is measured for *GMD* between 8 µm and 25 µm during measurement campaigns RICE01, RICE02, and HALO06. A sharp increase in δ to values of up to 0.5 is observed for particles smaller than 8 µm. Only the measurement data from the RICE03 measurement campaign show an increasing trend in δ with *GMD* at the lower cirrus temperature range. This is likely due to more complex ice crystals in the lower temperature range during RICE03 in comparison to RICE01 and RICE02, as seen in Fig. 5.3.

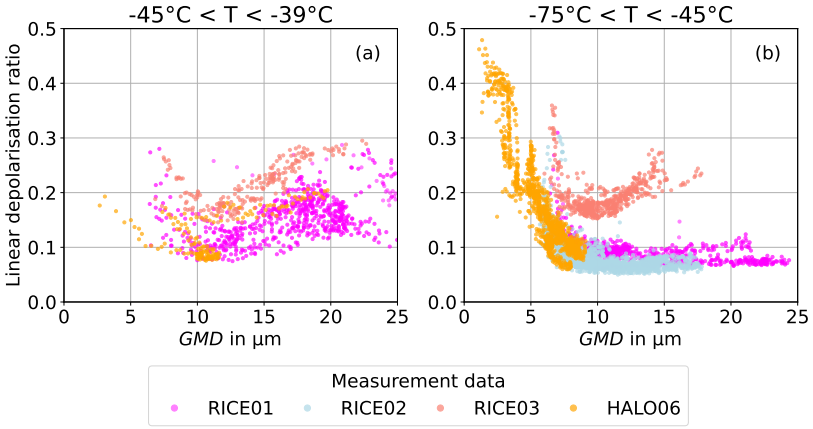

Figure 5.4.: The linear depolarisation ratio δ from SIMONE as a function of the geometric mean diameter (*GMD*) measured with PPD-2K and FTIR for time averages of 10 s. **(a)** shows the measurement data for initial gas temperatures between -45 °C and -39 °C and **(b)** between -75 °C and -45 °C for the measurement campaigns RICE01, RICE02, RICE03 and HALO06. The data are measured during multiple grow and sublimation phases at different relative humidity.

5.5. The influence of the ice particle small-scale complexity on the linear depolarisation ratio

Fig. 5.5 shows δ as a function of the small-scale complexity parameter k_e at cirrus temperatures between -75 °C and -39 °C. The measurement data are shown separately for the measurement campaigns RICE03 in Fig. 5.5a, RICE02 in Fig. 5.5b, and RICE01 in Fig. 5.5c. Pearson correlation coefficients (R) are determined, and a linear function fit is added. The results are calculated separately for different size groups of (5 ± 1) µm, (10 ± 1) µm, (15 ± 1) µm, (20 ± 1) µm. This is done to limit the possible effect that the particle size has on δ. A weak to moderate positive correlation of $0.21 \leq R \leq 0.61$ between δ and k_e was found during RICE01 at $-50\,°C \leq T_{gas,i} \leq -39\,°C$. In contrast, during RICE02 at $T_{gas,i}$ of -50 °C and during RICE03 at $-50\,°C \leq T_{gas,i} \leq -40\,°C$, no or only a weak correlation of $|R| \leq 0.16$ was observed.

The weak to moderate correlation between δ and k_e seen in only one of the three measurement campaigns is an unexpected finding. It is thought that increasing ice crystal morphological complexity in the size range between

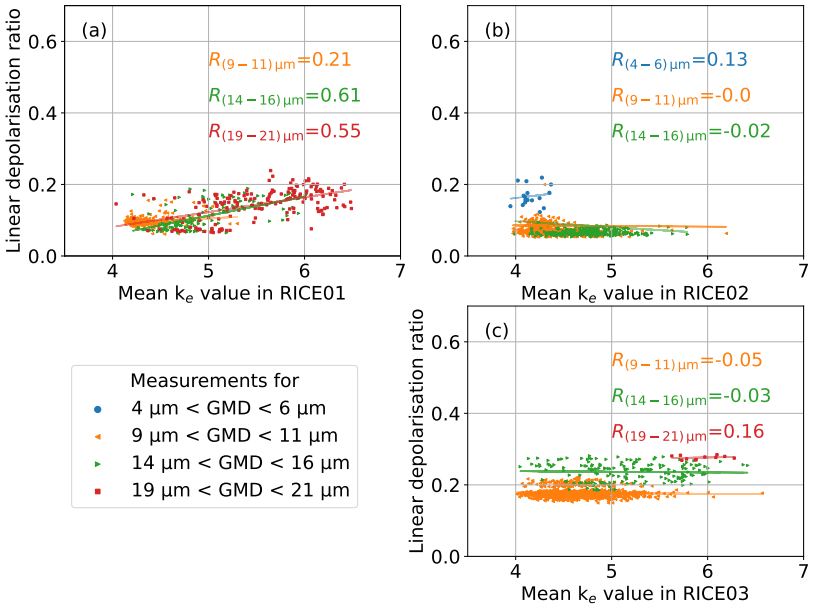

Figure 5.5.: The linear depolarisation ratio δ as a function of the small-scale complexity parameter k_e for measurement campaigns RICE03 **(a)**, RICE02 **(b)**, and RICE01 **(c)**. The measurement data uses an integration time of 10 s. Linear fits and a correlation analysis are added. Only a weak to moderate correlation is found.

5 µm and 20 µm increases the linear backscattering depolarisation ratio δ. This is shown by ray tracing simulations [143] and IITM simulations [120] for ice crystal morphological complexity in the form of surface roughness. Therefore, a stronger correlation between the small-scale complexity and δ was expected. A possible explanation is that the most pristine ice crystals with the lowest surface roughness cannot be grown in the cloud chamber expansion experiments. The most pristine ice crystals need long growth times at slow growth speeds, which cannot be reached in the AIDA cloud simulation chamber due to sedimentation losses. Due to the absence of the most pristine ice particles, it is possible that a certain degree of ice crystal morphological complexity was reached, beyond which further increases cause only minimal effects on δ. This plateau in δ is observed for a degree of surface roughness larger than approximately 0.1 in [120].

Another reason can be that the small-scale complexity parameter k_e is not suitable to find this correlation. Possibly, other morphological features, for example the aspect ratio, have a strong effect on δ but simultaneously a small effect on k_e. This emphasises the complex relationship between the ice crystal microphysical properties and δ. In the next section, the measurement data will be compared to ray tracing and T-matrix simulations.

5.6. Comparison of the measurements to light scattering simulations

This section compares δ of the cloud chamber grown cirrus clouds to T-matrix simulations of spheroids, geometrical optics ray tracing Monte Carlo simulations of hexagonal particles and IITM simulations of hexagonal particles.

5.6.1. Comparison to T-matrix simulations

The linear depolarisation ratio measured with SIMONE in the AIDA cloud simulation chamber is compared to T-matrix simulations of ice particles with spheroidal shape based on the model of [107] and a python implementation by [87]. Computational limitations constrain the T-matrix simulations to size parameters below approximately 50. The bulk scattering δ is calculated according to equation 2.23 and 2.24 for 41 particle sizes between 0.5 µm and 10.0 µm with a fixed σ of 1.21 at a scattering angle of 178°. This is the mean σ of all particle size distributions with *GMD* smaller than 10 µm measured with PPD-2K during the measurement campaigns. The aspect ratio is varied between 1.5 and 2.0, which is the range of aspect ratios of columns found on the microscope images of the formvar replicas.

Fig. 5.6 shows the results of the T-matrix simulations together with the measurement data from the AIDA cloud simulation chamber campaigns for the previously defined two temperature groups. The highest simulated values of δ occur for the smallest simulated particle sizes of approximately 2 µm with values exceeding 0.5. For increasing particle sizes, δ decreases with particle size. Furthermore, the simulations show a decrease in δ with increasing aspect ratio for particles with sizes larger than approximately 3 µm. The simulated δ reproduces the trend of the measurement data well, especially

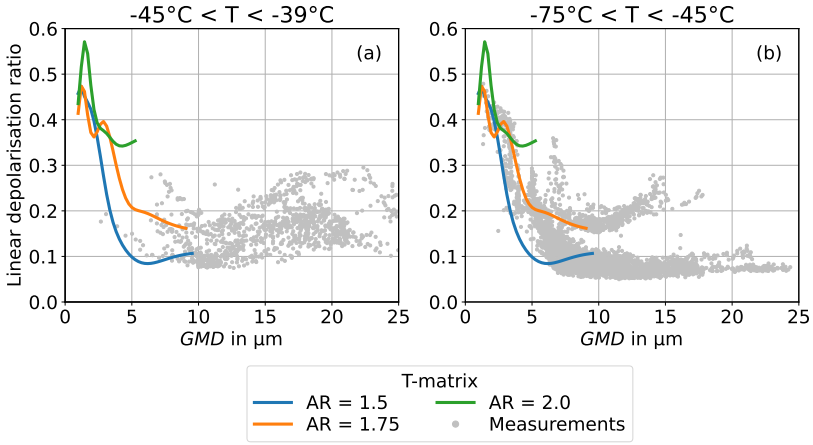

Figure 5.6.: T-matrix simulations of ice particles with spheroidal shape (lines) are compared to measurement data (dots) of the linear depolarisation ratio δ as a function of the geometric mean diameter (GMD). The experimental data at initial gas temperatures between -45 °C and -39 °C is shown in **(a)** and between -75 °C and -45 °C in **(b)**.

for the assumptions of aspect ratios of 1.50 and 1.75. It can be noted that the majority of ice particles in the size range of the T-matrix simulations are observed in the lower cirrus temperature range between -75 °C and -45 °C.

5.6.2. Comparison to geometrical optics ray tracing simulations

For particles with size parameters larger than approximately 90, the geometrical optics approximation can be applied. In this size range, we use a conventional geometrical optics ray tracing method [97, 98, 99], which was run for randomly oriented hexagonal particles with 2 million orientations. The bulk scattering matrix elements are calculated from the single size scattering matrix elements with an integration over the log-normal particle size distribution. The used σ of 1.26 is the mean σ of all log-normal function fits to the particle size distributions measured with PPD-2K during the investigated cirrus experiments. The bulk scattering size integration is performed with 42 particle size bins between 8.4 µm and 37.3 µm. Ice crystal morphological complexity is implemented in the ray tracing simulations with the tilted facet

approach, internal scatterers, and hollowness on the basal faces. For the tilted facet method, the distortion parameter describes a maximum random tilt that is applied to the ice crystal surface when a ray hits. A distortion parameter of 0 is equivalent to no tilt, and a distortion parameter of 0.5 is equivalent to a maximum random tilt of up to 45°. The internal scatterers are characterised by a mean free path. This is the mean distance a ray propagates before a random simulated internal scattering event. During an internal scattering event, the ray randomly changes the direction of propagation. In this work, the internal scatterers are quasi non-absorbing with a single-scattering albedo of 0.999, representative of air bubbles. Hollow columns are simulated with a hollowness depth of 33.3 % of the crystal length from each basal face (see Fig. 5.8c). This type and length of hollowness is consistent with the hollowness seen on the microscope images of the formvar replicas (e.g. Fig. 5.2a).

Fig. 5.7 shows the simulated δ at 178° near-backscattering direction for solid columns with distortions between 0.0 and 0.5 and an aspect ratio of 1.5, together with the measurement data from the AIDA cloud simulation chamber. The ray tracing simulations with the assumption of solid columns return δ values above 0.5, overestimating δ from AIDA cloud simulation chamber measurements.

Mean free paths of 150 µm and 10^4 µm are applied. A mean free path of 150 µm represents a high amount of internal scatterers, and a mean free path much larger than the particle dimensions of 10^4 µm represents negligible internal scattering. In contrast to the case of negligible internal scattering, for high internal scattering the simulated δ slightly increases with increasing particle size. The increase in δ with particle size for a high amount of internal scatterers can be explained by the consequent increase in direction changes of the ray, which randomises the polarisation information and thus increases δ. In addition, δ has a local minimum of approximately 0.5 for a distortion of 0.3 and increases especially for lower distortions. Aspect ratios of 1.75 and 2.0 yield similar results to the shown aspect ratio of 1.5 (see appendix B.1).

An improved parametrisation of the ice crystal morphology is needed to achieve better agreement with the measurement data. In the following, hollow basal faces with a length of 33.3 % of the crystal length are added to hexagonal ice particles. The modeled ice particle structure is shown in Fig. 5.8c). This type of hollowness is regularly seen in the microscope images of the formvar replicas in Fig. 5.2. Fig. 5.8 shows δ for the hollow columns with mean free paths between 500 µm and 10^4 µm and distortions between 0.0 and 0.5. An

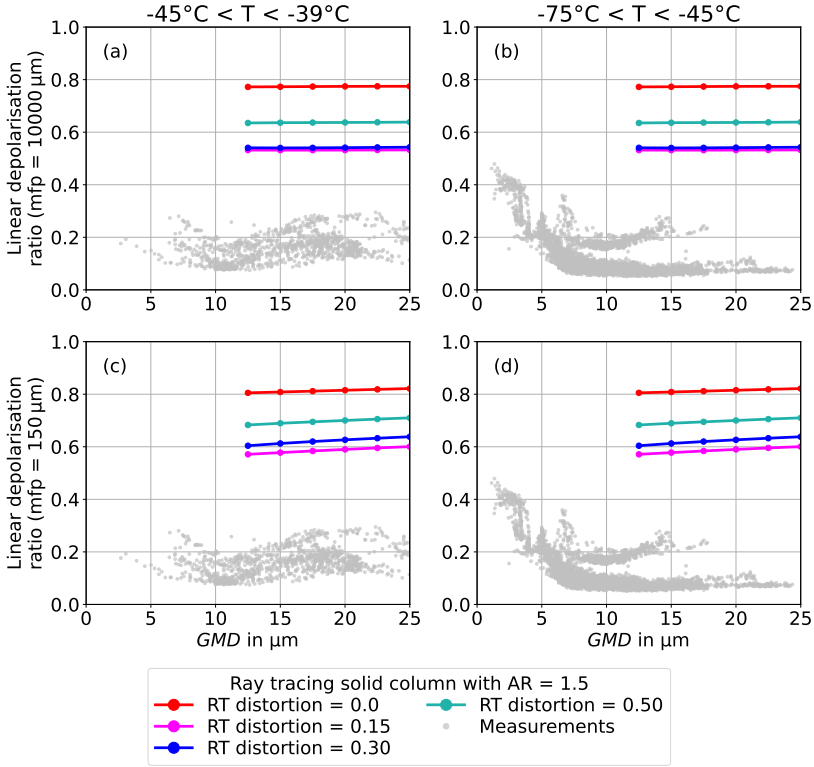

Figure 5.7.: Ray tracing simulations of solid hexagonal ice crystals (lines) are compared to measurement data (dots) of the linear depolarisation ratio δ at the near-backscattering direction of 178°. The data is shown as a function of geometric mean diameter (GMD)[97]. The distortion parameter is varied between 0.0 and 0.5. Mean free paths between 150 µm (**a**) and (**b**) and 10^4 µm (**c**) and (**d**) are used. The experimental data at initial gas temperatures between -45 °C and -39 °C is shown in **(a)** and between -75 °C and -45 °C in **(b)**. The simulations of hollow columns overestimate the measurement data.

increasing mean free path causes an increase in δ for all simulated sizes. For hollow columns, the mean free path has a larger effect on δ in comparison to solid columns, likely caused by the overall lower δ.

The hollow basal faces lower δ to the range of the measurement data, likely caused by the additional planar surfaces of the ice crystal. As a result, the simulations of hollow columns with a mean free path of 2000 µm reproduce

the measurement data of δ in the warmer cirrus temperature range between -45 °C and -39 °C. Using a mean free path of 4000 µm yields results similar to the measurement data of δ at the colder cirrus temperatures between -75 °C and -45 °C.

An aspect ratio of 1.5 is used, but the simulation data are almost identical for aspect ratios of 1.75 and 2.0 (see appendix B.1). In addition, the results of the ray tracing simulations are almost identical for the wavelength of 552 nm used by SIMONE-Junior. Details and the effect of different depths of hollowness are given in appendix B.1.

The measurement data can only be reproduced by the ray tracing simulations when the tilted facet approach, internal scattering, and hollow basal faces are used to model ice crystal morphological complexity. This emphasises the need to sufficiently implement ice crystal morphological complexity in light scattering simulations. However, conventional geometrical optics are limited to particle sizes where the geometrical optics approximation holds (size parameters larger than approximately 10^2). For smaller sizes, numerically exact light scattering simulations are needed. The numerically exact IITM method is an option and will be compared to the measurement data from the AIDA cloud simulation chamber in the next section.

5.6.3. Comparison to IITM simulations

Fig. 5.9 shows δ at the near-backscattering direction of 178° from IITM simulations at a wavelength of 488 nm [58] together with the SIMONE measurement data. The simulations use the refractive index of ice at a wavelength of 532 nm, which is very similar to the refractive index at 488 nm. δ is integrated over a log-normal particle size distribution with 31 particle sizes between 0.1 µm to 24.6 µm. For particle sizes of up to 10 µm σ of 1.21 is used, and for larger particle sizes σ of 1.26 is used. The aspect ratio is varied between 1.0 and 2.0. Ice particle morphological complexity is implemented as the degree of surface roughness σ^2, which is the variance of a two-dimensional Gaussian distribution of local planar surface slopes.

From values close to zero at particle sizes smaller than 1 µm, δ sharply increases for increasing particle sizes. At particle sizes of approximately 3 µm δ plateaus with smaller variations with particle size. Depending on σ^2 and the aspect ratio, δ ranges between approximately 0.2 and 0.5 on the plateau.

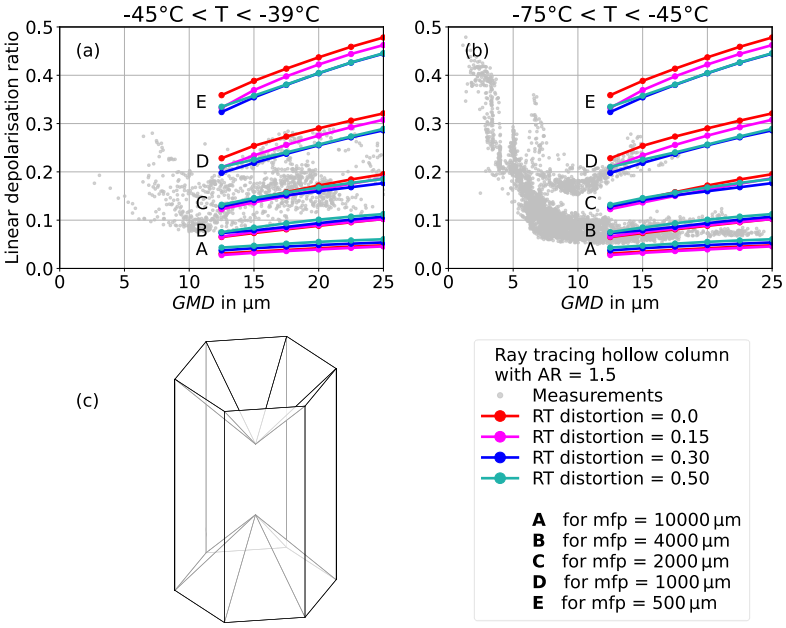

Figure 5.8.: Ray tracing simulations of hollow hexagonal ice crystals (lines) are compared to measurement data (dots) of the linear depolarisation ratio δ as a function of geometric mean diameter (GMD) at the near-backscattering direction of 178° [97]. The distortion parameter is varied between 0.0 and 0.5. Mean free paths between 500 µm (**A**) and 10^4 µm (**E**) are used. The experimental data at initial gas temperatures between -45 °C and -39 °C is shown in **(a)** and between -75 °C and -45 °C in **(b)**. The simulations reproduce the measurement data for mean free paths of 4000 µm and 2000 µm for the warmer and colder cirrus temperature regimes, respectively. The geometry of the ice crystals with a hollowness depth of 33.3 % from each basal face is shown in (**c**).

For particle sizes larger than approximately 3 µm δ increases with surface roughness, while for smaller sizes, δ is almost independent of surface roughness. The computational effort of the IITM simulations strongly increases for aspect ratios departing from one. Therefore, the simulations of aspect ratios of 1.5 and 2.0 are only available for particle sizes up to approximately 9 µm. An increase in aspect ratio causes a slight increase in δ. The IITM simulations almost always overestimate δ measurements of the cloud chamber experiments. Only the simulations of the most pristine case ($\sigma^2 = 0$) with

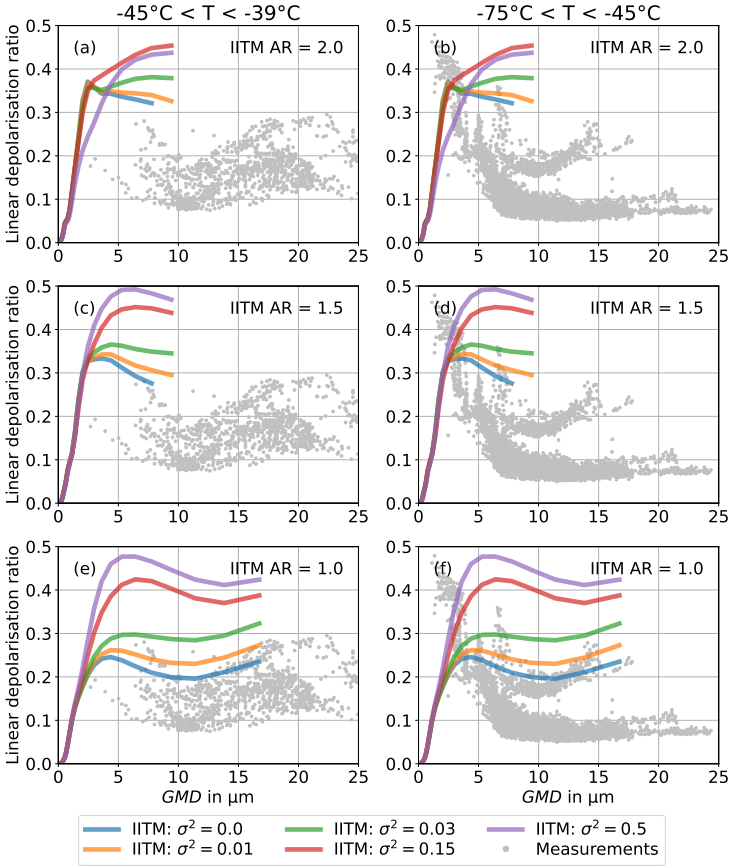

Figure 5.9.: Measurement data (dots) of the linear depolarisation ratio δ at the near-backscattering direction of 178° as a function of geometric mean diameter (GMD) are compared to IITM simulations with an aspect ratio of one (lines) by [58]. The surface roughness variance σ^2 of the simulations is varied between 0 and 0.5. **(a)** shows the AIDA measurement data at initial gas temperatures between -75 °C and -45 °C and **(b)**between -45 °C and -39 °C.

aspect ratio one overlap with parts of the measurement data. This contrasts with the findings of the microphysical properties of the ice crystals, where most of the ice crystal replica images and diffraction patterns showed at least some degree of morphological complexity.

The difference between the measurement data and the IITM simulations of δ can be attributed to the used ice crystal morphological complexity model. The ice crystal replica analysis revealed that many ice crystals exhibited additional features of morphological complexity, like air inclusions and hollowness, which are not implemented in the IITM model. For example, the ray tracing simulations could only reproduce the measurement data when these additional complexity features were added in the crystal model. Adapting the ice crystal morphological complexity model in the IITM simulations further, e.g. by implementing hollowness features, may improve agreement with the measurement data.

5.7. Atmospheric implications

The AIDA cloud simulation chamber observations of δ at different temperatures are shown in Fig. 5.10. The cloud chamber observed δ is lower than mid-latitude atmospheric measurements (grey shaded area), except for the experiments at the coldest temperatures at approximately -70 °C. A mean δ of 0.33±0.11 was observed for mid-latitude cirrus, measured with a ground-based LIDAR at a wavelength of 694 nm by [124]. Similar results were observed by the CALIPSO space-borne LIDAR at a wavelength of 532 nm with a daytime global cirrus clouds mean of 0.34 [127]. However, the nighttime global cirrus cloud mean of $\delta = 0.24$ is closer to our cloud chamber findings. Yet, according to the authors, the lower nighttime values are caused by background signals from Rayleigh scattering of the atmosphere. Other mid-latitude LIDAR studies report cirrus δ in the range between approximately 0.2 and 0.5, e.g. [153, 88].

For polar cirrus clouds in a similar temperature range, ground and satellite-based observations showed lower δ in comparison to mid-latitude cirrus with mean δ between approximately 0.1 and 0.4 [22, 23, 125]. During our cloud chamber observations, δ ranged between approximately 0.08 and 0.3 at GMD below approximately 70 µm. This range of δ is lower than mid-latitude observations but in good agreement with atmospheric polar observations. The common occurrence of diamond dust and ice fog particles at sizes smaller than 100 µm in polar regions [162, 55] is a possible explanation for the good agreement between the cloud chamber and previous polar observations.

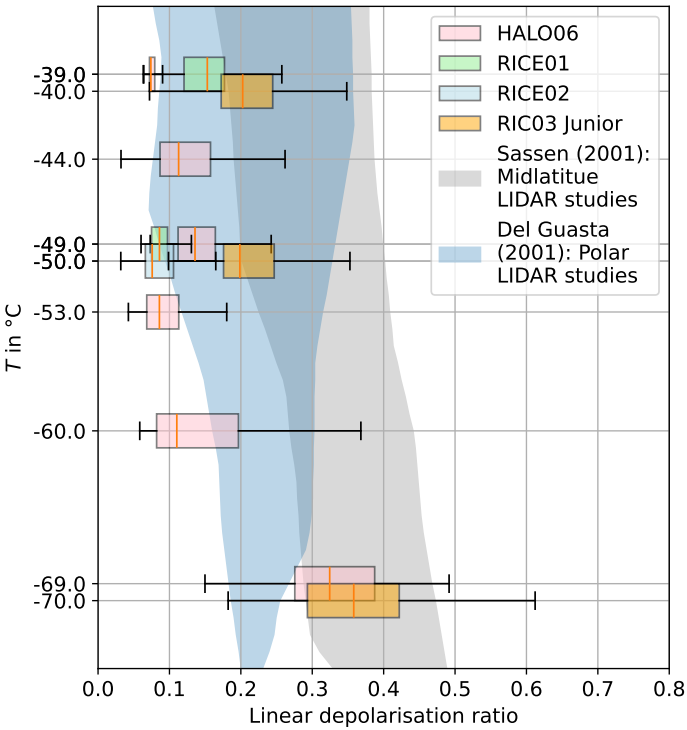

Figure 5.10.: Linear depolarisation ratio δ measured at different gas temperatures (T) during different measurement campaign at the AIDA cloud simulation chamber with the SIMONE instrument. Atmospheric LIDAR measurements of δ from tropical and mid-latitude studies [124] are added in grey and from polar studies [22] are added in blue as a reference. The observed mean AIDA clouds chamber δ are lower than the atmospheric tropical and mid-latitude observations between -60 °C and -40 °C but in agreement with polar studies.

While our cloud chamber cirrus measurements are restricted to relatively small ice crystals with *GMD* below approximately 70 µm, atmospheric cirrus cloud particle sizes regularly exceed 100 µm, especially for higher cirrus temperatures [110, 169, 20]. The backscattering linear depolarisation ratio

of four different cirrus clouds between -63 °C and -58 °C, observed during the CIRRUS in Mid-Latitudes (CIRRUS-ML) campaign, has been studied by [54]. δ was found to increase from 0.39 for the cloud with the smallest medium effective diameter of 52.2 µm to 0.52 for the cloud with the largest medium effective diameter of 193.8 µm. This increase in δ with particle size is consistent with our cloud chamber observations.

It is known that small ice crystals with sizes below 10 µm cause high δ [136]. This is in agreement with our observations of δ up to 0.45 for the smallest ice particles. The commonly observed high δ in lower cirrus temperatures in the atmosphere (e.g. [127, 88]) can be explained by the presence of small ice particles with sizes below 5 µm. Small ice particles with sizes between 1 µm and 10 µm have been observed in tropical tropopause cirrus clouds [169, 84]. They can be a driver of higher δ observed at lower latitudes, because deep convective systems that generate tropical tropopause cirrus occur at higher frequencies in lower latitudes [39]. Small ice particles also influence the δ measurements of contrail cirrus, where ice particles with sizes below 10 µm are abundant [142].

5.8. Limitations of the numerical simulations

The linear depolarisation ratio of laboratory grown ice crystals at -30 °C has been studied by [143] in the size range from approximately 20 µm to approximately 80 µm at a wavelength of 532 nm. A higher fraction of plate-like particles was observed on formvar replicas of the fall tube grown ice particles. In agreement with our cloud chamber observations, hollow basal facets and air inclusions were visible on the replicas of columnar ice particles. δ was observed between approximately 0.25 and 0.45 at the exact backscattering direction of 180° and between approximately 0.1 and 0.35 in the 178° near-backscattering direction. The results at 178° agree well with our SIMONE observations. This raises the question, which effect the measurement of δ at the near-backscattering direction of 178° has in comparison to the exact backscattering direction of 180° [136].

Fig. 5.11 shows the difference between δ at 180° and at 178°, simulated with ray tracing simulations of solid columns (Fig. 5.11a), with T-matrix simulations of spheroids (Fig. 5.11b), with ray tracing simulations of hollow columns (Fig. 5.11c), and with IITM simulations of solid columns. The ray tracing

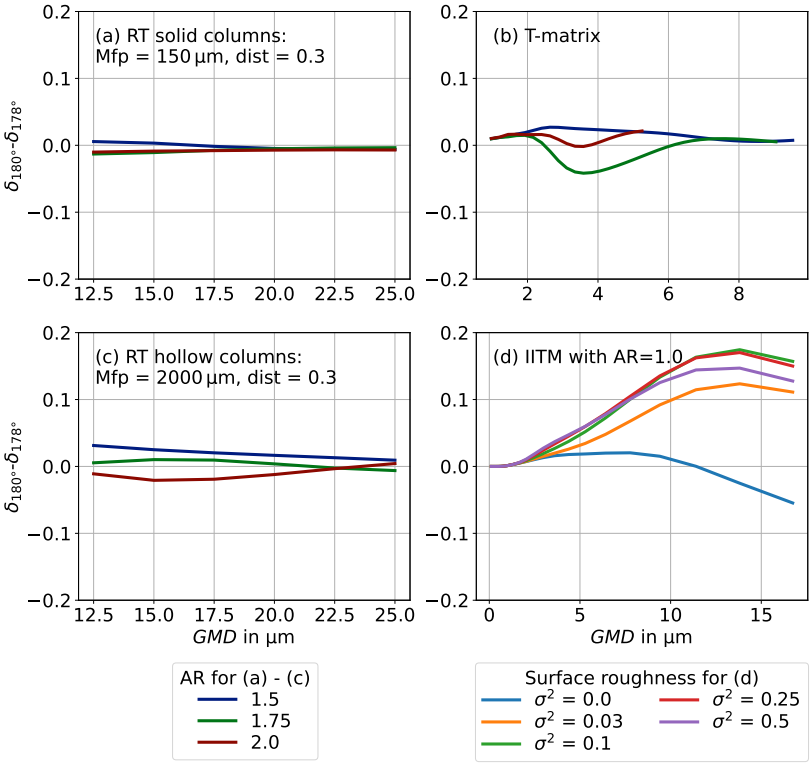

Figure 5.11.: The difference between the simulated linear depolarisation ratio δ at direct backscattering direction of 180° and near-backscattering at 178° is shown for T-matrix simulations **(a)**, ray tracing (RT) simulations with a distortion of 0.3 and a mean free path of 150 µm **(b)** and ray tracing (RT) simulations with a distortion of 0.3 and a mean free path of 10^4 µm **(c)**. The difference for IITM simulations with roughness variance σ^2 between 0 and 0.5 and an aspect ratio of one can be seen in **(d)**. The IITM simulations show the highest possible bias of up to 0.17 for GMD = 13.8 µm.

and T-matrix simulations have a difference of $\delta_{180°} - \delta_{178°}$ smaller than 0.04, which cannot explain the difference between our cloud chamber findings and atmospheric observations. However, the IITM simulations show a clear bias towards higher δ for roughened ice crystals at the direct backscattering direction of 180° (see Fig. 5.11d). The difference between δ measured at 180° and at 178° increases with increasing particle size. A maximum difference

of 0.17 is found for rough ice particles with a *GMD* of 13.8 µm. Therefore, it cannot be entirely excluded that the lower SIMONE observations of δ in comparison to atmospheric observations are due to the detection angle of 178° near-backscattering direction. It needs to be noted that this does not affect the comparison to the numerical simulations of δ, which were also performed at the 178° near-backscattering direction.

The observations of δ in the AIDA cloud simulation chamber suggest that more comprehensive optical models are needed to accurately reproduce δ of ice particles with a high degree of morphological complexity. The IITM simulations of hollow columns, which included only surface roughness, showed poor agreement with the measurement data. Meanwhile, the ray tracing simulations achieved good agreement when multiple scales and types of morphological complexity (hollow basal faces, tiled facet method, and internal scatterers) were incorporated in the ice crystals model. This supports the conclusion that it is critical for an accurate optical model to capture the full range of morphological complexity. However, the applicability of the used ray tracing simulation to polarimetric properties has been questioned. This is because changes in the polarisation caused by internal scatterers and interference effects from rays leaving the ice crystal are omitted in the ray tracing simulations [100, 143]. Furthermore, some approaches like the commonly used tilted facet method remain limited because they lack physical surfaces, which makes it challenging to relate them to observed, real ice crystal morphological complexity features [98, 92]. In addition, many complexity features occur in the size range of the wavelength of the incident light, which makes the representation of these types of morphological complexity questionable in a geometrical optical model. Overall, the findings show that a physically more realistic ice particle model is needed, which includes different shapes, surface roughness, and internal complexity to accurately simulate polarimetric light scattering properties.

5.9. Summary

This chapter investigated the relationship between the linear depolarisation ratio (δ) and the ice crystal microphysical properties for 47 cloud-chamber grown cirrus clouds with ice particle sizes below approximately 70 µm.

First, the microphysical properties are analysed. It was found that smaller and more pristine ice particles grow at lower cirrus temperatures between -75 °C and -45 °C in comparison to ice particles grown between -45 °C and -39 °C. Furthermore, it was observed that the fraction of hexagonal columnar particles increases with decreasing temperature from 19 % at -40 °C to 41 % at -50 °C, according to microscope images of formvar replicas taken during the regrowth phases of the experiments. At both temperatures, a significant fraction of at least 40 % of the hexagonal ice particles was observed to have hollow basal faces in contrast to previous studies.

Subsequently, the effect of the particle size on δ was investigated. Ice particles with sizes larger than 10 µm were observed to have δ lower than 0.3 during the cloud chamber measurements. This range of δ is lower than atmospheric LIDAR observations of mid-latitude cirrus but in good agreement with polar observations. Furthermore, two temperature dependent δ - size modes were found. During the cloud chamber measurements at temperatures below -45 °C, δ predominantly stayed constant with particle size. In the higher cirrus temperature range between -45 °C and -39 °C, the cloud chamber observations showed an increasing trend of δ with particle size. The measurement results in both temperature ranges were reproduced with geometrical optical rays tracing simulations of hollow columnar particles, using the tilted facet method and adding internal scatterers to simulate morphological complexity. The strong increase in δ with decreasing particle size for particles with sizes below 10 µm was reproduced with T-matrix simulations assuming spheroidal particle shape. Also, δ from recent IITM simulations of roughened hexagonal ice particles were compared with our AIDA measurements, but the IITM simulations overestimated δ by about 15 %. Adapting the ice crystal morphological complexity model further, e.g. by the implementation of hollowness, may give better agreement with the measurement data.

In addition, the link between the small-scale complexity parameter k_e, derived from the ice crystal diffraction patterns, and δ was investigated. No clear correlation was found. A possible reason can be that the cloud chamber grown ice particles already have a baseline roughness, which limits the range of the observed small-scale complexity to an extent that no correlation could be observed. It is also possible that non-constant morphological features that had little influence on k_e —like the particle aspect ratio— strongly affected δ, and therefore no clear correlation was found.

Sufficiently understanding the influence of ice particle size and morphological complexity on δ is important for the correct interpretation of remote sensing data from LIDAR instruments like [124, 116, 15]. With an improved remote sensing retrieval of small ice particle morphology, ice cloud parametrisations in climate models can be optimised. In addition, the measurements of the δ of small cirrus ice particles are useful for the validation of optical particle models at the limit of the geometrical optics approximation.

This chapter analysed how the microphysical properties of small ice particles influence δ. In the next chapter, we will investigate how the microphysical properties influence the radiative properties of small ice particles, aiming for an improved optical parametrisation of small ice particles in climate models.

6. Effects of ice particle growth conditions on the asymmetry parameter g

After the analysis of the polarisation properties of small ice particles in the previous chapter, we will now focus on the effects of the particle growth conditions and microphysical properties on the asymmetry parameter g, which strongly influences the radiative properties of cirrus clouds.

The RICE04 (Rough ICE 04) campaign took place in October 2023 at the AIDA cloud simulation chamber at the Karlsruhe Institute of Technology (KIT) with two objectives. The first, scientific objective was to study the impact of quasi-constant temperature and relative humidity during particle growth on g, which was measured with the new PHIPS-POL instrument. The second, technical objective was to test and characterise the new PHIPS-POL instrument in the cloud chamber for possible future airborne campaigns. The cloud chamber expansion experiments were conducted at initial gas temperatures of -40 °C and -50 °C and at relative humidity with respect to ice during the regrowth phase between 104 % and 142 %. The investigated cirrus cloud ice particles had maximum dimensions predominantly below 70 µm, which is similar to the boundary layer ice particles in chapter 4 and the cloud chamber-grown ice crystals in chapter 5.

6.1. Effects of cirrus microphysics on radiative forcing

Cirrus clouds commonly exist in the atmosphere with a global mean of up to 40 % [172, 126, 102] and thus have a major impact on Earth's climate [8, 179, 96, 168]. The warming or cooling effect that the cirrus clouds have on

the climate is quantified with the radiative forcing, which is the net induced change in radiative flux. The two-stream radiative transfer approximation is commonly used to determine the cloud radiative forcing in climate models [38, 19]. In the two-stream approximation, cirrus clouds are parametrised by the single scattering albedo, the extinction cross section, and the asymmetry parameter g. In the shortwave spectrum, g strongly depends on particle size, shape, and morphological complexity [68].

There are multiple ways to simulate the light scattering properties of ice particles, for example ray tracing simulations in the geometrical optics approximation like the Ray Tracing Monte Carlo (RTMC) method [98] or the Improved Geometrical Optics (IGOM) method [176]. Furthermore, there are numerically exact methods like the Inverse-Embedded T-Matrix method (IITM) [10] or the finite-difference time domain method [175]. However, optical simulations generally use simplified representations of the ice crystal morphological complexity [69, 160]. Therefore, atmospheric observations of g are needed to verify the assumptions about the ice crystal morphology taken in the numerical simulations [173].

Nonetheless, atmospheric measurements inherently occur under changing ice crystal growth conditions. The continuous variations in temperature and humidity in the atmosphere make the observation of a correlation between ice particle growth conditions and microphysical properties challenging [67]. Therefore, laboratory experiments are needed to enable the study of ice crystal microphysical and optical properties at quasi-constant growth conditions.

6.2. Temporal evolution of the regrowth experiments

Fig. 6.1 shows the temporal evolution of AIDA experiment 09 of measurement campaign RICE04 at an initial gas temperature of -40 °C as an example expansion experiment. The expansion follows the procedure detailed in section 3.4. When the expansion was started at measurement time $t = 0$ s the pressure inside the cloud chamber started to decrease (see Fig. 6.1a) and the relative humidity increased (see Fig. 6.1f). The ice cloud started to nucleate at approximately $t = 180$ s when the relative humidity with respect to ice (RH_{ice}) exceeded the aerosol-specific threshold for heterogeneous ice nucleation.

This can be noted by a decrease in relative humidity. The initial growth phase was stopped when the first ice particles grew to sizes in the detection limit of PHIPS-POL of approximately 25 µm at $t = 250$ s. Then, slightly sub-saturated conditions were set to remove the ice crystal morphological complexity, which was induced in the initial growth period, by sublimation. When the particle size had decreased by approximately 20 %, the regrowth period was started with another expansion at approximately $t = 550$ s. For experiment 09 the ice crystal growth was studied at a quasi-constant supersaturation of 22 % with respect to ice. The supersaturation is the relative humidity exceeding saturation at $RH = 100$ %. At approximately $t = 1300$ s most ice particles had sublimated out of the chamber and the expansion was stopped. Fig. 6.1 shows g and the ice crystal complexity parameter C_P, retrieved including and excluding the light scattering detector at a polar angle of 6°. C_P is a measure of the ice particle complexity derived from the angular scattering function[173]. There was good agreement between g including and excluding the 6° angular position, while C_P was significantly lower when the 6° angular position was included. It can be noted that C_P increased during the initial growth up to 0.42, decreased during the sublimation period to approximately 0.35, and increased again during the final growth period to a plateau at approximately 0.50. The values are given for the retrieval excluding the 6° angular position. g evolves complementarily. After a local minimum during the initial growth of approximately 0.75, it increased during the sublimation period to approximately 0.80, before decreasing again during the final growth period to a plateau at a value of approximately 0.70. This behaviour motivates section 6.4, where the differences in g and C_P during the growth and sublimation phases are analysed for all cirrus experiments conducted in the RICE04 measurement campaign.

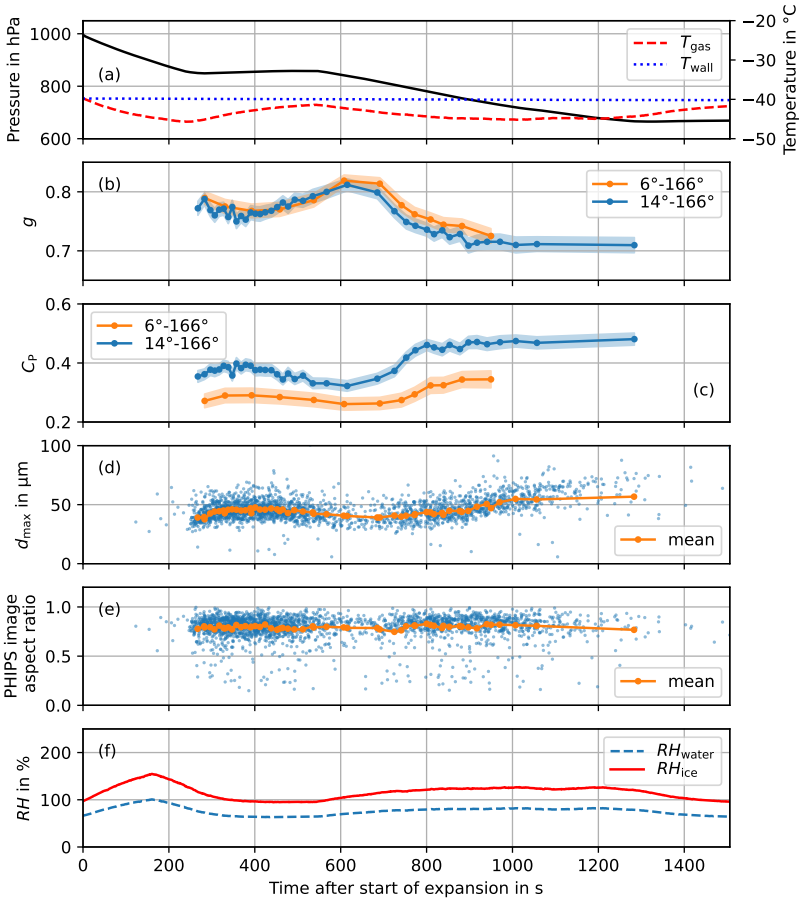

Figure 6.1.: Temporal evolution of optical and microphysical properties during expansion regrowth experiment 09 of the RICE04 campaign in October 2023 at the AIDA cloud simulation chamber. **(a)** shows the air pressure, gas temperature, and wall temperature of the cloud chamber. **(b)**-**(e)** show the temporal evolution of the asymmetry parameter (g), complexity parameter (C_P), diameter, and aspect ratio derived from the PHIPS-POL images. Means are calculated for sets of 50 detected particles. Labels 6° - 166° and 14° - 166° use the angular scattering function of 6° - 166° and 14° - 166°, respectively. **(f)** shows the relative humidity (RH) with respect to liquid water (RH_{water}) and ice (RH_{ice}).

6.3. Overview of optical and microphysical properties

Next, details about the microphysical properties of the cloud chamber-grown ice particles are given. During the regrowth experiments, ice particles with maximum dimensions (d_{max}) of up to 134.4 µm were measured with the stereoscopic images of PHIPS-POL. The mean of the maximum dimension ($\overline{d_{max}}$) of the complete experiments is with (41.6 ± 12.7) µm similar to $\overline{d_{max}}$ of the regrowth phases with (41.4 ± 13.4) µm (see Fig. 6.2a,b). Yet, the $\overline{d_{max}}$ of the regrowth experiments at initial gas temperatures (T_{gas}) of -40 °C is with (46.9 ± 12.3) µm 17.8 % larger than the $\overline{d_{max}}$ of the regrowth experiments at

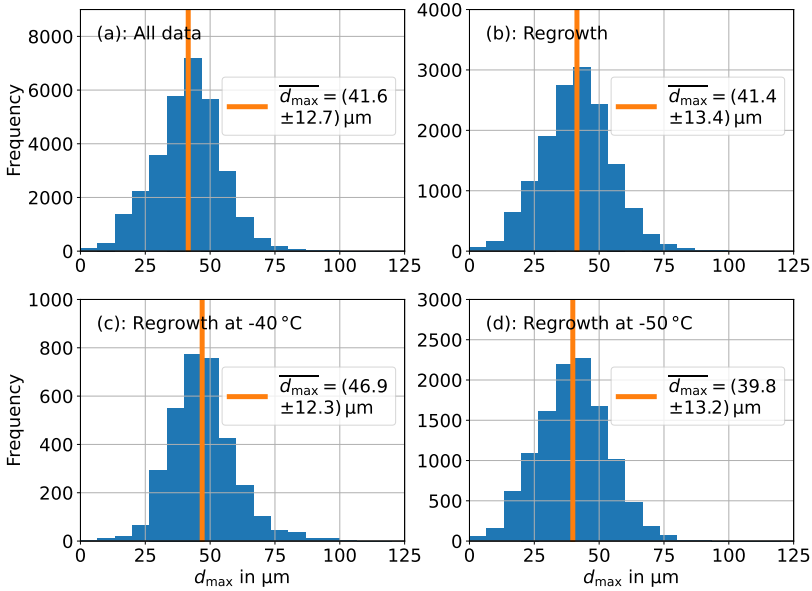

Figure 6.2.: Histograms of the particle maximum dimensions (d_{max}) derived from the stereoscopic images of PHIPS-POL during the RICE04 campaign at the AIDA cloud simulation chamber in October 2023. **(a)** shows d_{max} of the complete dataset, **(b)** shows d_{max} only from the regrowth phases at quasi-constant temperature and humidity, **(c)** shows d_{max} during quasi-constant regrowth at initial gas temperatures of -40 °C and **(d)** shows d_{max} during quasi-constant regrowth at initial gas temperatures of -50 °C. $\overline{d_{max}}$ is the mean of d_{max}.

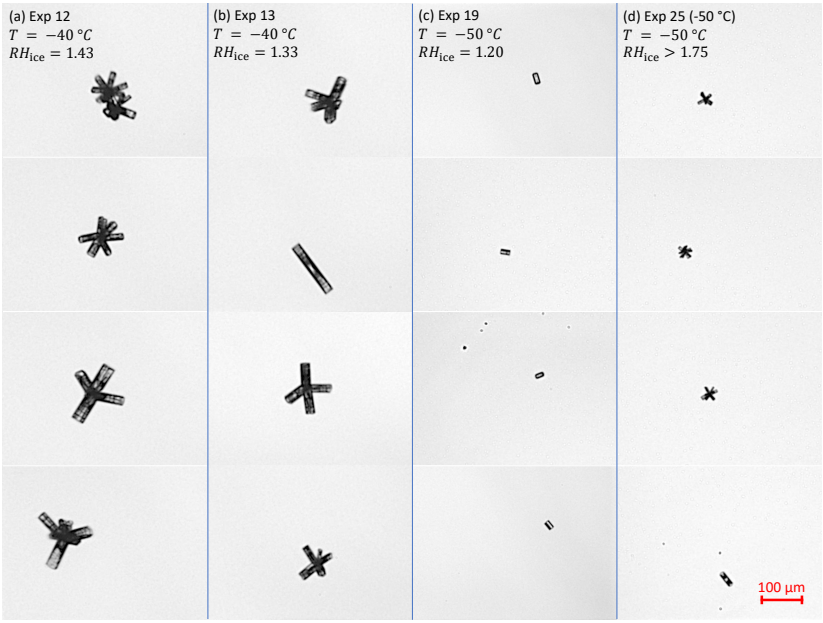

Figure 6.3.: Four example ice particle images are shown for different experiments of the RICE04 measurement campaign. **(a)** shows ice particles from experiment 12 at an initial gas temperature (T_{gas}) of -40 °C and RH_{ice} = 1.43, **(b)** shows ice particles from experiment 13 at T_{gas} of -40 °C and RH_{ice} = 1.33, **(c)** shows ice particles from experiment 19 at T_{gas} of -50 °C and RH_{ice} = 1.20, and **(d)** shows ice particles from experiment 25 at T_{gas} of -40 °C and RH_{ice} exceeding 1.75. It can be seen that the ice particles at -40 °C grow to larger sizes than at -50 °C.

initial T_{gas} of -50 °C with (39.8 ± 13.2) µm (see Fig. 6.2c,d). The larger mean size of ice particles grown at higher temperatures is expected due to the increasing growth rate of ice with increasing temperature at constant relative humidity [6]. There is an upper size limit of ice particles that can be grown in the AIDA cloud simulation chamber due to sedimentation. In the previous chapter, this limit was estimated to be approximately 70 µm, which is in good agreement with the upper particle size limit in the histograms in Fig. 6.2.

Besides size information, also shape information can be obtained from the stereoscopic images of PHIPS-POL. The ice particles during RICE04 had mainly columnar shapes with single hexagonal columns as well as budding bullet rosettes. A collage of sample images is shown in Fig. 6.3. It can be seen

that the ice particles tend to grow to larger sizes at an initial gas temperature (T_{gas}) of -40 °C, compared to those grown at T_{gas} of -50 °C. Furthermore, there are predominantly single columns in experiment 19 ($T_{gas} = -50$ °C and $RH_{ice} = 1.20$), whereas during experiment 25 ($T_{gas} = -50$ °C and $RH_{ice} > 1.75$) a higher fraction of bullet rosettes was observed. The change to a growth regime of bullet rosettes at higher relative humidity at a temperature of -50 °C is consistent with the observations of [6].

The asymmetry parameter g and complexity parameter C_P are derived from the angular scattering function (see also retrieval method in section 3.1.4). The 6° channel has a high background intensity due to its proximity to the laser beam and the beam dump, which makes the reliability of the data from this channel questionable (see calibration in section 3.1.3). Therefore, g and C_P are calculated separately for the angular scattering functions with polar angles between 14° and 166°, and with polar angles between 6° and 166°. Fig. 6.4a and Fig. 6.4b show histograms of g and C_P for the angular scattering functions between 6° and 166°. Fig. 6.4c and Fig. 6.4d show histograms of g and C_P for the angular scattering functions between 14° and 166°. Table 6.1 shows the mean values of g and C_P calculated for the complete experiments (All data) and for the regrowth phases only (Regrowth). While the difference in g between including and excluding the 6° channel is 0.01 and smaller, there is a difference of up to 0.06 for C_P.

The different behaviour of g and C_P can be explained by the definition of g as the first moment (first expansion coefficient) of the angular scattering function. It is a measure of how much light is scattered in the forward direction with reference to the backward direction. In contrast to g, C_P uses all moments (all expansion coefficients) and therefore also needs a larger angular range of the angular scattering function to be accurately retrieved. The additional detection at 6° allows the retrieval of C_P values lower than 0.4. Yet, this only has a limited effect on the retrieved values of g.

In this chapter, the angular scattering function between 14° and 166° is used for the retrieval of g and C_P for multiple reasons:

- The large uncertainty associated with the 6° position of the angular scattering function induces additional measurement uncertainty to the retrieved g
- 79.6 % of the measured particles have saturated channels including the 6° position, while only 61.2 % of the measured particles have saturated

Table 6.1.: Overview of observed asymmetry parameter (g) and complexity parameter (C_P) of the ice particles measured with PHIPS-POL during the RICE04 measurement campaign.

		Analysis of scattering function 14°-166°	Analysis of scattering function 6°-166°
All data	Mean g	0.74 ± 0.03	0.74 ± 0.03
	Mean C_P	0.44 ± 0.04	0.40 ± 0.05
Regrowth	Mean g	0.72 ± 0.02	0.73 ± 0.02
	Mean C_P	0.47 ± 0.03	0.41 ± 0.06

channels excluding the 6° position of the angular scattering function. Therefore, the sample size is higher when excluding the 6° channel.

- When including the 6° position of the angular scattering function, there is an additional bias because particles with a high intensity of scattered light at the near-forward direction, and thus a high g, tend to be saturate the detector at the 6° position and get thus excluded from the analysis.

Nonetheless, the following analysis of the growth conditions on g and C_P was also performed including the 6° channel. The corresponding figures are shown in appendix C.2.2.

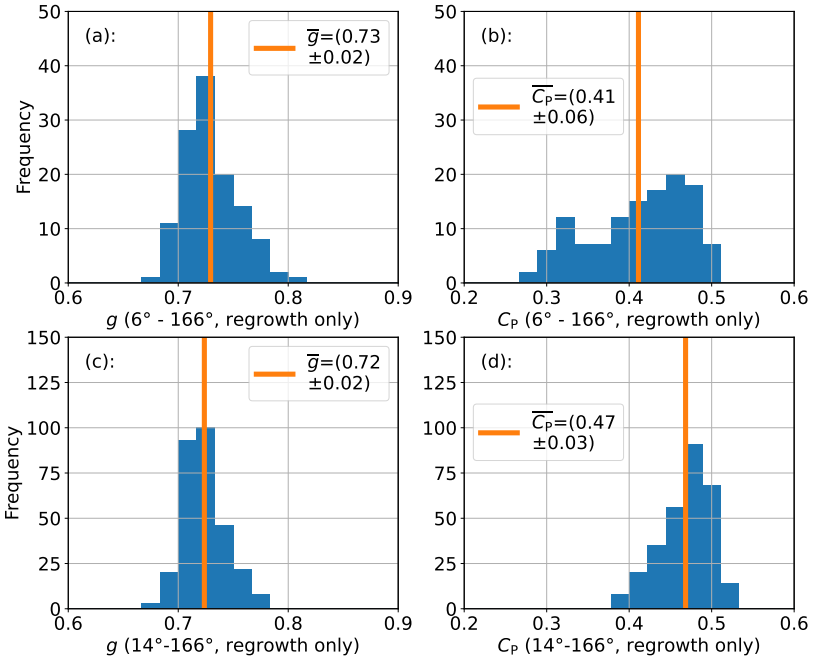

Figure 6.4.: Histograms of the asymmetry parameter (g) and the complexity parameter (C_P) derived from the angular scattering function of PHIPS-POL with the method of [173] during the RICE04 campaign at the AIDA cloud simulation chamber in October 2023. **(a)** shows g using the angular scattering function from 6° to 166°, **(b)** shows C_P using the angular scattering function from 6° to 166°, **(c)** shows g using the angular scattering function from 14° to 166° and **(d)** shows C_P using the angular scattering function from 14° to 166°. Only the regrowth periods of the experiments at quasi-constant temperature and humidity are used for the analysis. The mean values of g and C_P are given as $\overline{g}$ and $\overline{C_P}$.

6.4. Effects of growth phase on g

In this section, the effect of the growth phase on g and C_P is analysed. Fig. 6.5 shows a box plot g measured during all cirrus experiments of the RICE04 measurement campaign, for an experiment list with the used settings of PHIPS-POL in the individual experiments see appendix C.2.1. The figure is separated into particles measured during the initial growth periods ('i'), sublimation periods ('s'), and regrowth periods ('r') of the regrowth exper-

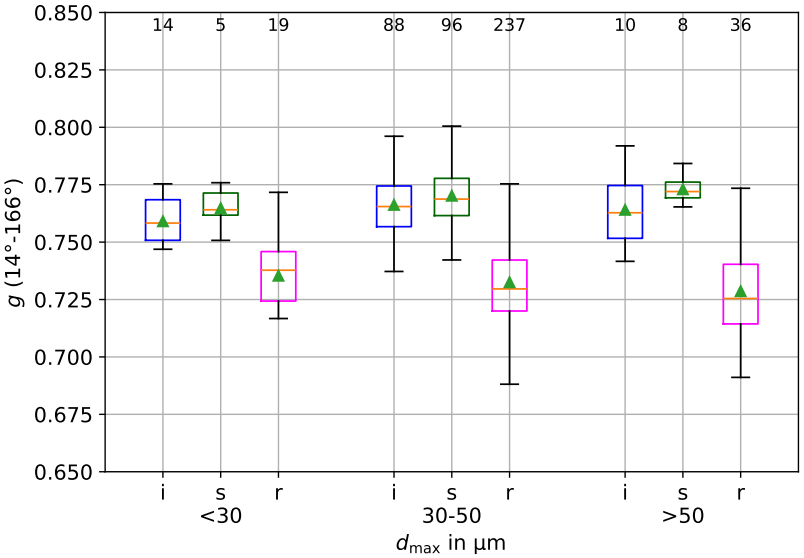

Figure 6.5.: Box plots of the asymmetry parameter (g) during the different phases of the regrowth experiments. The box plots show particles measured during the initial growth periods ('i'), during the sublimation periods ('s'), and during the regrowth periods ('r') of the regrowth experiments separately. The results are devided into three size groups to reduce the effect of the particle size. The number above the box plots give the number of sets of 50 angular scattering functions that are used for the box plots. In comparison to the initial growth phase, a slight increase in g during the sublimation phase and a strong decrease in g during the regrowth phase are observed.

iments. Furthermore, the particles are separated into three size groups of sizes <30 µm, 30 µm to 50 µm, and >50 µm to reduce a possible effect of the particle size on g. In all the size groups, there is an increase in g during the sublimation period, with a mean of 0.01 in comparison to the initial growth period. Furthermore, all size groups show a decrease g during the regrowth periods, with a mean of -0.03 in comparison to the initial growth period. Next, the growth conditions of individual experiments will be investigated.

In Fig. 6.6 a box plot is shown for C_P, also separated into growth phases and particle size groups. During the sublimation periods the C_P decreases in all size groups with a mean decrease of -0.01 in comparison to the initial growth period. C_P increases with reference to the initial growth period during the regrowth periods in all size groups, with a mean increase of 0.05.

The process causing the decrease in morphological complexity during sublimation is detailed in the following. In sub-saturated conditions with respect to ice, the high curvature parts of the ice crystal sublimate first because the larger surface area leads to a locally higher water vapour pressure, which increases sublimation [64]. The reduction in curvature during sublimation reduces the degree of morphological complexity, which explains the reduction in C_P during the sublimation periods of the experiments. A reduction in morphological complexity during ice crystal sublimation has also been reported in the literature [151, 135].

While an irreversible increase in ice crystal morphological complexity during multiple regrowth cycles is known [158], the general decrease in asymmetry parameter g after a sublimation-regrowth cycle is a new finding. It is supported by the known inverse relationship between the ice crystal morphological complexity and g [150, 173]. The finding implies that ageing cirrus clouds, which undergo sublimation and regrowth cycles, exhibit lower g in comparison to cirrus clouds in their initial growth state. A similar decrease in asymmetry parameter has been observed in situ in the atmosphere for ageing contrail cirrus clouds [36, 16]. Nevertheless, the results from cloud chamber observations can only be transferred to fast-growing cirrus clouds because it is not possible to simulate slow particle growth (exceeding time periods in the order of ten minutes) in the AIDA cloud simulation chamber due to sedimentation losses.

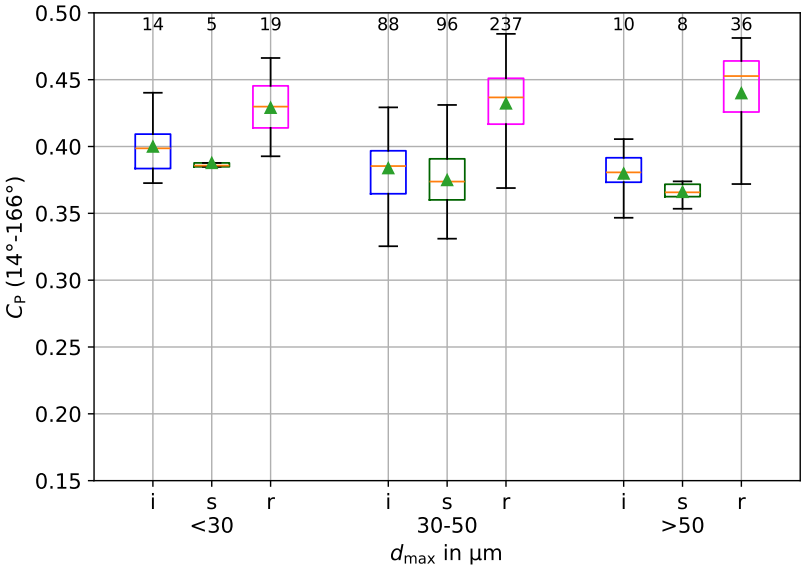

Figure 6.6.: Box plots of the complexity parameter (C_P) during the different phases of the regrowth experiments. The box plots show particles measured during the initial growth periods ('i'), during the sublimation periods ('s'), and during the regrowth periods ('r') of the regrowth experiments separately. The results are devided into three size groups to reduce the effect of the particle size. The number above the box plots give the number of sets of 50 angular scattering functions that are used for the box plots. In comparison to the initial growth phase, a slight decrease in C_P during the sublimation phase and a strong increase in C_P during the regrowth phase are observed.

6.5. Effects of relative humidity and temperature on g

In this section, the effects of T and RH_{ice} on g and C_P are analysed at quasi-constant conditions during the regrowth phases of the experiments.

In Fig. 6.7a,b the mean values of the g and C_P during the regrowth experiments are shown at different temperatures T_{gas} in the AIDA cloud simulation chamber. The sizes are restricted between 30 µm and 50 µm to reduce the effect of changing particle size on g and C_P. The standard deviation of T_{gas} during the regrowth phase is shown as an error bar. The error bars of g and

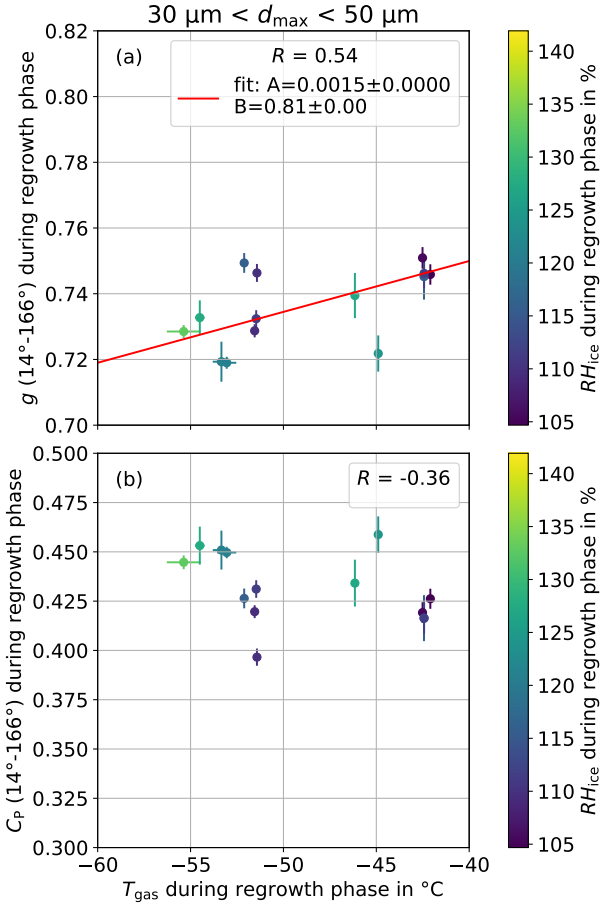

Figure 6.7.: Mean asymmetry parameter (g) **(a)** and mean complexity parameter (C_P) **(b)** during the regrowth phases of the expansion experiments at quasi-constant relative humidity with respect to ice (RH_{ice}) are shown as a function of the mean gas temperature (T_{gas}) in the AIDA cloud simulation chamber. Particle sizes are restricted to 30 µm to 50 µm to limit the size effect. There is a moderate correlation between g and T_{gas} and weak negative correlation between C_P and T_{gas}.

C_P are the PHIPS-POL measurement uncertainty derived with a Monte-Carlo simulation from the uncertainty of the channel-to-channel gain calibration

factors (see section 3.1.3f). The correlation is determined with the Pearson correlation coefficient R and a linear regression is added when at least a moderate correlation with $|R| > 0.5$ exists. There is moderate correlation between T_{gas} and g with R of 0.54 and a weak negative correlation between T_{gas} and C_{P} with R of -0.36.

The temperature influences the morphological complexity and thus g because it governs the growth rate as well as the ratio between the growth rates at the basal and prismatic facets as well as their ratio [6, 158]. Furthermore, the temperature affects the thickness of the quasi-liquid layer on the ice crystal, which again influences the particle growth [51, 103, 158]. Our findings are consistent with the temperature dependence of g observed in atmospheric mid-latitude cirrus [42].

Next, the effect of the relative humidity on g and C_{P} is investigated. Fig. 6.8a,b shows the mean values of the g and C_{P} during the regrowth experiments at different RH_{ice} in the AIDA cloud simulation chamber. The sizes are again restricted between 30 µm and 50 µm. The error bars of RH_{ice} are the standard deviation of the values measured during the regrowth phases. There is a moderate negative correlation between g and RH_{ice} with R of -0.55. A high correlation with R of 0.72 is found between C_{P} and RH_{ice}.

Particle growth at higher relative humidity has been reported in literature to cause morphologically more complex ice crystals [6, 135, 158]. Pristine particle growth occurs at low supersaturations because the slow growth speed enables the deposited molecules to well diffuse laterally, while fast growth speed promotes defects in the crystal lattice through two-dimensional nucleation of ice [112]. Two-dimensional nucleation of ice is a process where new layers in the ice lattice are formed through multiple isolated monolayer patches, which spread across the surface [33, 129]. Consequently, the morphological complexity increases at higher ice particle growth speeds. A possible process can also be stacking vaults from cubic growth [81, 158].

In the following, the dependence of g and C_{P} on the available condensible water vapour mixing ratio w^{acw} is analysed. $w^{\mathrm{acw}} = w - w_{\mathrm{s}}$ is the difference between the interstitial water vapour mixing ratio $w = \frac{p_{\mathrm{w}}}{p - p_{\mathrm{w}}}$ and the saturated water vapour mixing ratio $w^{\mathrm{s}} = \frac{p^{\mathrm{s}}_{\mathrm{w}}}{p - p^{\mathrm{s}}_{\mathrm{w}}}$ with water vapour pressure p_{w}, saturated water vapour pressure $p^{\mathrm{s}}_{\mathrm{w}}$, total air pressure p and the ratio between the molar masses of water and dry air $\epsilon = 0.622$. w^{acw} is a measure that combines the effects of temperature and relative humidity on the ice

crystal growth [135]. There is at most a weak correlation observed between g and w^{acw} ($R = -0.05$) and between C_{P} and w^{acw} ($R = 0.26$). It is a surprising finding that RH_{ice} and T individually have a stronger influence on g and C_{P} in comparison to the combined w^{acw}.

The findings of the relationship between w^{acw} and C_{P} differ from the relation between w^{acw} and the small-scale complexity parameter k_{e} found by [135], where a major effect of w^{acw} on k_{e} was observed. The difference in the relation between w_{acw} and k_{e} and between w_{acw} and C_{P} can be explained by the definition of k_{e}, which is a measure of the small-scale morphological complexity of individual particles, while C_{P} is a measure of the morphological complexity of an ensemble of ice particles. When the angular scattering function is averaged over 50 particles for the retrieval of C_{P}, speckle patterns caused by the small-scale complexity tend to average out, while they have an influence on k_{e}. This shows that there is no simple relationship between morphological complexity metrics C_{P} and k_{e}.

Consequently, C_{P} is likely more influenced by the shape component of the ice particle habit than by the small-scale complexity. This is consistent with the findings of [6] that the particle shape, namely habit and aspect ratio, is not dominated by w^{acw} but rather depends on T and RH_{ice} individually.

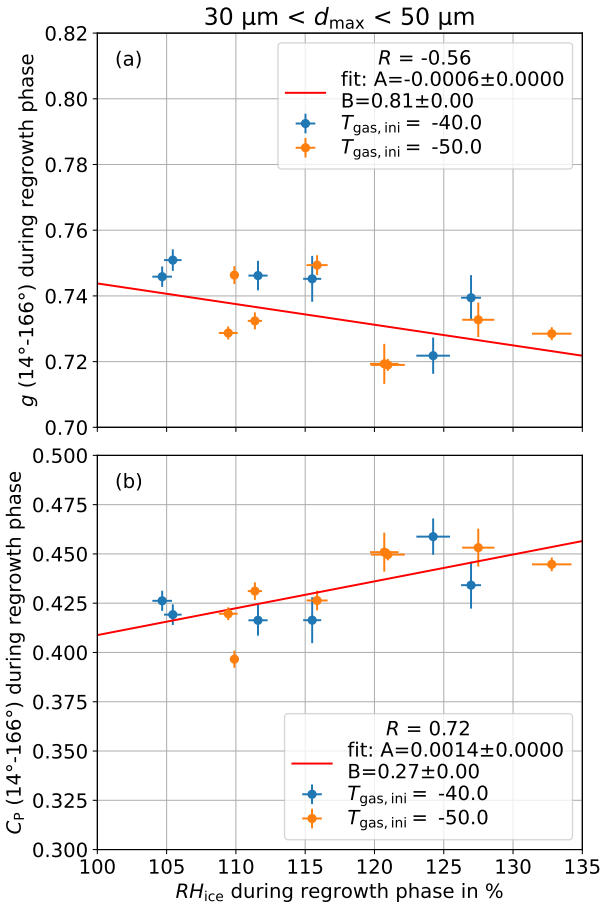

Figure 6.8.: Mean asymmetry parameter (g) **(a)** and mean complexity parameter (C_P) **(b)** during the regrowth phases of the expansion experiments at quasi-constant relative humidity are shown as function of the relative humidity with respect to ice (RH_{ice}) in the AIDA cloud simulation chamber. Initial gas temperatures of -40 °C and -50 °C are shown in different colour. Particle sizes are restricted to 30 µm to 50 µm to limit the size effect. The Pearson correlation coefficient R shows a moderate negative correlation between g and RH_{ice} and a high correlation between C_P and RH_{ice}.

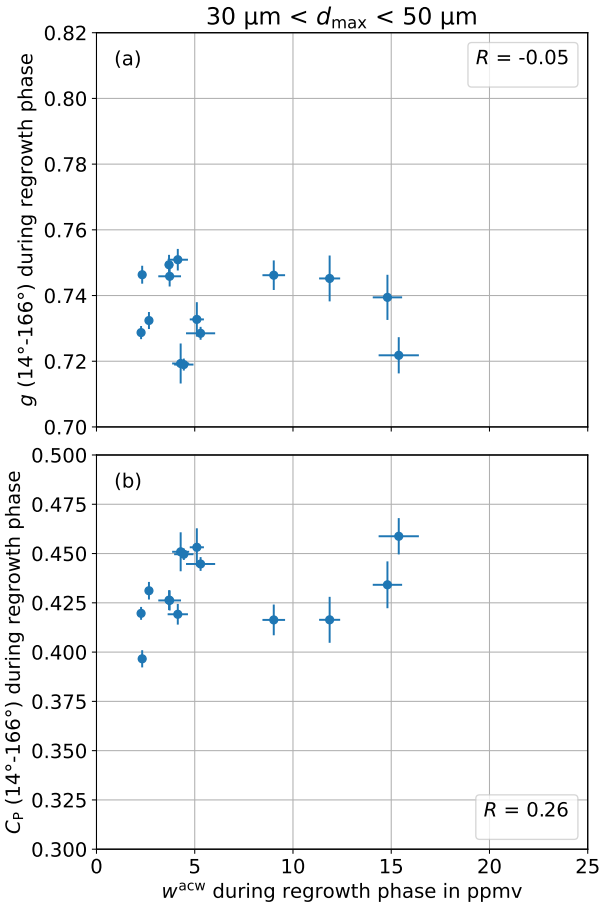

Figure 6.9.: Mean asymmetry parameter (g) **(a)** and mean complexity parameter (C_P) **(b)** during the regrowth phases of the expansion experiments at quasi-constant regrowth conditions are shown as function of the mean available condensible water vapour mixing ratio (w^{acw}) in the AIDA cloud simulation chamber. Particle sizes are restricted to 30 µm to 50 µm to limit the size effect. The Pearson correlation coefficient R shows at most a weak correlation between g and w^{acw} and between C_P and w^{acw}.

6.6. Size and temperature effect on g

In the previous sections, the effects of the macrophysical cloud parameters like temperature, relative humidity, and growth phase on g and C_P were investigated. In the following, we will continue with an analysis of the link between the microphysical properties identified on the images of the PHIPS-POL cameras and the optical parameters g and C_P.

Fig. 6.10a and Fig. 6.10b show the mean g and C_P, respectively, of all particles in the corresponding size and aspect ratio ranges. Size and aspect ratio groups with less than 50 particles are not shown due to poor statistics (white boxes). Fig. 6.10c,d,e,f show the individual effects of d_{max} and aspect ratios on g and C_P. Pearson correlation coefficients indicate a moderate correlation between the aspect ratio and g and C_P, along with a high correlation between d_{max} and C_P. However, the differences between g and C_P across the d_{max} and aspect ratio bins are minimal (<0.01).

In previous studies, a decreasing trend of g with particle size was seen in atmospheric observations with PHIPS [66, 160], while the opposite trend has previously been reported from measurements with the polar nephelometer [43]. A reason for the absence of clear trends in the cloud chamber measurements can be the limited image quality at small particle sizes. Especially for particle sizes below 50 µm, the images often cannot properly resolve the aspect ratio of the particle. A different explanation is the common habit class of (budding) bullet rosettes during the experiments. For bullet rosettes, the aspect ratio determined with the algorithm of [139] is generally close to one when similar arm length and well-distributed arms are assumed (see also images in Fig. 6.3). While the aspect ratio of the individual bullets (as used in [160]) is a promising measure, the smaller sizes of the cloud chamber-grown particles and the limited image resolution inhibit this analysis.

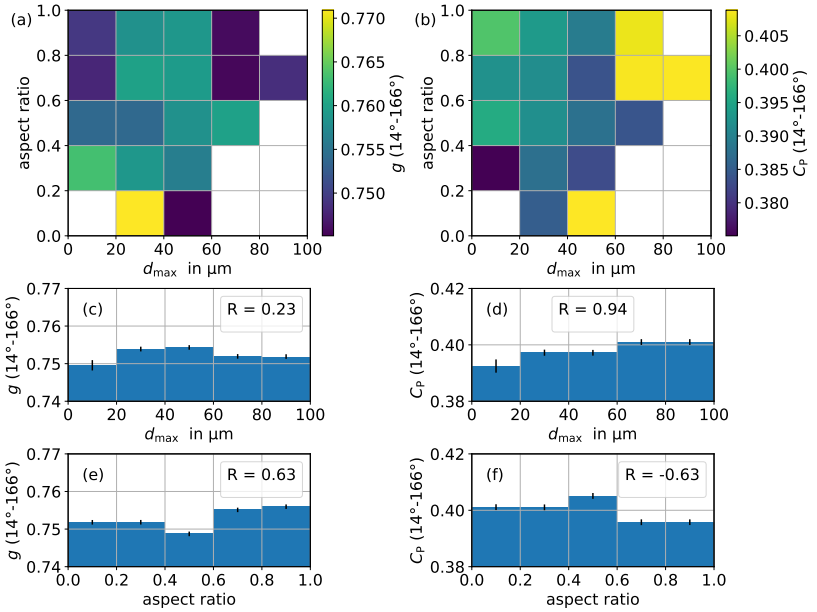

Figure 6.10.: Mean of asymmetry parameter (g) and complexity parameter (C_P) of individual ice particles of different maximum particle sizes and aspect ratios are shown in **(a)** and **(b)**, respectively. The influence of particle size on g and C_P for all aspect ratios are shown in **(c)** and **(d)**. The influence of the aspect ratio on g and C_P for all particle sizes are shown in **(e)** and **(f)**. Pearson correlation coefficients R are calculated. The data includes the complete experiments, not limited to the regrowth phases. Size and aspect ratio groups with less than 50 particles are not shown due to poor statistics (white boxes).

6.7. Effects of the growth conditions on the halo ratio

A special feature of PHIPS-POL is that it can, unlike PHIPS-HALO, measure the light scattering intensity at a polar angle of 22°. At 22° an intensity maximum occurs for light that is scattered by pristine hexagonal ice particles, causing the atmospheric phenomenon known as halo [25, p. 10.10.2]. A measure to quantify an increased intensity of light scattered at the polar angle of 22° is the halo ratio, which we define as the intensity detected at

a polar angle of 22° divided by the intensity detected at a polar angle of 14° ($I_{22°}/I_{14°}$), similar to the halo ratio definition by [5].

Fig. 6.11a, Fig. 6.11b, and Fig. 6.11c show violin plots of the halo ratio of individual particles as a function of RH_{ice}, the average temperature during regrowth ($\overline{T}$), and w^{acw}, respectively. In the violin plots, the 90 % quantile is shown in red. Only the regrowth phases of the experiments with quasi-constant regrowth conditions are included. While there is no clear effect of RH_{ice} or $\overline{T}$, the halo ratio shows a decrease in upper outliers and a decrease in the 90 % quantile with increasing w^{acw}. There is a high correlation with $R = -0.80$ between the 90 % quantile and w^{acw}.

Only the 90 % quantile has an increasing halo ratio at slow growth conditions because an exact azimuthal alignment is required for halo reflections to reach the PHIPS detector. The decreasing trend of the 90 % quantile of the halo ratio with w_{acw} emphasises the slow and pristine growth regime that is needed for halo producing ice particles. [135] defined a threshold value of w_{acw} of 4.3 ppmv for the growth of ice particles with a sufficient degree of crystal morphological complexity to exhibit a flat angular scattering function. While Fig. 6.11c shows a generally higher 90 % quantile below this threshold of w_{acw}, it also shows that the 90 % quantile rather decreases gradually with increasing w_{acw} than an abrupt change in growth regime.

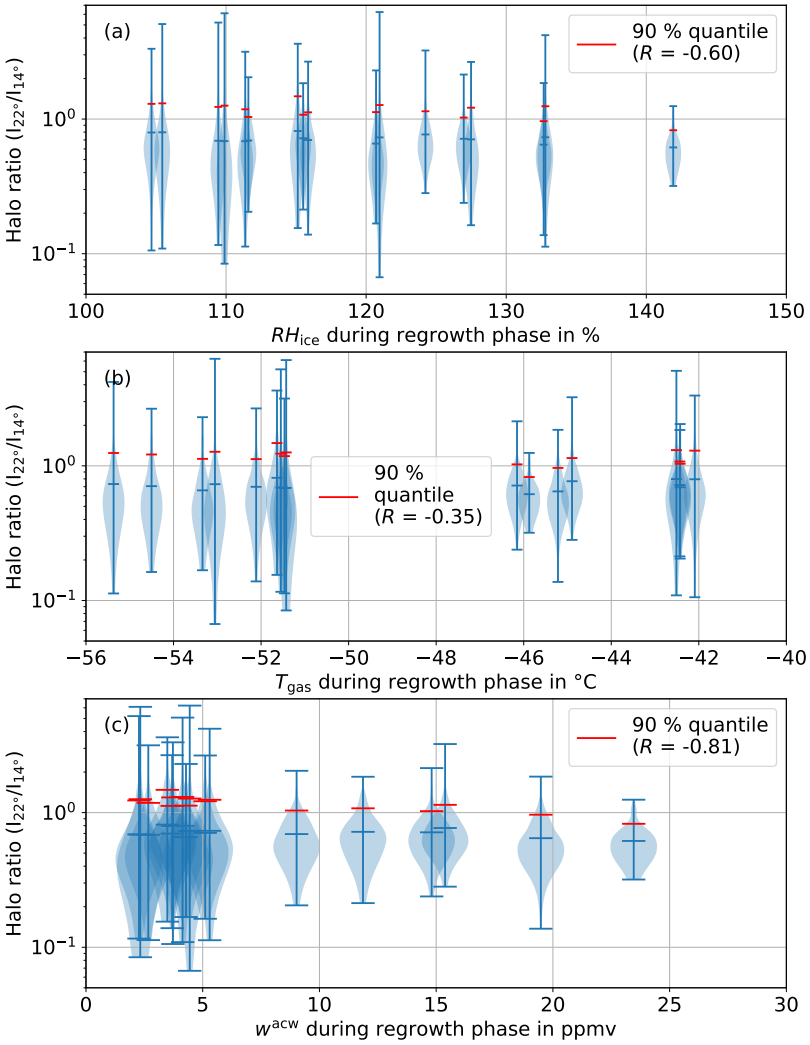

Figure 6.11.: Halo ratio as a function of regrowth relative humidity with respect to ice (RH_{ice}) (**a**), as a function of regrowth gas temperature (T_{gas}) (**b**), and as a function of regrowth available condensible water vapour mixing ratio w^{acw} (**c**). R is the Pearson correlation coefficient. There is a high correlation between the 90 % quantile of the halo ratio and w^{acw}.

6.8. Atmospheric implications

The atmospheric implications of the findings of this work are highlighted in this section. In situ measurements of the asymmetry parameter g of cirrus clouds are relatively scarce. Observations range between 0.74 and 0.75 with the cloud integrating nephelometer [48, 40, 41], between 0.76 and 0.79 with the polar nephelometer [74, 43, 140, 105, 16], and between 0.72 and 0.75 with PHIPS-HALO [135, 68, 160, 66] (see table 6.2). g of cirrus clouds can also be retrieved from remote sensing radiometric satellite observations, which yielded values between 0.76 and 0.78 [27, 28, 29]. However, for the remote sensing retrieval, an underlying optical particle model and therefore assumptions on the ice crystal morphology are needed.

While most atmospheric measurements of g range between 0.74 and 0.79, modelling results return values between approximately 0.75 and 0.85 [93, 101]. Assumptions of a lower degree of ice crystal morphological complexity tend to return higher values of g [99].

We found a mean g of 0.74 during the complete experiments and of 0.72 during the regrowth phases, which is lower than previous cloud chamber observations with PHIPS-HALO and lower than atmospheric measurements with the polar nephelometer. Yet, they are in good agreement with atmospheric observations of the cloud integrating nephelometer and PHIPS-HALO. A possible reason for the lower value in comparison to the previous cloud chamber measurements with PHIPS-HALO is the improved retrieval method, which does not rely on an optical particle model. The discrepancy to the remote sensing measurement can be explained by the bias of remote sensing instrumentation to weight g of the first optical depth of the cloud higher, which is usually near the cloud top at more pristine growth conditions and consequently yields higher g [28].

In this work, moderate correlations between g and RH_{ice} and between g and T are found. This is in contrast to the hypothesis by [135] that the angular scattering function becomes insensitive to a further increase in available condensible water vapour at $w_{\mathrm{acw}} > 4.3\,\mathrm{ppmv}$. While we did not find a significant effect of w_{acw} on g, there are individual influences of RH_{ice} and g. This is supported by the particle growth regime study by [6], where T and RH_{ice} have individual influences on the growth regime, and thus also on the optical properties, even for $w_{\mathrm{acw}} > 4.3\,\mathrm{ppmv}$.

While the slopes of the linear regression between g and T and between g and C_P may seem low with changes of g of approximately 0.03 over the measurement ranges of T and RH_{ice}, it needs to be considered that radiative transfer models are sensitive to small changes of g. In order to limit the uncertainty of the radiative fluxes below ice clouds with an uncertainty of 5 %, g needs to be known with an uncertainty of 5 % [157]. Limitations and assumptions of the used retrieval method of [173] are detailed in the next section.

Cloud type	Instrument	g	References
Arctic cirrus	Cloud integrating nephelometer	0.74±0.03	[48, 40]
Florida cirrus	Cloud integrating nephelometer	0.75±0.01	[41]
ML cirrus	Cloud integrating nephelometer	0.77 [0.74,0.79]	[5]
ML cirrus	Polar nephelometer	0.77 [0.76,0.78]	[45, 43, 42]
ML cirrus	Polar nephelometer	0.79 [0.77,0.80]	[74, 44]
Polluted cirrus	Polar nephelometer	0.77 [0.76,0.79]	[16]
Aged contrail cirrus	Polar nephelometer	0.78 [0.76,0.80]	[36, 16]
Cloud chamber grown cirrus	PHIPS-HALO	0.78	[135]
ML Cirrus	PHIPS-HALO	0.75	[68]
HL Cirrus (only bullet rosette habit)	PHIPS-HALO	0.72 [0.70,0.75]	[160]
ML and HL cirrus	PHIPS-HALO	0.73 [0.69,0.76]	[66]

Table 6.2.: Asymmetry parameter (g) from different airborne campaigns with different instruments. PHIPS-HALO is operated at 532 nm, the polar nephelometer is operated at approximately 800 nm, and the cloud integrating nephelometer is operated at 635 nm. ML refers to mid-latitude and HL refers to high latitude.

6.9. Limitations of the nephelometer measurements

The accuracy of the retrieval of g with the method of [173] depends on the values of C_P. The relation is shown in Fig. 6.12, where the retrieved g and C_P are shown as a function of the true values of g and C_P. The figures are based on a set of angular scattering functions of different hexagonal and Koch fractal-shaped ice particles of different sizes, shapes, and distortions, which were modeled with the ray tracing code of [99]. Fig. 6.12a uses the angular detector setup of PHIPS-HALO, Fig. 6.12b of PHIPS-POL for the angular scattering function from 14° to 166°, and Fig. 6.12c of PHIPS-POL for the angular scattering function from 6° to 166°. The ranges of C_P for regions of highly accurate retrieval with absolute errors below 0.005 (**A**) and convergence with absolute errors below 0.02 (**B**) are given in a table in Fig. 6.12d. It can be noted that the retrieval accuracy increases for decreasing smallest detection angle.

During the experiments of RICE04 g is calculated using the detectors of PHIPS-POL between 6° to 166° and between 14° to 166° due to a large possible bias at the 6° detector. Using the angular scattering function between 6° to 166°, the C_P measured during RICE04 is higher than 0.25. According to the retrieval accuracy in Fig. 6.12c the retrieved data is the highly accurate region. C_P of the angular scattering function between 14° to 166° is higher than 0.35, which is also within the highly accurate region according to the retrieval accuracy in Fig. 6.12b. The mean values of g of both retrieval methods only differ by 0.01. The good agreement of g between the angular scattering functions with and without the 6° channel supports the reliability of the retrieval method.

The restriction of [108] used in the method of [173] of $\theta = 7/x$ (in radian) with size parameter x implies that the minimum particle size is 20.0 µm when using the angular scattering function between 6° and 166°. This condition is fulfilled for 94.3 % of the particles measured during RICE04.

The reliability of the used retrieval method of [173] has been questioned because it relies on the geometrical optics approximation. However, since 98.2 % of the particles measured during RICE04 are larger than a size parameter of 50 at the incident wavelength of 532 nm, the approximation is valid. A limitation of the method is that the diffraction component of g (g_D) uses the assumption of spherical particles, which is not true for ice particles. The

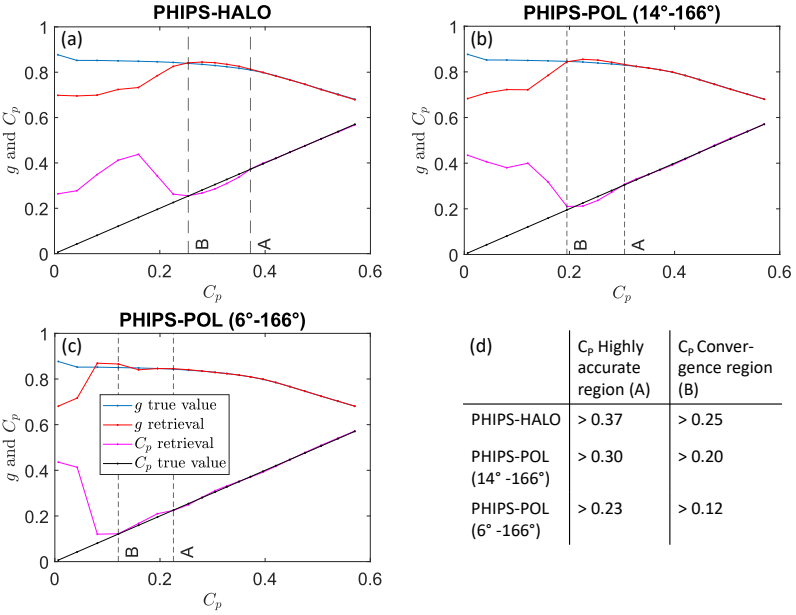

(d)	C_P Highly accurate region (A)	C_P Convergence region (B)
PHIPS-HALO	> 0.37	> 0.25
PHIPS-POL (14° -166°)	> 0.30	> 0.20
PHIPS-POL (6° -166°)	> 0.23	> 0.12

Figure 6.12.: The retrieved asymmetry parameter (g) and complexity parameter (C_P) are shown as a function of the real g and C_P for the detector layout in the nephelometer measurement of PHIPS-HALO **(a)**, of PHIPS-POL for the angular scattering function from 14° to 166° **(b)**, and of PHIPS-POL for the angular scattering function from 6° to 166° **(c)** using a mixture of hexagonal and Koch fractal shaped ray tracing simulated angular scattering functions [99]. The highly accurate regions of C_P with absolute retrieval errors below 0.005 and converging regions of C_P with absolute retrieval errors below 0.02 are marked as **A** and **B**, respectively. The figure is based on [173].

non-sphericity can affect the retrieval accuracy. Yet, g_D becomes close to unity as larger the particles become. Therefore, this effect likely only plays a role for the smallest detected particles, which make up a small fraction of the complete set of measured ice particles.

6.10. Summary and outlook

The mean asymmetry parameter g of cirrus cloud particles regrown at quasi-constant growth conditions in the AIDA cloud simulation chamber is found to

be 0.03 lower than during the initial ice particle growth. Simultaneously, the mean complexity parameter C_P is 0.05 higher during the regrowth phases in comparison to the initial growth phases. This implies that the ageing of cirrus alters their radiative properties through increasing morphological complexity during growth and sublimation cycles.

Performing experiments on the effects of quasi-constant growth conditions on g, a moderate positive correlation (R = 0.54) between T and g was found. Furthermore, a moderate negative correlation between the RH_{ice} and g (R = -0.56) was observed. Yet, only a weak correlation was found between w^{acw} and g, which can be attributed to the predominant individual influences of the T and RH_{ice}. This emphasises how the growth conditions of cirrus clouds influence their radiative properties through different ice particle morphologies, including the degree of morphological complexity.

Grouping the individual ice particles by size and aspect ratio, no clear trend of g with the maximum particle size or aspect ratio is observed. Possible reasons can be the used aspect ratio metric and the limited image quality for small particle sizes below 50 µm.

The halo ratio $I_{22°}/I_{14°}$ of individual ice particles was investigated as a function of growth conditions during the regrowth phases of the experiments. While there is no clear trend with the mean halo ratio, the growth conditions affect the 90 % quantile of the halo ratio. The 90% quantile is influenced due to the required specific ice crystal orientation for observing a halo maximum on the detector ring of PHIPS-POL. There is a moderate negative correlation of -0.61 between RH_{ice} and the 90 % quantile and a high negative correlation of -0.81 between w_{acw} and the 90 % quantile. This finding highlights the needed slow, pristine growth conditions for a growth regime of halo-producing ice crystals.

From the technical perspective, the setup of PHIPS-POL with two MCPMTs and the improved angular layout allowed an increased retrieval accuracy of g in comparison to PHIPS-HALO. Furthermore, additional information on the optical properties could be obtained with the halo ratio. For future improvement, adaptations to the beam shaping are needed so that the 6° detection position is less impaired. In addition, measurements of the polarisation properties with the second detector ring should be investigated further.

The next step is to investigate the observed values and dependencies of g in a radiative transfer model (e.g. ecRAD) [62]. This can be implemented, for

example, as a parametrisation of the microphysical properties of boundary layer ice particles, which were observed in chapter 5.

7. Conclusion

The last chapter concludes this work by summarizing the findings related to the three research questions about the microphysical and optical properties of small ice particles, which were introduced in chapter 1. Finally, an outlook outlines future research questions that emerge from this work.

7.1. Summary

Research Question 1: What are the microphysical properties of summer time small boundary layer ice particles at Dome C, and how do they differ in comparison to small boundary layer ice particles in polluted urban regions?

Multi-week in situ field measurements of the microphysical properties of boundary layer ice particles with sizes between 11 µm and 150 µm were conducted at Dome C on the Antarctic plateau. A particle size mode at approximately 70 µm was identified for cirrus precipitation and diamond dust events, which did not exist during periods of ice fog. Rather, ice fog was dominated by a smaller size mode below 11 µm. The mean particle concentration observed during ice fog events was, with $3.8\,L^{-1}$, approximately four times higher than the mean particle concentration of $1.0\,L^{-1}$ observed during cirrus precipitation and diamond dust events. Signs of homogeneous nucleation were observed as a possible pathway for the initiation of ice fog on the Antarctic plateau.

The mean ice fog particle concentrations measured in the clean environment at Dome C are lower than the mean particle concentrations of urban, polluted ice fog in Fairbanks, Alaska, ($7.7\,L^{-1}$), measured with the same instrument. Furthermore, ice fog particles at Dome C were found to be morphologically

more pristine than their counterparts in Fairbanks urban ice fog. The differences in microphysical properties are likely caused by high anthropogenic aerosol and water vapour emissions at Fairbanks, Alaska.

Research Question 2: How is the backscattering linear depolarisation ratio linked to small ice particle microphysical properties like size, shape, and morphological complexity and how can this be accurately modelled with state-of-the-art light scattering simulations?

The combined analysis of 47 expansion experiments at cirrus temperatures conducted at the AIDA cloud simulation chamber showed that the particle size is the dominant driver for the linear depolarisation ratio (δ) of ice crystals with sizes between approximately 7 µm and 70 µm. Two temperature dependent δ-size modes were found. At temperatures below -45 °C, δ predominantly stayed constant with increasing particle size. At temperatures between -45 °C and -39 °C, δ increased with increasing particle size. Overall, ice particles with sizes larger than 10 µm were found to have $\delta < 0.3$, which is smaller than atmospheric observations but in good agreement with polar observations.

No clear correlation was observed between the small-scale complexity parameter (k_e) and δ. A possible reason can be that the ice crystals grown in the cloud chamber inherently have a baseline roughness that prevents an observable correlation between k_e and δ. It is also possible that non-constant microphysical properties affected δ, which do not affect k_e. This can be, for instance, the particle aspect ratio.

The measurement data could be reproduced with ray tracing simulations only when different types of ice particle morphological complexity were incorporated in the simulations. This included the tilted facet method, hollow basal facets, and internal scatterers. Yet, the measurement results could not be reproduced with the state-of-the-art numerically exact IITM method, likely due to using exclusively surface roughness as morphological complexity in the particle model. This shows that morphological complexity needs to be properly included for accurate radiative transfer models as well as in accurate remote sensing retrievals.

Research question 3: How do the growth conditions, such as temperature and relative humidity, influence the asymmetry parameter of cirrus clouds composed of small ice particles?

Cirrus cloud regrowth experiments conducted at the AIDA cloud simulation chamber showed that the asymmetry parameter g of ice particles with sizes

predominantly below 70 µm decreased by 0.03 during the regrowth phase (following an initial growth period and sublimation). This indicates that the ageing of cirrus clouds modifies their radiative properties through recurrent growth and sublimation phases.

Furthermore, during particle regrowth at quasi-constant growth conditions, a moderate negative correlation between g and the relative humidity with respect to ice ($R = -0.56$) and a weak negative correlation between g and the temperature ($R = -0.36$) were found. This highlights that the growth conditions of cirrus clouds influence their radiative properties by affecting the ice particle microphysical properties, including morphological complexity.

In addition, a strong negative correlation ($R = -0.81$) was found between the halo ratio and the available condensible water vapour mixing ratio. This highlights the pristine, slow growth conditions needed for halo-producing ice particle growth.

Overall, it can be concluded that **ice particle size and morphological complexity need to be considered together to fully characterise and to correctly simulate small ice particles**.

7.2. Outlook

The results of this work raise follow-up research questions to be studied in the future. The characterisation of the microphysical properties of small ice particles at Dome C motivates investigations of the effect of the retrieved ice particle microphysical properties on Antarctic weather and climate models. To achieve this objective, it would be useful to measure the microphysical properties of boundary layer ice particles at Dome C over a longer time frame including wintertime measurements to obtain statistically more robust information. Furthermore, simultaneous INP measurements could provide additional insights on the nucleation processes.

The analysis of the linear depolarisation ratio of small ice particles at the AIDA cloud simulation chamber encourages further studies on the link between the linear depolarisation ratio and the ice particle morphological complexity. It remains an open question if there is a link between the linear depolarisation ratio and the ice particle morphological complexity when using a different morphological complexity metric (e.g. C_{P} measured with PHIPS) or when

investigating single particles. Furthermore, the discrepancy between the measurement data of δ and the numerically exact simulations motivates follow-up studies on the representation of ice particle morphological complexity in numerically exact optical simulations with the aim to reproduce the observed linear depolarisation ratio-size relation.

The found effect of the growth conditions on the asymmetry parameter of small cloud chamber-grown ice particles can be adapted in cirrus radiative transfer calculations to accurately represent small ice particles. Furthermore, the exact link between the asymmetry parameter and the growth conditions of ice particles larger than 70 µm remains an open question due to the present limitation to grow ice particles with sizes exceeding approximately 70 µm in the AIDA cloud simulation chamber.

While the results of this work do not directly mitigate global warming, this work contributes by adding to the understanding of our atmosphere and enabling improvements of the microphysical and optical parametrisations of cirrus clouds in climate models.

A. Appendix of chapter about boundary lacer ice particles at Dome C, Antarctica

This appendix chapter provides additional information about the measurements at Dome C and about the PPD-2K instrument.

A.1. PPD-2K operational time during measurement campaign at Dome C, Antarctica

The operational times of PPD-2K during the deployment at Dome C, Antarctica, between November 2023 and January 2024 are shown in Fig. A.1 as red periods. Non-operational downtimes due to servicing, maintenance, and instrument connection errors occurred during the white periods.

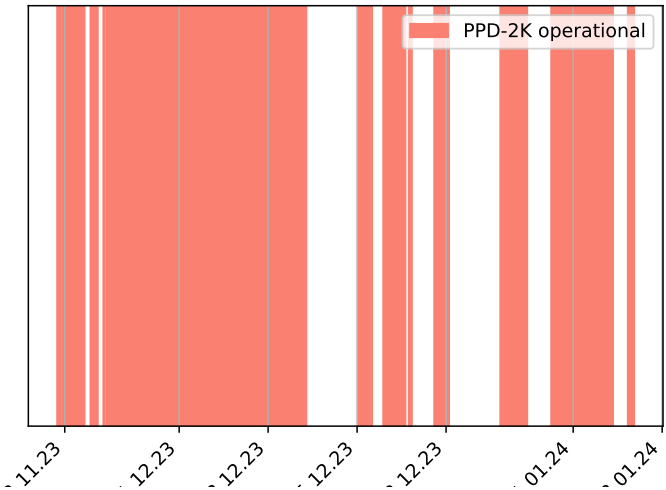

Figure A.1.: Red periods: Operational time of the PPD-2K during deployment at Dome C, Antarctica, between November 2023 and January 2024. White periods: Non-operational periods due to servicing, maintenance, and instrument connection errors.

A.2. Conversion between spherical equivalent diameter and ice particle maximum dimension

The ice particle shape and morphological complexity determine the light scattering properties and therefore how much light is scattered in the direction of the trigger field of view. As a result, the relationship between the particle maximum dimension and the spherical equivalent diameter measured with PPD-2K depends on the ice particle shape and morphological complexity. The conversion between the spherical equivalent diameter and the maximum dimension can be estimated by calculating how much light is scattered in the direction of the trigger field of view of PPD-2K. Using a ray tracing light scattering database of ice crystals by [180] and Mie calculations for spherical droplets [117], a spherical equivalent diameter of 25 µm is estimated to be equivalent to a maximum dimension of between 30 µm for a rough hollow column and up to 69 µm for a smooth plate. The relationship is shown in Fig. A.2 for solid columns, hollow columns, hollow bullet rosettes, and solid

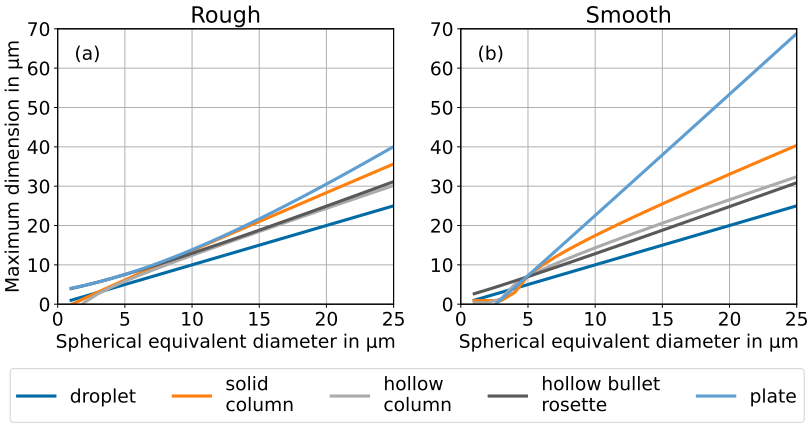

Figure A.2.: Ice particle maximum dimension as a function of spherical equivalent diameters for rough **(a)** and smooth **(b)** ice particles of different habits. The conversion is calculated from the light that is scattering in the direction of the trigger field of view based on an ice crystals light scattering database [180] and Mie theory for droplets [117]. The maximum size is up to 2.5 times larger than the spherical equivalent diameter.

plates. Smooth particles of different particle habits show a larger spread in the conversion between the maximum dimension and the spherical equivalent diameter than rough particles. This can be attributed to the fact that the scattering features, like the 22° halo, tend to disappear for rough particles, causing the angular scattering function to have a flat, featureless shape which depends less on the different habits.

A.3. Optical small-scale parameter (k_e) threshold for rough particles

For diffraction patterns recorded with SID-3, a small-scale complexity parameter threshold for rough ice particles was determined to $k_e = 4.6$ [135]. For rough ice particles, speckles are increasingly visible on the diffraction patterns. Random examples of diffraction patterns of Dome C ice particles with a Fourier maximum of two are shown in Fig. A.3. It can be seen that also for PPD-2K speckle patterns start to be visible for k_e of approximately 4.6

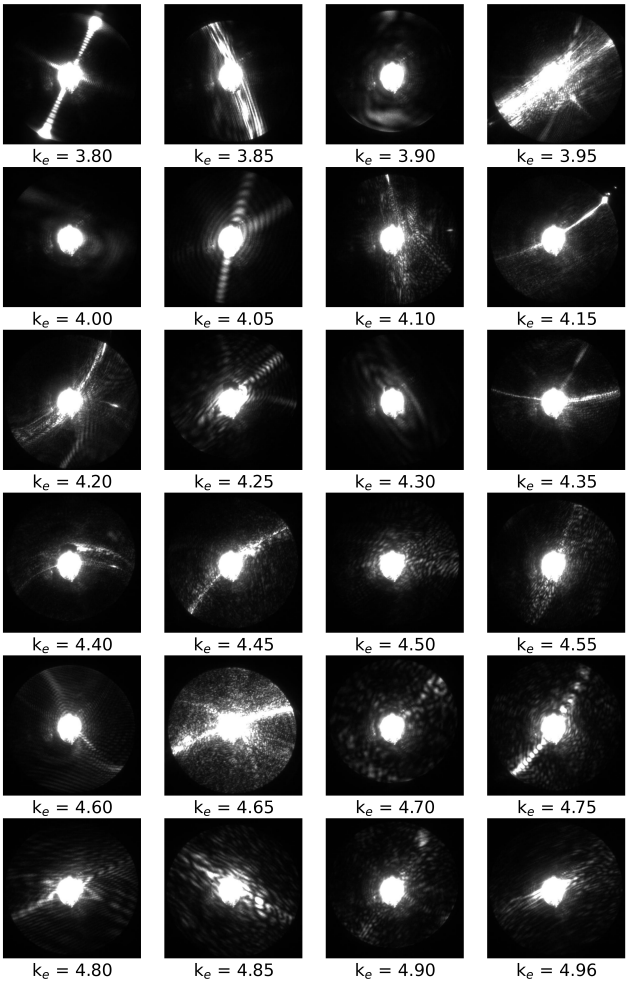

Figure A.3.: Random example diffraction patterns of columns classified by a Fourier maximum of second order. They are sorted by the small-scale complexity parameter k_e. Ice particles are considered complex when k_e is equal to 4.6 or higher.

and higher, similar to SID-3. Therefore, the threshold of rough ice particles of $k_e = 4.6$ is valid for PPD-2K too.

A.4. Dome C liquid fog event of 18 December 2023

On 17 and 18 November 2023, two locally formed low vertical extent liquid fog events were observed at Dome C. Fig. A.4 shows the temporal evolution of the microphysical properties of the liquid fog event of 18 December 2023, together with the atmospheric conditions. Also for this event, a period of homogeneous freezing is observed, when the fraction of frozen ice particles increases from less than 5 % to over 50 % between 16:00 and 17:00 UTC at a temperature of approximately -38 °C near ground level. Wind speed, wind direction, and the particle shape fractions according to the Fourier diffraction pattern analysis are shown in Fig. A.5. Pollution from the station's exhausts is possible when wind speed and direction are in range 1 (light blue shaded) or when wind speed or direction are in range 2 (dark blue shaded) [155]. Therefore, Concordia station's generators did not influence the measurements.

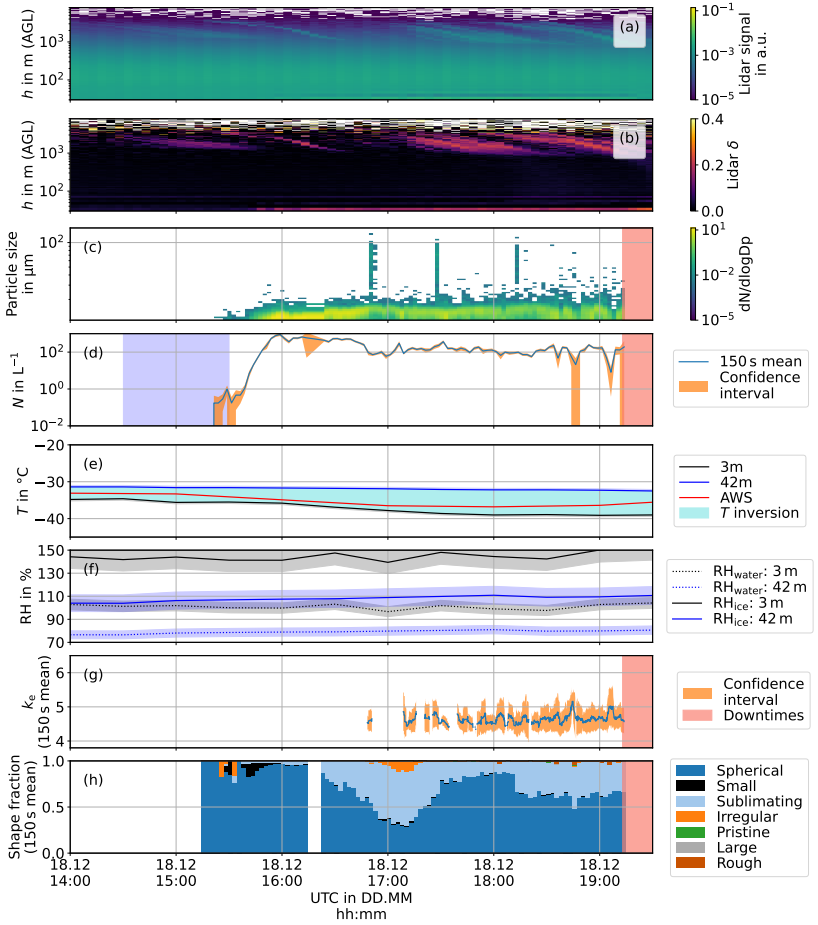

Figure A.4.: Dome C supercooled liquid fog event of 18 December 2023 with temporal evolution of the LIDAR backscattering signal **(a)**, LIDAR linear depolarisation ratio (δ) **(b)**, PPD-2K particle size distribution **(c)** and PPD-2K particle concentration (N) integrated over 150 s between 11 µm and 150 µm **(d)**. PPD-2K downtimes are highlighted in red. The temperature (T) and relative humidity (RH) with respect to liquid water and ice at Concordia station at altitudes between 3 m (AGL) and 42 m (AGL) are shown in **(e)** and **(f)**. The temperature data from the AWS at Concordia station at 3 m (AGL) is added for redundancy. Temperature inversions are shaded in blue. CNN classified particle shape fractions [132] and mean optical small-scale complexity parameter (k_e) [156] derived from the PPD-2K diffraction patterns are shown in **(g)** and **(h)** for time periods of 150 s.

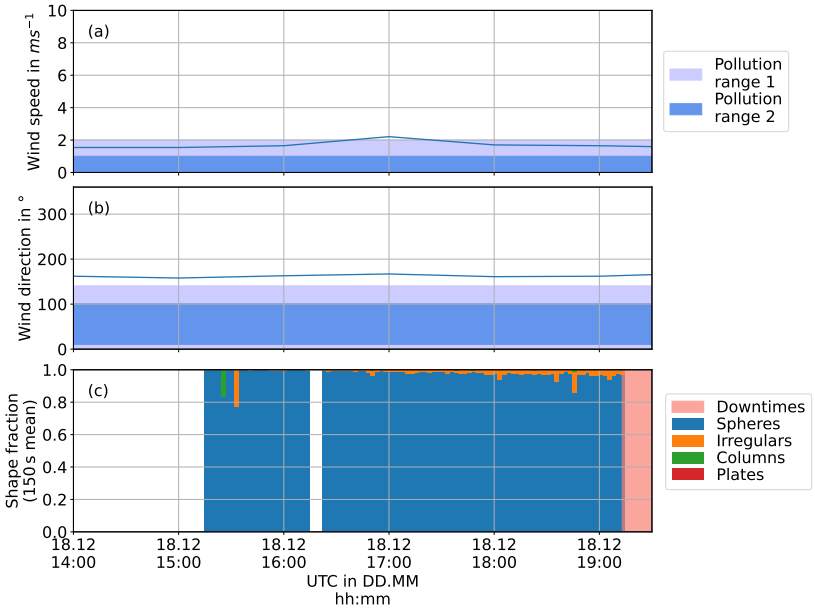

Figure A.5.: Wind speed **(a)** and wind direction **(b)** from the AWS at Concordia station [53]. Pollution from the station's exhausts is possible when wind speed and direction are in range 1 (light blue shaded) or when wind speed or direction are in range 2 (dark blue shaded) [155]. Pollution from the station does not affect the measurements of the ice fog event starting on 25 November 2023. **(c)** shows the particle shape fractions from the Fourier PPD-2K diffraction pattern analysis [156].

B. Appendix of chapter about depolarisation properties of small cirrus ice crystals

B.1. Additional ray tracing simulations

This section shows additional ray tracing simulations using the conventional geometrical optics ray tracing Monte Carlo code of [97]. Fig. B.1 shows the effect of a variation in aspect ratio between 1.5 and 2.0 on the linear depolarisation ratio for solid columns with mean free paths of 150 µm and 10000 µm and hollow columns with a mean free path of 2000 µm. A distortion of 0.3 is used. A variation in aspect ratio between 1.5 and 2.0 only causes minor differences in the simulated linear depolarisation ratio. The difference in linear depolarisation ratio is largest with 2.5 % between an aspect ratio of 1.5 and 2.0 for the smallest calculated size of 12.5 µm of the hollow columns.

The difference between the wavelength of 552 nm used in SIMONE-Junior during the RICE03 campaign and 448 nm used in SIMONE during the other investigated measurement campaigns is simulated with the Monte Carlo ray tracing simulations and shown in Fig. B.2. Linear depolarisation ratios for hollow columns with a mean free path of 2000 µm and solid columns with mean free paths of 150 µm and 10000 µm are calculated. A distortion of 0.3 and an aspect ratio of 1.5 are used. The wavelength of 552 nm used during RICE03 only causes minor changes to the linear depolarisation in comparison to the wavelength of 448 nm used during all other campaigns. The maximum difference in linear depolarisation ratio between the two wavelengths in the ray tracing simulations is 1.5 %.

Fig. B.3 shows the simulated linear depolarisation ratio for different depths of hollowness on the basal faces. The hollowness has the shape shown in Fig.

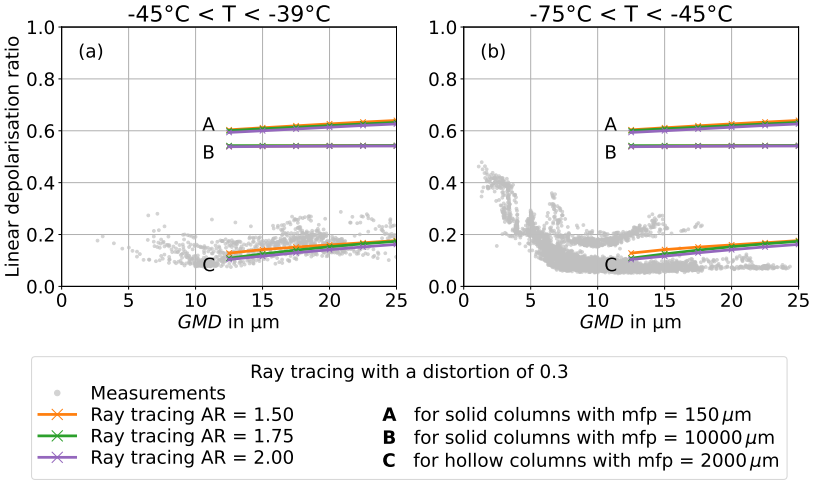

Figure B.1.: The effects of changing aspect ratios between 1.5 and 2.0 for the ray tracing simulations of the linear depolarisation ratio at the near-backscattering direction of 178° are shown for columns using [97]. The distortion is fixed to 0.3. Hollow columns with a mean free path of 2000 µm (**C**) and solid columns with a mean free path of 150 µm (**A**) and 10000 µm (**B**) are simulated. For comparison the AIDA measurement data of all temperatures between -45 °C and -39 °C (**a**) and between -75 °C and -45 °C (**b**) are added. The variation in aspect ratio between 1.5 and 2.0 only causes minor differences in the simulated linear depolarisation ratio.

5.8c. The depth on each side is varied between 0.0 and 0.5 of the crystal length from each basal face. An aspect ratio of 1.5, a distortion of 0.3, and a mean free path of 2000 µm are used. From no hollowness to a short hollowness of 0.1 of the crystal length, the linear depolarisation ratio increases by approximately 5 % - 10 %. For a further increase in hollowness depth to 0.333 and 0.5, the linear depolarisation ratio strongly decreases to values in the range of the SIMONE measurements at the AIDA cloud simulation chamber between 10 % and 20 %.

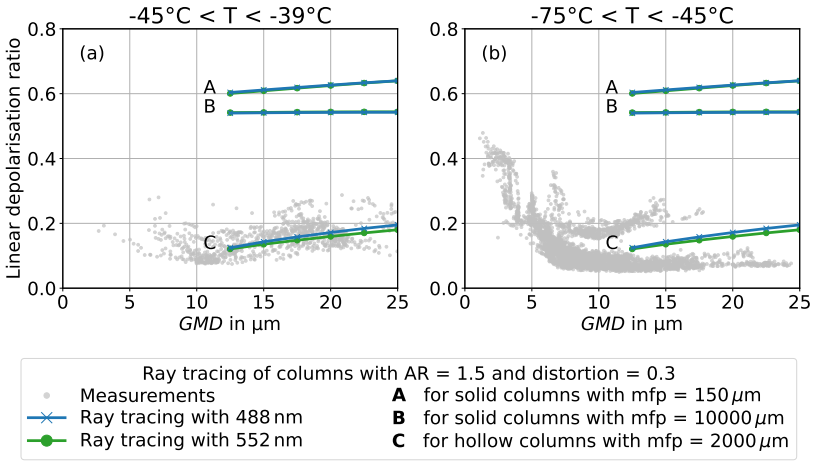

Figure B.2.: The differences using a wavelength of 448 nm (used in SIMONE) and 552 nm (used in SIMONE-Junior) for the ray tracing simulations of the linear depolarisation ratio at the near-backscattering direction of 178° are shown for columns using [97]. The aspect ratio is fixed to 1.5 and a distortion of 0.3 is used. Hollow columns with a mean free path of 2000 µm (**c**) and solid columns with a mean free path of 150 µm (**a**) and 10000 µm (**B**) are simulated. For comparison, the AIDA measurement data of all temperatures between -45 °C and -39 °C (**a**) and between -75 °C and -45 °C (**b**) are added. The different wavelengths that are used in the SIMONE and SIMONE-Junior instruments only cause minor differences in the simulated linear depolarisation ratio.

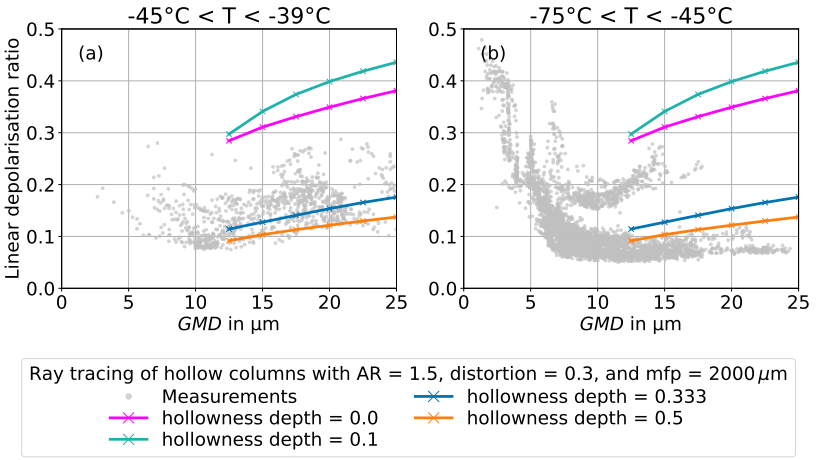

Figure B.3.: The effects of changing hollowness depth for hollow basal faces in the ray tracing simulations of the linear depolarisation ratio at the near-backscattering direction of 178° are shown for columns using [97]. The distortion is fixed to 0.3 and the aspect ratio to 1.5. Hollow columns with a hollowness depth from each basal face between 0.0 and 0.5 with mean free path of 2000 µm are simulated. For comparison the AIDA measurement data of all temperatures between -45 °C and -39 °C (**a**) and between -75 °C and -45 °C (**b**) are added. The linear depolarisation first increases for a hollowness depth of 0.5 and then decreases for further increasing hollowness depth up to 0.5.

C. Appendix of chapter about effect of ice particle growth conditions on asymmetry parameter

C.1. PHIPS-POL

C.1.1. PHIPS-POL crosstalk characterisation

For the PHIPS instruments, it is important to characterise the crosstalk from one channel of the MCPMT to the neighbouring channels. For the characterisation, laser pulses were generated with a homogeneous scattering element in the sensing area of the instrument. The scattering element was illuminated with digitally modulated laser pulses that were generated from a fiber-coupled OBIS laser and a function generator with a repetition rate of 40 Hz. One channel after the other was connected to the same angular position with all other channels but the trigger blinded. For each channel, > 1000 light pulses were recorded.

The next neighbours had a crosstalk of mainly below 3 %, which is in agreement with the manufacturer's specifications. Exemplarily, the crosstalk of channel 22 with gain 90 on both MCPMTs is shown in Fig. C.1. The black line stands for the manufacturer's specifications of a crosstalk < 3 %.

C.1.2. PHIPS-POL photomultiplier gain correction

In PHIPS-POL, the amplification of the two MCPMTs can be separately adjusted with a voltage. This voltage is provided from the backplane board and can be adjusted with a number between 0 and 256, called gain, for MCPMT1 (channel name: Offboardpot1) and MCPMT2 (channel name: Trigger gain).

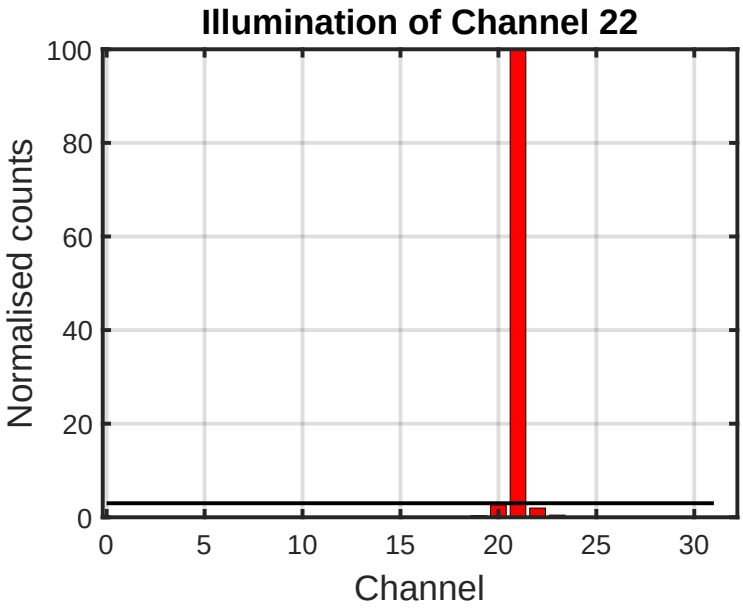

Figure C.1.: Example crosstalk of channel 22 from channel-to-channel crosstalk analysis with gain 90 on both MCPMTs, measured on 05 October 2023.

The advantage of the new instrument is that the channels of MCPMT1 can be set to a different gain than the channels of MCPMT2. The angular positions with a generally lower light intensity, such as the sideward scattering positions, can then be connected to channels with a higher gain. The forward scattering angular positions that see a higher light intensity can be connected to channels with a lower gain. This allows the measurement of the angular phase function over a larger intensity range. The different gains need to be taken into account when analysing the data.

Fig. C.2 shows the counts of two exemplary channels at different angular positions for a range of gain settings between 95 and 125. The counts are determined in the analog-to-digital converter (ADC) of the PHIPS-POL where 2048 stands for a MCPMT output voltage of 12 V. A homogeneous scattering target is used again as the light source, which is also illuminated with digitally modulated laser pulses from the fiber-coupled OBIS laser at a repetition rate of 40 Hz. The counts are averaged over > 1000 light pulses. The laser power

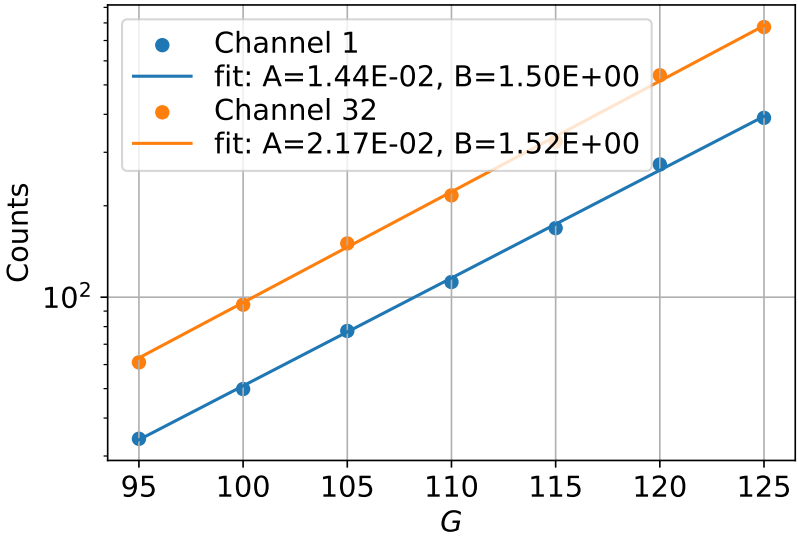

Figure C.2.: Amplification over gain G for exemplary for channels 1 and 32.

is kept constant, and the gains of both MCPMTs are varied between 95 and 125 in steps of five. An exponential function f

$$f(G, A, B) = A \cdot e^{\ln(B) \cdot \frac{G}{5}} \tag{C.1}$$

is fitted to the data of each channel with fit parameters A and B and gain setting G. B is the amplification for a gain increase of five. The exponential function C.1 is in good agreement with the experimental data over the analysed gain range (see fits for exemplary channels 1 and 32 in Fig. C.2).

The function fits to all channels are shown in Fig. C.3. It can be seen that the parameter B is similar for most channels. Channels 2, 3, 15, 16, and 17 deviate because they were optically not connected during the measurements. Channel 24 deviates because it is saturated (2048 counts) on the highest gain settings. These channels are not used for the calculation of the mean of B ($\overline{B}$) that is shown in table C.1. $\overline{B}$ of the two different MCPMTs only deviates by 0.9 %.

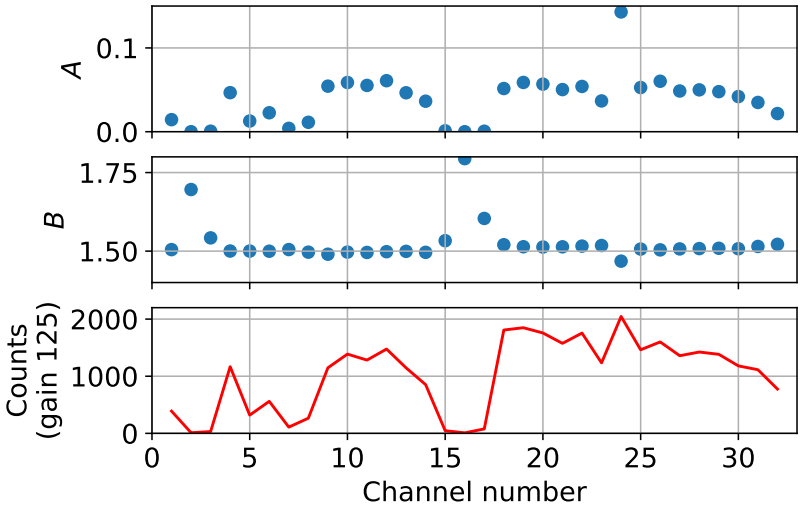

Figure C.3.: Exponential fit parameters A and B and counts at a gain of 125 for all channels of PHIPS-POL.

Function fit	$\bar{B}$	ΔB
Mean	1.506	0.008
MCPMT 1	1.499	0.004
MCPMT 2	1.512	0.005

Table C.1.: The mean $\overline{B}$ and the standard deviation ΔB of parameter B of exponential function fits with equation C.1 to all optically connected and non-saturated MCPMT channels.

In the data analysis of RICE04 equation C.1 and $\overline{B} = 1.506$ are used to normalise the counts of MCPMT2 with the lower gain settings to the counts of the MCPMT1 with the higher gain setting. The normalised counts of a channel of MCPMT1 $\tilde{c_1}$ are given by

$$\tilde{c_1} = c_1 \cdot B^{\frac{G_1 - G_2}{5}} \tag{C.2}$$

where c_1 are the counts of a channel of MCPMTs1, G_1 is the gain setting of MCPMTs1, and G_2 is the gain setting of MCPMTs2. Furthermore, the counts of MCPMT1 are divided by a calibration factor of 0.7103 to obtain the same amplification at the same gain setting at both MCPMTs.

C.2. RICE04 additional information

C.2.1. RICE04 experiment list

Table C.2 shows the experiment list of the RICE04 campaign, including the used instrument settings of PHIPS-POL. Only experiments at cirrus temperatures are shown because only cirrus experiments are analysed in this work. Experiments 22 and 23 are not shown in the table because PHIPS-POL data were not available for these experiments. Additional comments about the individual experiments are given below:

- Exp 07: C1 camera console crashed. Only one C1 image. Triggers only on ice. Settings are optimised for ice. No multiple triggers. C2 images are still sharp with zoom 4. Regrowth with RH_{ice} =1.04 between images [630,1459].
- Exp 08: Triggers only on ice. Settings are optimised for ice. No multiple triggers. C1 images better than before reset of focus but still not great. Regrowth with RH_{ice} = 1.04 between images [1442,2332].
- Exp 09: Regrowth with RH_{ice} = 1.22 between images [2000,2484].
- Exp 10: Regrowth with RH_{ice} = 1.15 between images [550,840].
- Exp 11: Regrowth with RH_{ice} = 1.10 between images [1950,2370].
- Exp 12: Regrowth with RH_{ice} = 1.4 between images [1440,1750]. Large particles in regrowth. Forward channels saturated in regrowth.
- Exp 13: Regrowth with RH_{ice} = 1.3 between images [1437,1778]. Large particles in regrowth.
- Exp 14: Regrowth with RH_{ice} = 1.25 between images [1480,2218].
- Exp 15: Very small particles. TTH needed to be lowered to 50 to getPHIPS triggers. Regrowth with RH_{ice} =1.05 between images [553,1928]. Images are blurry in comparison to -40 °C experiments.
- Exp 16: Scattering laser stray light is affecting counts on 6° and 14° channels through high background counts. Regrowth with RH_{ice} =1.05 between images [1763,3803].
- Exp 17: Regrowth with RH_{ice} = 1.05 between images [2006,5000].

- Exp 18: Regrowth with RH_{ice} = 1.10 between images [2452,4723].
- Exp 19: Regrowth with RH_{ice} = 1.15 between images [200,5890]. Reduced camera delay causes clear images also at -50 °C but possibly issues with scattering data as well.
- Exp 20: Regrowth with RH_{ice} = 1.20 between images [2865,6810] Reduced camera delay causes clear images also at -50 °C but possibly issues with scattering data as well.
- Exp 21: Regrowth with RH_{ice} = 1.25 between images [1544,4280].
- Exp 22: No PHIPS-POL data.
- Exp 23: No PHIPS-POL data.
- Exp 24: Regrowth with RH_{ice} = 1.15 between images [1233,5395].
- Exp 25: Regrowth with RH_{ice} =1.03 between images [717,2400].
- Exp 26: No comments.
- Exp 27: Regrowth with RH_{ice} =1.20 between images [892,2139].
- Exp 28: Regrowth with RH_{ice} =1.10 between images [957,2100].
- Exp 29: Regrowth with RH_{ice} =1.05 between images [1100,2340].
- Exp 30: Laser needed to warm up to 10 °C afterPHIPS power up before measurement could be started.
- Exp 31: Laser turned off due to too cold base plate temperature. Regrowth with RH_{ice} =1.05 between images [769,1037]. Camera delay = 0 µs for images [799,925].
- Exp 32: Regrowth with RH_{ice} =1.25 between images [700,1460] & [1850,1958].

Table C.2.: Experiment list of RICE04 campaign experiments at cirrus temperatures wherePHIPS was operational. Experiment 22 and 23 are omitted because PHIPS-POL data could not be produced.

Name	T_{gas}	Gain 1/ Gain 2	TTH	Glitch	Camera Delay	Zoom C1/C2	Images	Laser power	Aerosol concentration
Exp 07	-40 °C	105/95	60	10 µs	40 µs	3/4	1479	10 mW	Soot: 130 cm^{-3}
Exp 08	-40 °C	105/95	100	10 µs	40 µs	3/4	2338	20 mW	Soot: 70 cm^{-3}
Exp 09	-40 °C	105/95	100	10 µs	40 µs	3/4	2493	20 mW	Soot: 40 cm^{-3}
Exp 10	-40 °C	105/95	100	10 µs	40 µs	3/4	862	20 mW	Soot: 90 cm^{-3}
Exp 11	-40 °C	105/95	130	10 µs	40 µs	3/4	2386	20 mW	Soot: 55 cm^{-3}
Exp 12	-40 °C	105/95	150	10 µs	40 µs	3/4	1778	20 mW	Soot: 35 cm^{-3}
Exp 13	-40 °C	105/95	75	10 µs	40 µs	3/4	1888	10 mW	Soot: 20 cm^{-3}
Exp 14	-40 °C	105/95	150	10 µs	40 µs	3/4	2313	20 mW	Soot: 50 cm^{-3}
Exp 15	-50 °C	105/95	50	10 µs	40 µs	3/4	2110	20 mW	Soot: 27 cm^{-3}
Exp 16	-50 °C	105/95	150	10 µs	40 µs	3/4	4995	150 mW	Soot: 8 cm^{-3}
Exp 17	-50 °C	120/105	150	10 µs	40 µs	3/4	5207	50 mW	Soot: 27 cm^{-3}
Exp 18	-50 °C	125/105	150	10 µs	40 µs	3/4	4781	50 mW	Soot: 5 cm^{-3}
Exp 19	-50 °C	125/105	150	10 µs	0 µs	3/4	6210	50 mW	Soot: 23 cm^{-3}
Exp 20	-50 °C	120/100	150	10 µs	0 µs	3/4	7311	50 mW	Soot: 23 cm^{-3}
Exp 21	-50 °C	115/95	150	10 µs	40 µs	3/4	5266	50 mW	Soot: 25 cm^{-3}
Exp 24	-50 °C	115/95	150	10 µs	40 µs	3/4	5603	50 mW	Soot: 25 cm^{-3}
Exp 25	-50 °C	115/95	150	10 µs	20 µs	3/4	2213	50 mW	Background: 3 cm^{-3}
Exp 26	-50 °C	115/95	150	10 µs	0 µs	3/4	2607	50 mW	Illite: 60 cm^{-3}
Exp 27	-50 °C	115/95	150	10 µs	0 µs	3/4	2880	50 mW	Illite: 37 cm^{-3}
Exp 28	-50 °C	115/95	150	10 µs	0 µs	3/4	2290	50 mW	Illite: 10 cm^{-3}
Exp 29	-50 °C	115/95	150	10 µs	0 µs	3/4	2868	50 mW	Illite: 5 cm^{-3} + Soot: $20 \cdot 10^3$ cm^{-3}
Exp 30	-70 °C	120/100	150	10 µs	0 µs	3/4	372	50 mW	Background: 3 cm^{-3}
Exp 31	-70 °C	125/105	150	10 µs	0-40 µs	3/4	1037	50 mW	Soot: 10 cm^{-3}
Exp 32	-70 °C	125/105	150	10 µs	40 µs	3/4	2001	50 mW	Soot: 3 cm^{-3}

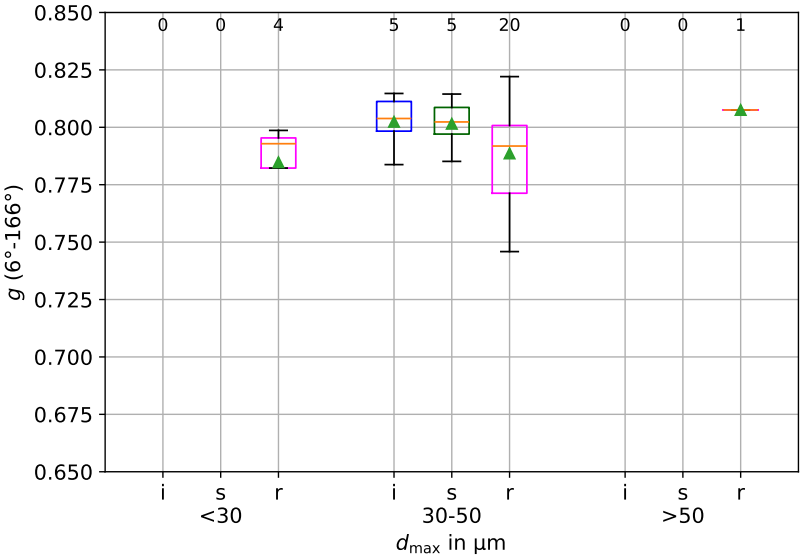

Figure C.4.: Box plots of the asymmetry parameter g during the different phases of the regrowth experiments including the 6° channel. The results are separated into three size groups to reduce the effect of the particle size. In comparison to the initial growth phase, a slight increase in g during the sublimation phase and a strong decrease in g during the regrowth phase are observed.

C.2.2. Figures of RICE04 data including PHIPS-POL 6° channel

In the following section, the analysis of chapter 6 is redone using the full angular scattering function of PHIPS-POL from 6° to 166°. The larger angular range of the angular scattering function leads to a higher retrieval accuracy, while simultaneously a larger uncertainty is induced due to the inclusion of the possibly erroneous 6° detector. Furthermore, the sample size is reduced due to a higher fraction of particle detection events with saturated channels. Fig. C.4,C.5,C.6,C.7,C.8,C.9 use the angular scattering function between 6° and 166° and are equivalent to Fig. 6.5,6.6,6.7,6.8,6.9,6.10, which use the angular scattering function between 14° and 166° in chapter 6.

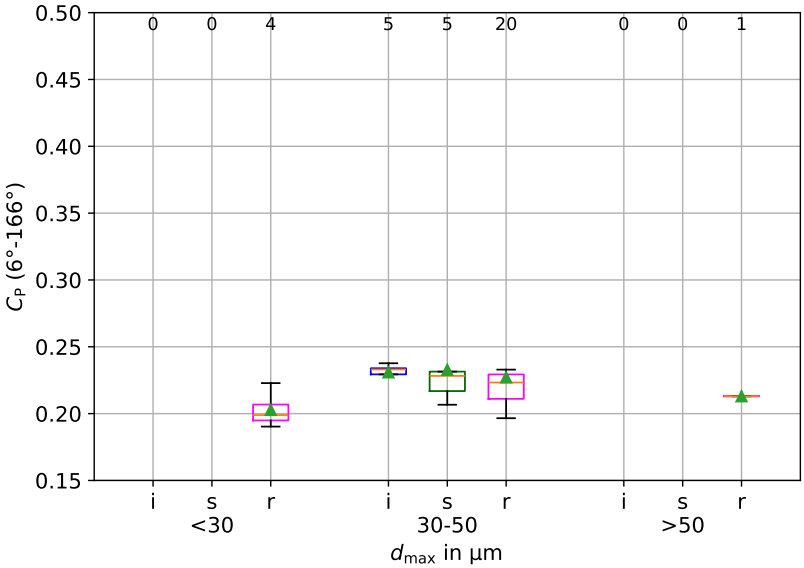

Figure C.5.: Box plots of the complexity parameter C_P during the different phases of the regrowth experiments including the 6° channel. The results are separated into three size groups to reduce the effect of the particle size. In comparison to the initial growth phase, a slight decrease in C_P during the sublimation phase and a strong increase in C_P during the regrowth phase are observed.

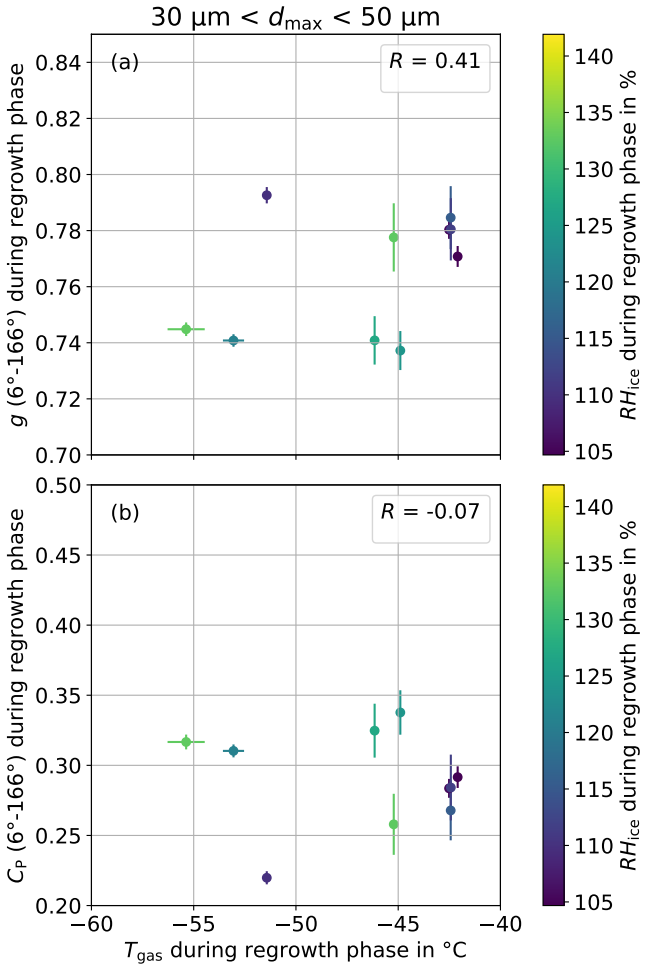

Figure C.6.: Mean asymmetry parameter g **(a)** and mean complexity parameter C_P **(b)** during the regrowth phases of the expansion experiments at constant relative humidity including the 6° channel are shown as a function of the median gas temperature in the AIDA cloud simulation chamber. Particle sizes are restricted to 30 µm to 50 µm to limit the size effect. There is a medium correlation.

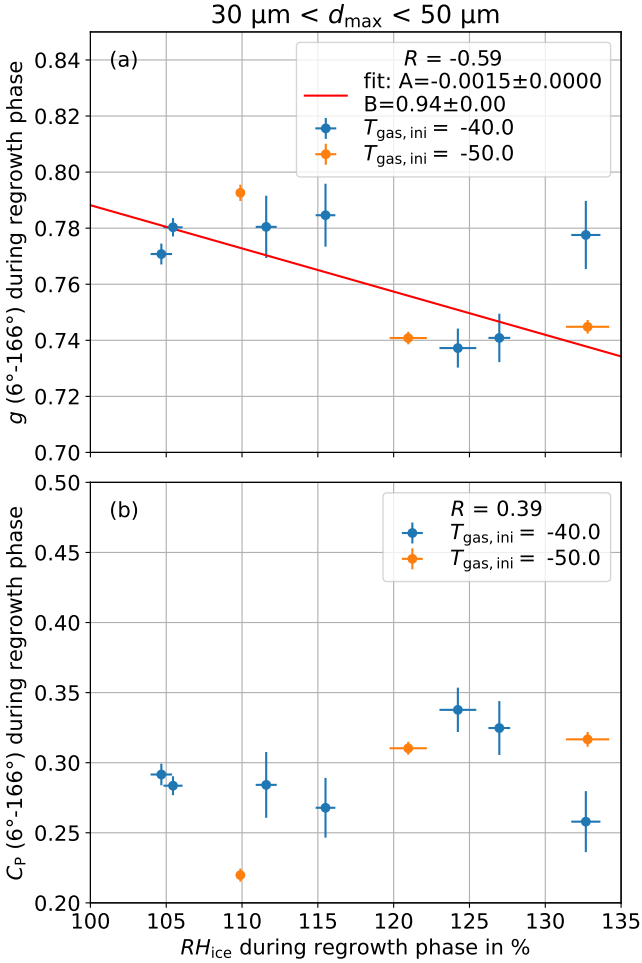

Figure C.7.: Mean asymmetry parameter g **(a)** and mean complexity parameter C_P **(b)** during the regrowth phases of the expansion experiments at constant relative humidity including the 6° channel are shown as function of the relative humidity with respect to ice (RH_{ice}) in the AIDA cloud simulation chamber. Initial gas temperatures of -40 °C and -50 °C are shown in different colour. Particle sizes are restricted to 30 µm to 50 µm to limit the size effect. The Pearson correlation coefficient R shows a medium correlation between g and RH_{ice} and a high correlation between C_P and RH_{ice}.

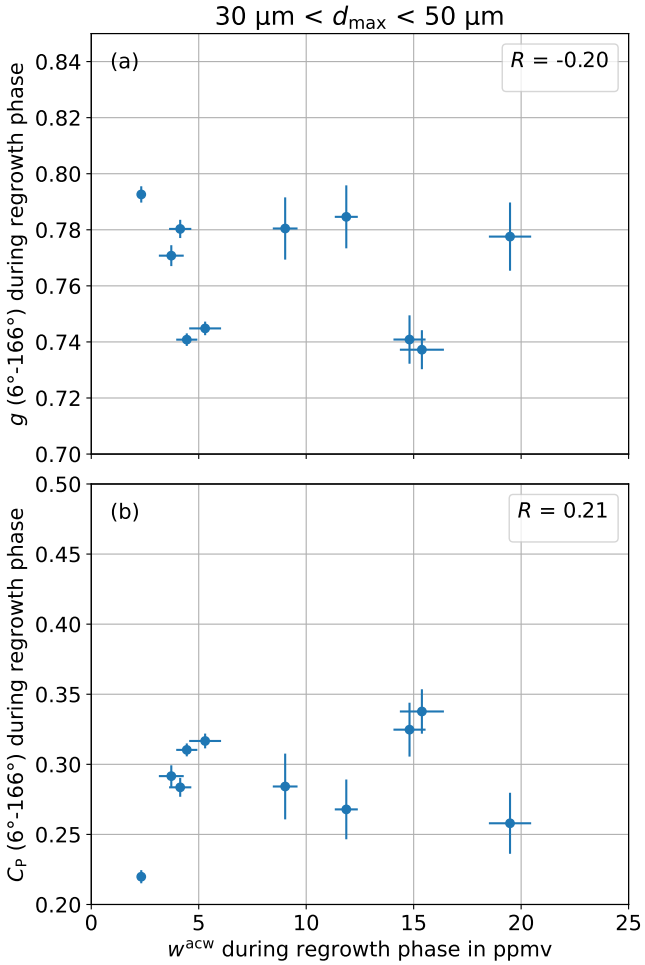

Figure C.8.: Mean asymmetry parameter g **(a)** and mean complexity parameter C_P **(b)** during the regrowth phases of the expansion experiments at constant relative humidity including the 6° channel are shown as function of the mean available condensible water vapour mixing ratio in the AIDA cloud simulation chamber. Particle sizes are restricted to 30 µm to 50 µm to limit the size effect. The Pearson correlation coefficient R shows a low correlation between g and a medium correlation between C_P and RH_{ice}.

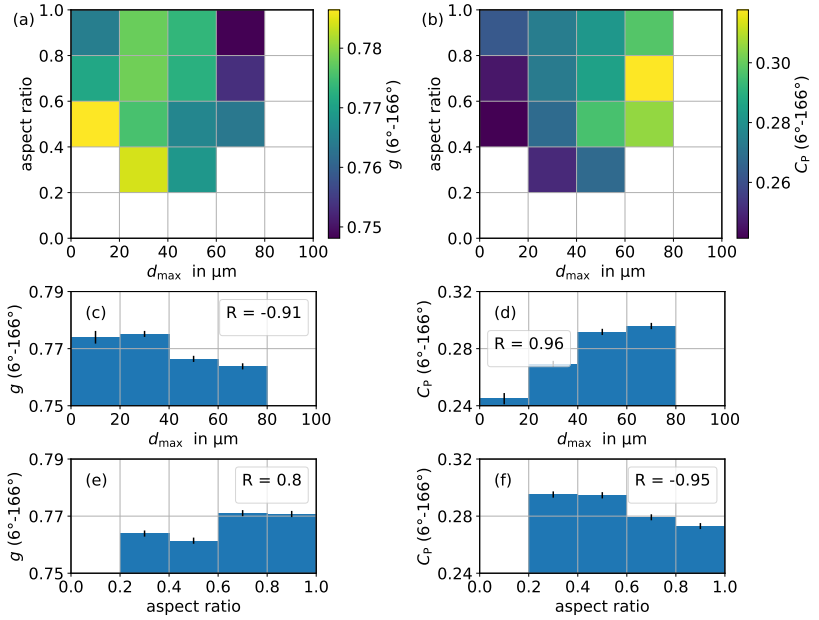

Figure C.9.: Mean of asymmetry parameter g and complexity parameter C_P of individual ice particles of different maximum particle sizes and aspect ratios including the 6° channel are shown in **(a)** and **(b)**, respectively. The influence of particle size on g and C_P for all aspect ratios are shown in **(c)** and **(d)**. The influence of the aspect ratio on g and C_P for all particle sizes are shown in **(e)** and **(f)**. The data includes the complete experiments, not limited to the regrowth phases. Size and aspect ratio groups with less than 50 particles are not shown due to poor statistics (white boxes).

List of Figures

List of Tables

Acknowledgements

I want to thank

- Prof. Thomas Leisner and Prof. Corinna Hoose for being my referee and co-referee.
- Prof. Emma Järvinen and Dr. Martin Schnaiter for the scientific support, the possibility to work with one-of-a-kind instruments, and the possibility to take advantage of their scientific network.
- Dr. Robert Wagner and Dr. Kristina Höhler for scientific discussion.
- My colleges, especially Shawn Wagner, Franziska Rogge, Dr. Alexander Böhmländer, Dr. Tobias Schorr, Johanna Seidel, Dr. Guanglang Xu, and Sepehr Ariaei for a great time at IMKAAF and during the IMPACTS2023 campaign.
- The IMKAAF technical team for support during AIDA campaigns and instrument preparation.
- Dr. Massimo del Guasta for the opportunity to travel to Concordia station and to learn about and experience life and research in Antarctica.
- The technical and scientific team 2023/2024 at Concordia station for great support during my measurements and an amazing time at Dome C.
- Dr. Carl Schmitt for the scientific discussions about ice fog and a great time in Fairbanks, Alaska.
- My colleges at UAF for a great time in Fairbanks, Alaska.
- The GRACE graduate school for the opportunity of a research travel to Fairbanks, Alaska.
- My family and friends for the support.

Bibliography

[1] Ahmed Abdelmonem et al. "PHIPS–HALO: the airborne Particle Habit Imaging and Polar Scattering probe–Part 1: Design and operation". In: *Atmospheric Measurement Techniques* 9.7 (2016), pp. 3131–3144. DOI: 10.5194/amt-9-3131-2016.

[2] American Meteorological Society. *Diamond dust (last access: 30.01.2025)*. URL: https://glossary.ametsoc.org/wiki/Diamond_dust.

[3] American Meteorological Society. *Ice fog (last access: 30.01.2025)*. URL: https://glossary.ametsoc.org/wiki/Ice_fog.

[4] Anna Annibaldi et al. "Direct gravimetric determination of aerosol mass concentration in central antarctica". In: *Analytical chemistry* 83.1 (2011), pp. 143–151. DOI: https://doi.org/10.1021/ac102026w.

[5] Frédérique Auriol et al. "In situ observation of cirrus scattering phase functions with 22 and 46 halos: Cloud field study on 19 February 1998". In: *Journal of the atmospheric sciences* 58.22 (2001), pp. 3376–3390. DOI: 10.1175/1520-0469(2001)058<3376:isoocs>2.0.co;2.

[6] Matthew P Bailey and John Hallett. "A comprehensive habit diagram for atmospheric ice crystals: Confirmation from the laboratory, AIRS II, and other field studies". In: *Journal of the Atmospheric Sciences* 66.9 (2009), pp. 2888–2899. DOI: 10.1175/2009jas2883.1.

[7] Ian Baker. "Imaging dislocations in ice". In: *Microscopy research and technique* 62.1 (2003), pp. 70–82. DOI: 10.1002/jemt.10382.

[8] Anthony J Baran. "From the single-scattering properties of ice crystals to climate prediction: A way forward". In: *Atmospheric Research* 112 (2012), pp. 45–69. DOI: 10.1016/j.atmosres.2012.04.010.

[9] Emanuele Bevacqua, Carl-Friedrich Schleussner, and Jakob Zscheischler. "A year above 1.5° C signals that Earth is most probably within the 20-year period that will reach the Paris Agreement limit". In: *Nature Climate Change* 15.3 (2025), pp. 262–265. DOI: 10.1038/s41558-025-02246-9.

[10] Lei Bi et al. “Efficient implementation of the invariant imbedding T-matrix method and the separation of variables method applied to large nonspherical inhomogeneous particles”. In: *Journal of Quantitative Spectroscopy and Radiative Transfer* 116 (2013), pp. 169–183. DOI: 10.1016/j.jqsrt.2012.11.014.

[11] Alexander Julian Böhmländer et al. “A novel aerosol filter sampler for measuring the vertical distribution of ice-nucleating particles via fixed-wing uncrewed aerial vehicles”. In: *Atmospheric Measurement Techniques Discussions* 2024 (2024), pp. 1–22. DOI: 10.5194/amt-18-3959-2025.

[12] Craig F Bohren and Donald R Huffman. *Absorption and scattering of light by small particles*. John Wiley & Sons, 2004. ISBN: 9780471293408.

[13] Olivier Boucher et al. “Clouds and aerosols”. In: *Climate change 2013: The physical science basis. Contribution of working group I to the fifth assessment report of the intergovernmental panel on climate change*. Cambridge University Press, 2013, pp. 571–657.

[14] James R Campbell et al. “Daytime cirrus cloud top-of-the-atmosphere radiative forcing properties at a midlatitude site and their global consequences”. In: *Journal of Applied Meteorology and Climatology* 55.8 (2016), pp. 1667–1679. DOI: 10.1175/jamc-d-15-0217.1.

[15] João Pereira do Carmo et al. “Atmospheric LIDar (ATLID): pre-launch testing and calibration of the European space agency instrument that will measure aerosols and thin clouds in the atmosphere”. In: *Atmosphere* 12.1 (2021), p. 76. DOI: 10.3390/atmos12010076.

[16] Aurélien Chauvigné et al. “Statistical analysis of contrail to cirrus evolution during the Contrail and Cirrus Experiment (CONCERT)”. In: *Atmospheric Chemistry and Physics* 18.13 (2018), pp. 9803–9822. DOI: 10.5194/acp-18-9803-2018.

[17] Christopher J Cox et al. “Supercooled liquid fogs over the central Greenland Ice Sheet”. In: *Atmospheric Chemistry and Physics* 19.11 (2019), pp. 7467–7485. DOI: 10.5194/acp-19-7467-2019.

[18] Mellissa Cross. “PySPLIT: a Package for the Generation, Analysis, and Visualization of HYSPLIT Air Parcel Trajectories.” In: *SciPy*. 2015, pp. 133–137. DOI: 10.25080/majora-7b98e3ed-014.

[19] Cheng Dang, Charles S Zender, and Mark G Flanner. "Intercomparison and improvement of two-stream shortwave radiative transfer schemes in Earth system models for a unified treatment of cryospheric surfaces". In: *The Cryosphere* 13.9 (2019), pp. 2325–2343. DOI: 10.5194/tc-13-2325-2019.

[20] Elena De La Torre Castro et al. "Differences in microphysical properties of cirrus at high and mid-latitudes". In: *Atmospheric Chemistry and Physics* 23.20 (2023), pp. 13167–13189. DOI: 10.5194/acp-23-13167-2023.

[21] Massimo Del Guasta. "ICE-CAMERA: a flatbed scanner to study inland Antarctic polar precipitation". In: *Atmospheric Measurement Techniques Discussions* 2022 (2022), pp. 1–35. DOI: 10.5194/amt-15-6521-2022.

[22] Massimo Del Guasta. "Simulation of LIDAR returns from pristine and deformed hexagonal ice prisms in cold cirrus by means of "face tracing"". In: *Journal of Geophysical Research: Atmospheres* 106.D12 (2001), pp. 12589–12602. DOI: 10.1029/2000jd900724.

[23] Massimo Del Guasta and Edgar Vallar. "In-cloud variability of LIDAR depolarization of polar and midlatitude cirrus". In: *Geophysical research letters* 30.11 (2003). DOI: 10.1029/2003gl017163.

[24] Massimo Del Guasta et al. "A statistical study of precipitation on the eastern antarctic plateau (Dome-C) using remote sensing and in-situ instrumentation". In: *Polar Science* 42 (2024), p. 101106. DOI: 10.1016/j.polar.2024.101106.

[25] Wolfgang Demtröder. *Experimentalphysik 2: Elektrizität und Optik*. Springer, 2017. ISBN: 9783662557891. DOI: 10.1007/978-3-662-55790-7.

[26] Gianluca Di Natale et al. "Consistency test of precipitating ice cloud retrieval properties obtained from the observations of different instruments operating at Dome C (Antarctica)". In: *Atmospheric Measurement Techniques* 15.24 (2022), pp. 7235–7258. DOI: 10.5194/amt-15-7235-2022.

[27] Bastiaan van Diedenhoven et al. "Remote sensing of ice crystal asymmetry parameter using multi-directional polarization measurements–Part 1: Methodology and evaluation with simulated measurements". In: *Atmospheric Measurement Techniques* 5.10 (2012), pp. 2361–2374. DOI: 10.5194/amt-5-2361-2012.

[28] Bastiaan van Diedenhoven et al. “Remote sensing of ice crystal asymmetry parameter using multi-directional polarization measurements–Part 2: Application to the Research Scanning Polarimeter”. In: *Atmospheric Chemistry and Physics* 13.6 (2013), pp. 3185–3203. DOI: 10.5194/acp-13-3185-2013.

[29] Bastiaan van Diedenhoven et al. “Variation of ice crystal size, shape, and asymmetry parameter in tops of tropical deep convective clouds”. In: *Journal of Geophysical Research: Atmospheres* 119.20 (2014), pp. 11–809. DOI: 10.1002/2014jd022385.

[30] Anna Dittmann et al. “Precipitation regime and stable isotopes at Dome Fuji, East Antarctica”. In: *Atmospheric Chemistry and Physics* 16.11 (2016), pp. 6883–6900. DOI: 10.5194/acp-16-6883-2016.

[31] Erica K Dolinar et al. “Estimation of the Uncertainty in Daytime Cirrus Cloud Radiative Forcing and Heating Rates due to Ice Crystal Optics”. In: *Journal of Applied Meteorology and Climatology* 64.5 (2025), pp. 513–527. DOI: 10.1175/jamc-d-24-0065.1.

[32] Bruce T Draine and Piotr J Flatau. “Discrete-dipole approximation for scattering calculations”. In: *Josa a* 11.4 (1994), pp. 1491–1499. DOI: 10.1364/josaa.11.001491.

[33] LF Evans. “Two-dimensional nucleation of ice”. In: *Nature* 213.5074 (1967), pp. 384–385. DOI: 10.1038/213384a0.

[34] David W Fahey et al. “The AquaVIT-1 intercomparison of atmospheric water vapor measurement techniques”. In: *Atmospheric Measurement Techniques* 7.9 (2014), pp. 3177–3213. DOI: 10.5194/amt-7-3177-2014.

[35] I Fattori et al. “Chemical composition and physical features of summer aerosol at Terra Nova Bay and Dome C, Antarctica”. In: *Journal of Environmental Monitoring* 7.12 (2005), pp. 1265–1274. DOI: 10.1039/b507327h.

[36] Guy Febvre et al. “On optical and microphysical characteristics of contrails and cirrus”. In: *Journal of Geophysical Research: Atmospheres* 114.D2 (2009). DOI: 10.1029/2008jd010184.

[37] Graham Feingold and Zev Levin. “The lognormal fit to raindrop spectra from frontal convective clouds in Israel”. In: *Journal of climate and applied meteorology* (1986), pp. 1346–1363. DOI: 10.1175/1520-0450(1986)025<1346:tlftrs>2.0.co;2.

[38] Qiang Fu. "A new parameterization of an asymmetry factor of cirrus clouds for climate models". In: *Journal of the Atmospheric Sciences* 64.11 (2007), pp. 4140–4150. DOI: 10.1175/2007jas2289.1.

[39] Joanna M Futyan and Anthony D Del Genio. "Deep convective system evolution over Africa and the tropical Atlantic". In: *Journal of Climate* 20.20 (2007), pp. 5041–5060. DOI: 10.1175/jcli4297.1.

[40] Timothy J Garrett, Peter V Hobbs, and H Gerber. "Shortwave, single-scattering properties of arctic ice clouds". In: *Journal of Geophysical Research: Atmospheres* 106.D14 (2001), pp. 15155–15172. DOI: 10.1029/2000jd900195.

[41] Timothy J Garrett et al. "Small, highly reflective ice crystals in low-latitude cirrus". In: *Geophysical Research Letters* 30.21 (2003). DOI: 10.1029/2003gl018153.

[42] Jean François Gayet et al. "Microphysical and optical properties of midlatitude cirrus clouds observed in the southern hemisphere during INCA". In: *Quarterly Journal of the Royal Meteorological Society: A journal of the atmospheric sciences, applied meteorology and physical oceanography* 132.621 (2006), pp. 2719–2748. DOI: 10.1256/qj.05.162.

[43] Jean-François Gayet et al. "Cirrus cloud microphysical and optical properties at southern and northern midlatitudes during the INCA experiment". In: *Journal of Geophysical Research: Atmospheres* 109.D20 (2004). DOI: 10.1029/2004jd004803.

[44] Jean-François Gayet et al. "Optical properties of pristine ice crystals in mid-latitude cirrus clouds: a case study during CIRCLE-2 experiment". In: *Atmospheric Chemistry and Physics* 11.6 (2011), pp. 2537–2544. DOI: 10.5194/acp-11-2537-2011.

[45] Jean-François Gayet et al. "Quantitative measurement of the microphysical and optical properties of cirrus clouds with four different in situ probes: Evidence of small ice crystals". In: *Geophysical research letters* 29.24 (2002), pp. XXX–XXX. DOI: 10.1029/2001gl014342.

[46] Christophe Genthon et al. "Atmospheric moisture supersaturation in the near-surface atmosphere at Dome C, Antarctic Plateau". In: *Atmospheric Chemistry and Physics* 17.1 (2017), pp. 691–704. DOI: 10.5194/acp-17-691-2017.

[47] Christophe Genthon et al. “Water vapor in cold and clean atmosphere: a 3-year data set in the boundary layer of Dome C, East Antarctic Plateau”. In: *Earth System Science Data* 14.4 (2022), pp. 1571–1580. DOI: 10.5194/essd-14-1571-2022.

[48] Hans-Ulrich Gerber et al. “Nephelometer measurements of the asymmetry parameter, volume extinction coefficient, and backscatter ratio in Arctic clouds”. In: *Journal of the atmospheric sciences* 57.18 (2000), pp. 3021–3034. DOI: 10.1175/1520-0469(2000)057<3021:nmotap>2.0.co;2.

[49] Eric Girard and Jean-Pierre Blanchet. “Microphysical parameterization of Arctic diamond dust, ice fog, and thin stratus for climate models”. In: *Journal of the Atmospheric Sciences* 58.10 (2001), pp. 1181–1198. DOI: 10.1175/1520-0469(2001)058<1181:mpoadd>2.0.co;2.

[50] Eric Girard and Jean-Pierre Blanchet. “Simulation of Arctic diamond dust, ice fog, and thin stratus using an explicit aerosol–cloud–radiation model”. In: *Journal of the Atmospheric Sciences* 58.10 (2001), pp. 1199–1221. DOI: 10.1175/1520-0469(2001)058<1199:soaddi>2.0.co;2.

[51] Ivan Gladich et al. “Mechanism of anisotropic surface self-diffusivity at the prismatic ice–vapor interface”. In: *Physical Chemistry Chemical Physics* 17.35 (2015), pp. 22947–22958. DOI: 10.1039/c5cp01330e.

[52] Diego A Gouveia et al. “Optical and geometrical properties of cirrus clouds in Amazonia derived from 1 year of ground-based lidar measurements”. In: *Atmospheric Chemistry and Physics* 17.5 (2017), pp. 3619–3636. DOI: 10.5194/acp-17-3619-2017.

[53] Paolo Grigioni et al. “Dati meteorologici della Stazione meteorologica CONCORDIA presso la Base CONCORDIA STATION (DomeC)”. In: *ENEA* (2022). DOI: 10.12910/DATASET2022-002.

[54] Silke Groß et al. “Investigating an indirect aviation effect on mid-latitude cirrus clouds–linking lidar-derived optical properties to in situ measurements”. In: *Atmospheric Chemistry and Physics* 23.14 (2023), pp. 8369–8381. DOI: 10.5194/acp-23-8369-2023.

[55] Ismail Gultepe et al. “Ice fog: The current state of knowledge and future challenges”. In: *Meteorological Monographs* 58 (2017), pp. 4–1. DOI: 10.1175/amsmonographs-d-17-0002.1.

[56] Taryn Haladay and Graeme Stephens. "Characteristics of tropical thin cirrus clouds deduced from joint CloudSat and CALIPSO observations". In: *Journal of Geophysical Research: Atmospheres* 114.D8 (2009). DOI: 10.1029/2008jd010675.

[57] Hamamatsu. *Multianode photomultiplier tube assembly H10515B-20 (last access: 18.11.2024)*. URL: https://www.hamamatsu.com/content/dam/hamamatsu-photonics/sites/documents/99_SALES_LIBRARY/etd/LINEAR_PMT_TPMH1325E.pdf.

[58] Adrian Hamel et al. "Cloud Chamber Studies on the Linear Depolarisation Ratio of Small Cirrus Ice Crystals". In: *EGUsphere* 2025 (2025), pp. 1–32. DOI: 10.5194/egusphere-2025-3515.

[59] Jerry Y Harrington and Gwenore F Pokrifka. "An Approximate Criterion for Morphological Transformations in Small Vapor Grown Ice Crystals". In: *Journal of the Atmospheric Sciences* 81.2 (2024), pp. 401–416. DOI: 10.1175/JAS-D-23-0131.1.

[60] Klaus G Heumann. "Determination of inorganic and organic traces in the clean room compartment of Antarctica". In: *Analytica chimica acta* 283.1 (1993), pp. 230–245. DOI: 10.1016/0003-2670(93)85227-b.

[61] Andrew J Heymsfield et al. "Cirrus clouds". In: *Meteorological Monographs* 58 (2017), pp. 2–1. DOI: 10.1175/amsmonographs-d-16-0010.1.

[62] Robin J Hogan and Alessio Bozzo. *ECRAD: A new radiation scheme for the IFS*. Vol. 787. European Centre for Medium-Range Weather Forecasts Reading, UK, 2016. DOI: 10.21957/whntqkfdz.

[63] Institut polaire français. *Concordia Station (last access: 13.02.2025)*. URL: https://institut-polaire.fr/en/antarctica/concordia-station/.

[64] Etienne Jambon-Puillet, Noushine Shahidzadeh, and Daniel Bonn. "Singular sublimation of ice and snow crystals". In: *Nature communications* 9.1 (2018), p. 4191. DOI: 10.1038/s41467-018-06689-x.

[65] Emma Järvinen. *Investigations of Angular Light Scattering by Complex Atmospheric Particles*. KIT Scientific Publishing, 2016. DOI: 10.5445/KSP/1000056601.

[66] Emma Järvinen and Franz Martin Schnaiter. "Low and Consistent Asymmetry Parameters in Arctic and Mid-latitude Cirrus". In: *EGUsphere* 2025 (2025), pp. 1–27. DOI: 10.5194/egusphere-2025-3065.

[67] Emma Järvinen, Heini Wernli, and Martin Schnaiter. "Investigations of mesoscopic complexity of small ice crystals in midlatitude cirrus". In: *Geophysical Research Letters* 45.20 (2018), pp. 11–465. DOI: 10.1029/2018gl079079.

[68] Emma Järvinen et al. "Additional global climate cooling by clouds due to ice crystal complexity". In: *Atmospheric Chemistry and Physics* 18.21 (2018), pp. 15767–15781. DOI: 10.5194/acp-18-15767-2018.

[69] Emma Järvinen et al. "Ice Crystal Complexity and Link to the Cirrus Cloud Radiative Effect". In: *Clouds and their Climatic Impacts: Radiation, Circulation, and Precipitation* (2023), pp. 47–85. DOI: 10.1002/9781119700357.ch3.

[70] Emma Järvinen et al. "Quasi-spherical ice in convective clouds". In: *Journal of the Atmospheric Sciences* 73.10 (2016), pp. 3885–3910. DOI: 10.1175/jas-d-15-0365.1.

[71] Emma Järvinen et al. "Seasonal cycle and modal structure of particle number size distribution at Dome C, Antarctica". In: *Atmospheric Chemistry and Physics* 13.15 (2013), pp. 7473–7487. DOI: 10.5194/acp-13-7473-2013.

[72] Andrew Jarvis and Piers M Forster. "Estimated human-induced warming from a linear temperature and atmospheric CO2 relationship". In: *Nature Geoscience* 17.12 (2024), pp. 1222–1224. DOI: 10.1038/s41561-024-01580-5.

[73] Alexandria Johnson et al. "Difficulties in early ice detection with the Small Ice Detector-2 HIAPER (SID-2H) in maritime cumuli". In: *Journal of Atmospheric and Oceanic Technology* 31.6 (2014), pp. 1263–1275. DOI: 10.1175/jtech-d-13-00079.1.

[74] Olivier Jourdan et al. "Assessment of cloud optical parameters in the solar region: Retrievals from airborne measurements of scattering phase functions". In: *Journal of Geophysical Research: Atmospheres* 108.D18 (2003). DOI: 10.1029/2003jd003493.

[75] Zamin A Kanji et al. "Overview of ice nucleating particles". In: *Meteorological monographs* 58 (2017), pp. 1–1. DOI: 10.1175/amsmonographs-d-16-0006.1.

[76] Paul H Kaye et al. "Classifying atmospheric ice crystals by spatial light scattering". In: *Optics letters* 33.13 (2008), pp. 1545–1547. DOI: 10.1364/ol.33.001545.

[77] Gottfried Kirchengast and Moritz Pichler. "A traceable global warming record and clarity for the 1.5° C and well-below-2° C goals". In: *Communications Earth & Environment* 6.1 (2025), p. 402. DOI: 10.1038/s43247-025-02368-0.

[78] Thomas Koop et al. "Water activity as the determinant for homogeneous ice nucleation in aqueous solutions". In: *Nature* 406.6796 (2000), pp. 611–614. DOI: 10.1038/35020537.

[79] Martina Krämer et al. "A microphysics guide to cirrus clouds–Part 1: Cirrus types". In: *Atmospheric Chemistry and Physics* 16.5 (2016), pp. 3463–3483. DOI: 10.5194/acp-16-3463-2016.

[80] Martina Krämer et al. "A microphysics guide to cirrus–Part 2: Climatologies of clouds and humidity from observations". In: *Atmospheric Chemistry and Physics* 20.21 (2020), pp. 12569–12608. DOI: 10.5194/acp-20-12569-2020.

[81] Werner F Kuhs et al. "Extent and relevance of stacking disorder in "ice Ic"". In: *Proceedings of the National Academy of Sciences* 109.52 (2012), pp. 21259–21264. DOI: 10.1073/pnas.1210331110.

[82] Natalia Kustova et al. "Depolarization Ratio for Randomly Oriented Ice Crystals of Cirrus Clouds". In: *Atmosphere* 13.10 (2022), p. 1551. DOI: 10.3390/atmos13101551.

[83] R Paul Lawson and Andrew Gettelman. "Impact of Antarctic mixed-phase clouds on climate". In: *Proceedings of the National Academy of Sciences* 111.51 (2014), pp. 18156–18161. DOI: 10.1073/pnas.1418197111.

[84] R Paul Lawson et al. "A review of ice particle shapes in cirrus formed in situ and in anvils". In: *Journal of Geophysical Research: Atmospheres* 124.17-18 (2019), pp. 10049–10090. DOI: 10.1029/2018jd030122.

[85] R Paul Lawson et al. "Microphysical and optical properties of atmospheric ice crystals at South Pole Station". In: *Journal of Applied Meteorology and Climatology* 45.11 (2006), pp. 1505–1524. DOI: 10.1175/jam2421.1.

[86] Hoesung Lee et al. *Climate change 2023: synthesis report. Contribution of working groups I, II and III to the sixth assessment report of the intergovernmental panel on climate change*. IPCC, 2023. DOI: 10.59327/IPCC/AR6-9789291691647.

[87] Jussi Leinonen. "High-level interface to T-matrix scattering calculations: architecture, capabilities and limitations". In: *Optics express* 22.2 (2014), pp. 1655–1660. DOI: 10.1364/oe.22.001655.

[88] Qiang Li and Silke Groß. "Changes in cirrus cloud properties and occurrence over Europe during the COVID-19-caused air traffic reduction". In: *Atmospheric Chemistry and Physics* 21.19 (2021), pp. 14573–14590. DOI: 10.5194/acp-21-14573-2021.

[89] Emily Lill et al. "The abundance and sources of ice nucleating particles within Alaskan ice fog". In: *Journal of Geophysical Research: Atmospheres* 129.16 (2024), e2024JD041170. DOI: 10.1029/2024jd041170.

[90] Kuo-Nan Liou and Henry Lahore. "Laser sensing of cloud composition: a backscattered depolarization technique". In: *Journal of Applied Meteorology and Climatology* 13.2 (1974), pp. 257–263. DOI: 10.1175/1520-0450(1974)013<0257:lsocca>2.0.co;2.

[91] Constantino Listowski and Tom Lachlan-Cope. "The microphysics of clouds over the Antarctic Peninsula–Part 2: modelling aspects within Polar WRF". In: *Atmospheric Chemistry and Physics* 17.17 (2017), pp. 10195–10221. DOI: 10.5194/acp-17-10195-2017.

[92] Chao Liu, R Lee Panetta, and Ping Yang. "The effects of surface roughness on the scattering properties of hexagonal columns with sizes from the Rayleigh to the geometric optics regimes". In: *Journal of Quantitative Spectroscopy and Radiative Transfer* 129 (2013), pp. 169–185. DOI: 10.1016/j.jqsrt.2013.06.011.

[93] Chao Liu et al. "A two-habit model for the microphysical and optical properties of ice clouds". In: *Atmospheric Chemistry and Physics* 14.24 (2014), pp. 13719–13737. DOI: 10.5194/acp-14-13719-2014.

[94] Ulrike Lohmann and Erich Roeckner. "Influence of cirrus cloud radiative forcing on climate and climate sensitivity in a general circulation model". In: *Journal of Geophysical Research: Atmospheres* 100.D8 (1995), pp. 16305–16323. DOI: 10.1029/95jd01383.

[95] Rong-Sheng Lu et al. "Grinding surface roughness measurement based on the co-occurrence matrix of speckle pattern texture". In: *Applied Optics* 45.35 (2006), pp. 8839–8847. DOI: 10.1364/ao.45.008839.

[96] Kai Lyu et al. "Orographic cirrus and its radiative forcing in NCAR CAM6". In: *Journal of Geophysical Research: Atmospheres* 128.10 (2023), e2022JD038164. DOI: 10.1029/2022jd038164.

[97] Andreas Macke. “rt-mc”. In: *Zenodo* (July 2020). DOI: 10.5281/zenodo.3965572. URL: https://doi.org/10.5281/zenodo.3965572.

[98] Andreas Macke, Michael I Mishchenko, and Brian Cairns. “The influence of inclusions on light scattering by large ice particles”. In: *Journal of Geophysical Research: Atmospheres* 101.D18 (1996), pp. 23311–23316. DOI: 10.1029/96jd02364.

[99] Andreas Macke, Johannes Mueller, and Ehrhard Raschke. “Single scattering properties of atmospheric ice crystals”. In: *Journal of Atmospheric Sciences* 53.19 (1996), pp. 2813–2825. DOI: 10.1175/1520-0469(1996)053<2813:sspoai>2.0.co;2.

[100] Andreas Macke et al. “Scattering of light by large nonspherical particles: ray-tracing approximation versus T-matrix method”. In: *Optics Letters* 20.19 (1995), pp. 1934–1936. DOI: 10.1364/ol.20.001934.

[101] Andreas Macke et al. “The role of ice particle shapes and size distributions in the single scattering properties of cirrus clouds”. In: *Journal of the atmospheric sciences* 55.17 (1998), pp. 2874–2883. DOI: 10.1175/1520-0469(1998)055<2874:troips>2.0.co;2.

[102] Alexander V Matus and Tristan S L’Ecuyer. “The role of cloud phase in Earth’s radiation budget”. In: *Journal of Geophysical Research: Atmospheres* 122.5 (2017), pp. 2559–2578. DOI: 10.1002/2016jd025951.

[103] Angelos Michaelides and Ben Slater. “Melting the ice one layer at a time”. In: *Proceedings of the National Academy of Sciences* 114.2 (2017), pp. 195–197. DOI: 10.1073/pnas.1619259114.

[104] Natasha L Miles, Johannes Verlinde, and Eugene E Clothiaux. “Cloud droplet size distributions in low-level stratiform clouds”. In: *Journal of the atmospheric sciences* 57.2 (2000), pp. 295–311. DOI: 10.1175/1520-0469(2000)057<0295:cdsdil>2.0.co;2.

[105] Guillaume Mioche et al. “Validation of the CALIPSO-CALIOP extinction coefficients from in situ observations in midlatitude cirrus clouds during the CIRCLE-2 experiment”. In: *Journal of Geophysical Research: Atmospheres* 115.D4 (2010). DOI: 10.1029/2009jd012376.

[106] Michael Mishchenko and Joop W. Hovenier. “Depolarization of light backscattered by randomly oriented nonspherical particles”. In: *Optics letters* 20.12 (1995), pp. 1356–1358. DOI: 10.1364/ol.20.001356.

[107] Michael I Mishchenko and Larry D Travis. "Capabilities and limitations of a current FORTRAN implementation of the T-matrix method for randomly oriented, rotationally symmetric scatterers". In: *Journal of Quantitative Spectroscopy and Radiative Transfer* 60.3 (1998), pp. 309–324. DOI: 10.1016/s0022-4073(98)00008-9.

[108] Michael I Mishchenko, Larry D Travis, and Andrew A Lacis. *Scattering, absorption, and emission of light by small particles*. Cambridge university press, 2002. ISBN: 9780521782524.

[109] Michael I Mishchenko, Larry D Travis, and Daniel W Mackowski. "T-matrix computations of light scattering by nonspherical particles: A review". In: *Journal of Quantitative Spectroscopy and Radiative Transfer* 55.5 (1996), pp. 535–575. DOI: 10.1016/0022-4073(96)00002-7.

[110] David Mitchell, RP Lawson, and B Baker. "Understanding effective diameter and its application to terrestrial radiation in ice clouds". In: *Atmospheric Chemistry and Physics* 11.7 (2011), pp. 3417–3429. DOI: 10.5194/acp-11-3417-2011.

[111] Ottmar Möhler et al. "Effect of sulfuric acid coating on heterogeneous ice nucleation by soot aerosol particles". In: *Journal of Geophysical Research: Atmospheres* 110.D11 (2005). DOI: 10.1029/2004jd005169.

[112] JT Nelson and MB Baker. "New theoretical framework for studies of vapor growth and sublimation of small ice crystals in the atmosphere". In: *Journal of Geophysical Research: Atmospheres* 101.D3 (1996), pp. 7033–7047. DOI: 10.1029/95jd03162.

[113] Vincent Noel et al. "Classification of particle effective shape ratios in cirrus clouds based on the lidar depolarization ratio". In: *Applied optics* 41.21 (2002), pp. 4245–4257. DOI: 10.1364/ao.41.004245.

[114] Stephen P Palm et al. "Satellite remote sensing of blowing snow properties over Antarctica". In: *Journal of Geophysical Research: Atmospheres* 116.D16 (2011). DOI: 10.1029/2011jd015828.

[115] R Lee Panetta, Chao Liu, and Ping Yang. "A pseudo-spectral time domain method for light scattering computation". In: *Light Scattering Reviews 8: Radiative transfer and light scattering* (2013), pp. 139–188. DOI: 10.1007/978-3-642-32106-1_4.

[116] Rebecca M Pauly et al. "Cloud-Aerosol Transport System (CATS) 1064 nm calibration and validation". In: *Atmospheric measurement techniques* 12.11 (2019), pp. 6241–6258. DOI: 10.5194/amt-12-6241-2019.

[117] Scott Prahl. "miepython: Pure python calculation of Mie scattering". Version 2.5.4. In: *Zenodo [code]* (May 2024). DOI: 10.5281/zenodo.11135148. URL: https://doi.org/10.5281/zenodo.11135148.

[118] Philippe Ricaud et al. "Supercooled liquid water cloud observed, analysed, and modelled at the top of the planetary boundary layer above Dome C, Antarctica". In: *Atmospheric Chemistry and Physics* 20.7 (2020), pp. 4167–4191. DOI: 10.5194/acp-20-4167-2020.

[119] Matteo Rinaldi et al. "Ice-nucleating particle concentration measurements from Ny-Ålesund during the Arctic spring–summer in 2018". In: *Atmospheric Chemistry and Physics* 21.19 (2021), pp. 14725–14748. DOI: 10.5194/acp-21-14725-2021.

[120] Masanori Saito and Ping Yang. "Quantifying the Impact of the Surface Roughness of Hexagonal Ice Crystals on Backscattering Properties for Lidar-Based Remote Sensing Applications". In: *Geophysical Research Letters* 50.18 (2023), e2023GL104175. DOI: 10.1029/2023gl104175.

[121] Masanori Saito et al. "A comprehensive database of the optical properties of irregular aerosol particles for radiative transfer simulations". In: *Journal of the Atmospheric Sciences* 78.7 (2021), pp. 2089–2111. DOI: 10.1175/jas-d-20-0338.1.

[122] Gianni Santachiara, F Belosi, and F Prodi. "Ice crystal precipitation at Dome C site (East Antarctica)". In: *Atmospheric Research* 167 (2016), pp. 108–117. DOI: 10.1016/j.atmosres.2015.08.006.

[123] Kenneth Sassen. "The polarization lidar technique for cloud research: A review and current assessment". In: *Bulletin of the American Meteorological Society* 72.12 (1991), pp. 1848–1866. DOI: 10.1175/1520-0477(1991)072<1848:tpltfc>2.0.co;2.

[124] Kenneth Sassen and Sally Benson. "A midlatitude cirrus cloud climatology from the Facility for Atmospheric Remote Sensing. Part II: Microphysical properties derived from lidar depolarization". In: *Journal of the Atmospheric Sciences* 58.15 (2001), pp. 2103–2112. DOI: 10.1175/1520-0469(2001)058<2103:amcccf>2.0.co;2.

[125] Kenneth Sassen, Vinay Kumar Kayetha, and Jiang Zhu. "Ice cloud depolarization for nadir and off-nadir CALIPSO measurements". In: *Geophysical research letters* 39.20 (2012). DOI: 10.1029/2012gl053116.

[126] Kenneth Sassen, Wang Zhien, and Liu Dong. "Global distribution of cirrus clouds from CloudSat". In: *Journal of geophysical research* 114.D8 (2009). DOI: 10.1029/2008JD009972.

[127] Kenneth Sassen and Jiang Zhu. "A global survey of CALIPSO linear depolarization ratios in ice clouds: Initial findings". In: *Journal of Geophysical Research: Atmospheres* 114.D4 (2009). DOI: 10.1029/2009jd012279.

[128] Florian Sauerland et al. "Ice-nucleating particle concentration impacts cloud properties over Dronning Maud Land, East Antarctica, in COSMO-CLM2". In: *Atmospheric Chemistry and Physics* 24.23 (2024), pp. 13751–13768. DOI: 10.5194/acp-24-13751-2024.

[129] Gen Sazaki et al. "Elementary steps at the surface of ice crystals visualized by advanced optical microscopy". In: *Proceedings of the National Academy of Sciences* 107.46 (2010), pp. 19702–19707. DOI: 10.1073/pnas.1008866107.

[130] Elisabeth Schlosser et al. "Precipitation and synoptic regime in two extreme years 2009 and 2010 at Dome C, Antarctica–implications for ice core interpretation". In: *Atmospheric Chemistry and Physics* 16.8 (2016), pp. 4757–4770. DOI: 10.5194/acp-16-4757-2016.

[131] Carl G Schmitt and Andrew J Heymsfield. "On the occurrence of hollow bullet rosette–and column-shaped ice crystals in midlatitude cirrus". In: *Journal of the atmospheric sciences* 64.12 (2007), pp. 4514–4519. DOI: 10.1175/2007jas2317.1.

[132] Carl G Schmitt et al. "Classification of ice particle shapes using machine learning on forward light scattering images". In: *Artificial Intelligence for the Earth Systems* (2024). DOI: 10.1175/aies-d-23-0091.1.

[133] Carl G Schmitt et al. "Microphysical characterization of boundary layer ice particles: results from a 3-year measurement campaign in interior Alaska". In: *Journal of Applied Meteorology and Climatology* (2024). DOI: 10.1175/jamc-d-23-0190.1.

[134] Carl G Schmitt et al. “The microphysical properties of ice fog measured in urban environments of Interior Alaska”. In: *Journal of Geophysical Research: Atmospheres* 118.19 (2013), pp. 11–136. DOI: 10.1002/jgrd.50822.

[135] Martin Schnaiter et al. “Cloud chamber experiments on the origin of ice crystal complexity in cirrus clouds”. In: *Atmospheric Chemistry and Physics* 16.8 (2016), pp. 5091–5110. DOI: 10.5194/acp-16-5091-2016.

[136] Martin Schnaiter et al. “Influence of particle size and shape on the backscattering linear depolarisation ratio of small ice crystals–cloud chamber measurements in the context of contrail and cirrus microphysics”. In: *Atmospheric Chemistry and Physics* 12.21 (2012), pp. 10465–10484. DOI: 10.5194/acp-12-10465-2012.

[137] Martin Schnaiter et al. “PHIPS-HALO: the airborne particle habit imaging and polar scattering probe–Part 2: Characterization and first results”. In: *Atmospheric measurement techniques* 11.1 (2018), pp. 341–357. DOI: 10.5194/amt-11-341-2018.

[138] Julia Schneider et al. “High homogeneous freezing onsets of sulfuric acid aerosol at cirrus temperatures”. In: *Atmospheric Chemistry and Physics* 21.18 (2021), pp. 14403–14425. DOI: 10.5194/acp-21-14403-2021.

[139] Roland Schön et al. “Particle habit imaging using incoherent light: a first step toward a novel instrument for cloud microphysics”. In: *Journal of Atmospheric and Oceanic Technology* 28.4 (2011), pp. 493–512. DOI: 10.1175/2011JTECHA1445.1.

[140] Valery Shcherbakov et al. “Light scattering by single ice crystals of cirrus clouds”. In: *Geophysical research letters* 33.15 (2006). DOI: 10.1029/2006gl026055.

[141] Karen Simonyan and Andrew Zisserman. “Very deep convolutional networks for large-scale image recognition”. In: *arXiv preprint arXiv:1409.1556* (2014). DOI: 10.48550/arXiv.1409.1556.

[142] Dharmendra Kumar Singh, Swarnali Sanyal, and Donald J Wuebbles. “Understanding the role of contrails and contrail cirrus in climate change: a global perspective”. In: *Atmospheric Chemistry and Physics* 24.16 (2024), pp. 9219–9262. DOI: 10.5194/acp-24-9219-2024.

[143] Helen R Smith et al. "Exact and near backscattering measurements of the linear depolarisation ratio of various ice crystal habits generated in a laboratory cloud chamber". In: *Journal of Quantitative Spectroscopy and Radiative Transfer* 178 (2016), pp. 361–378. DOI: 10.1016/j.jqsrt.2016.01.030.

[144] Ariel F Stein et al. "NOAA's HYSPLIT atmospheric transport and dispersion modeling system". In: *Bulletin of the American Meteorological Society* 96.12 (2015), pp. 2059–2077. DOI: 10.1175/bams-d-14-00110.1.

[145] Claudia J Stubenrauch et al. "Assessment of global cloud datasets from satellites: Project and database initiated by the GEWEX radiation panel". In: *Bulletin of the American Meteorological Society* 94.7 (2013), pp. 1031–1049. DOI: 10.1175/bams-d-12-00117.

[146] Claudia J Stubenrauch et al. "Cloud climatologies from the infrared sounders AIRS and IASI: strengths and applications". In: *Atmospheric Chemistry and Physics* 17.22 (2017), pp. 13625–13644.

[147] Karlsruhe Institute of Technology. *AIDA-Scheme (last access: 18.11.2024)*. URL: https://www.imk-aaf.kit.edu/img/04_AIDA-Scheme.jpg.

[148] Lin Tian et al. "A study of cirrus ice particle size distribution using TC4 observations". In: *Journal of the atmospheric sciences* 67.1 (2010), pp. 195–216. DOI: 10.1175/2009jas3114.1.

[149] George Tselioudis, William B Rossow, and David Rind. "Global patterns of cloud optical thickness variation with temperature". In: *Journal of climate* 5.12 (1992), pp. 1484–1495. DOI: 10.1175/1520-0442(1992)005<1484:gpocot>2.0.co;2.

[150] Zbigniew Ulanowski et al. "Incidence of rough and irregular atmospheric ice particles from Small Ice Detector 3 measurements". In: *Atmospheric Chemistry and Physics* 14.3 (2014), pp. 1649–1662. DOI: 10.5194/acp-14-1649-2014.

[151] Zbigniew Ulanowski et al. "Incidence of rough and irregular atmospheric ice particles from Small Ice Detector 3 measurements". In: *Atmospheric Chemistry and Physics* 14.3 (2014), pp. 1649–1662. DOI: 10.5194/acp-14-1649-2014.

[152] Zbigniew Ulanowski et al. "Light scattering by ice particles in the Earth's atmosphere and related laboratory measurements". In: *12th Int Conf on Electromagnetic and Light Scattering*. FIN: University of Helsinki, 2010, pp. 294–297. URL: https://uhra.herts.ac.uk/id/eprint/13530/.

[153] Benedikt Urbanek et al. "High depolarization ratios of naturally occurring cirrus clouds near air traffic regions over Europe". In: *Geophysical research letters* 45.23 (2018), pp. 13–166. DOI: 10.1029/2018gl079345.

[154] Étienne Vignon et al. "Ice fog observed at cirrus temperatures at Dome C, Antarctic Plateau". In: *Atmospheric Chemistry and Physics* 22.19 (2022), pp. 12857–12872. DOI: 10.5194/acp-22-12857-2022.

[155] Aki Virkkula et al. "Aerosol optical properties calculated from size distributions, filter samples and absorption photometer data at Dome C, Antarctica, and their relationships with seasonal cycles of sources". In: *Atmospheric Chemistry and Physics* 22.7 (2022), pp. 5033–5069. DOI: 10.5194/acp-22-5033-2022.

[156] Paul Vochezer et al. "In situ characterization of mixed phase clouds using the Small Ice Detector and the Particle Phase Discriminator". In: *Atmospheric Measurement Techniques* 9.1 (2016), pp. 159–177. DOI: 10.5194/amt-9-159-2016.

[157] Andy M Vogelmann and TP Ackerman. "Relating cirrus cloud properties to observed fluxes: A critical assessment". In: *Journal of Atmospheric Sciences* 52.23 (1995), pp. 4285–4301. DOI: 10.1175/1520-0469(1995)052<4285:rccpto>2.0.co;2.

[158] Jens Voigtländer et al. "Surface roughness during depositional growth and sublimation of ice crystals". In: *Atmospheric Chemistry and Physics* 18.18 (2018), pp. 13687–13702. DOI: 10.5194/acp-18-13687-2018.

[159] Robert Wagner et al. "Probing ice clouds by broadband mid-infrared extinction spectroscopy: case studies from ice nucleation experiments in the AIDA aerosol and cloud chamber". In: *Atmospheric Chemistry and Physics* 6.12 (2006), pp. 4775–4800. DOI: 10.5194/acp-6-4775-2006.

[160] Shawn W Wagner et al. "Light scattering and microphysical properties of atmospheric bullet rosette ice crystals". In: *Atmospheric Chemistry and Physics* 25.15 (2025), pp. 8785–8804. DOI: 10.5194/acp-25-8785-2025.

[161] Fritz Waitz et al. "PHIPS-HALO: the airborne Particle Habit Imaging and Polar Scattering probe–Part 3: Single-particle phase discrimination and particle size distribution based on the angular-scattering function". In: *Atmospheric Measurement Techniques* 14.4 (2021), pp. 3049–3070. DOI: 10.5194/amt-14-3049-2021.

[162] Von P Walden, Stephen G Warren, and Elizabeth Tuttle. "Atmospheric ice crystals over the Antarctic Plateau in winter". In: *Journal of Applied Meteorology* 42.10 (2003), pp. 1391–1405. DOI: 10.1175/1520-0450(2003)042<1391:aicota>2.0.co;2.

[163] Yuan Wang et al. "Impact of cloud ice particle size uncertainty in a climate model and implications for future satellite missions". In: *Journal of Geophysical Research: Atmospheres* 125.6 (2020), e2019JD032119. DOI: 10.1029/2019jd032119.

[164] Zhien Wang and Kenneth Sassen. "Cloud type and macrophysical property retrieval using multiple remote sensors". In: *Journal of Applied Meteorology and Climatology* 40.10 (2001), pp. 1665–1682. DOI: 10.1175/1520-0450(2001)040<1665:ctampr>2.0.co;2.

[165] Darryn W Waugh and William J Randel. "Climatology of Arctic and Antarctic polar vortices using elliptical diagnostics". In: *Journal of the Atmospheric Sciences* 56.11 (1999), pp. 1594–1613. DOI: 10.1175/1520-0469(1999)056<1594:coaaap>2.0.co;2.

[166] Heike Wex et al. "Antarctica's Unique Atmosphere: Really Low INP concentrations". 2024. DOI: 10.22541/au.172953981.12412340/v1.

[167] Warren J Wiscombe. "The delta–M method: Rapid yet accurate radiative flux calculations for strongly asymmetric phase functions". In: *Journal of Atmospheric Sciences* 34.9 (1977), pp. 1408–1422. DOI: 10.1175/1520-0469(1977)034<1408:TDMRYA>2.0.CO;2.

[168] Kevin Wolf, Nicolas Bellouin, and Olivier Boucher. "Sensitivity of cirrus and contrail radiative effect on cloud microphysical and environmental parameters". In: *Atmospheric Chemistry and Physics* 23.21 (2023), pp. 14003–14037. DOI: 10.5194/acp-23-14003-2023.

[169] Sarah Woods et al. "Microphysical properties of tropical tropopause layer cirrus". In: *Journal of Geophysical Research: Atmospheres* 123.11 (2018), pp. 6053–6069. DOI: 10.1029/2017jd028068.

[170] World Meteorological Organization. *Diamond dust (last access: 03.02.2025)*. URL: https://cloudatlas.wmo.int/en/diamond-dust.html.

[171] World Meteorological Organization. *Ice fog (last access: 03.02.2025)*. URL: https://cloudatlas.wmo.int/en/ice-fog.html.

[172] Donald P Wylie et al. "Four years of global cirrus cloud statistics using HIRS". In: *Journal of Climate* 7.12 (1994), pp. 1972–1986. DOI: 10.1175/1520-0442(1994)007<1972:fyogcc>2.0.co;2.

[173] Guanglang Xu, Martin Schnaiter, and Emma Järvinen. "Accurate retrieval of asymmetry parameter for large and complex ice crystals from in-situ polar nephelometer measurements". In: *Journal of Geophysical Research: Atmospheres* 127.3 (2022), e2021JD036071. DOI: 10.1029/2021jd036071.

[174] Jianzhong Xu et al. "Characteristics of atmospheric ice nucleating particles over East Antarctica retrieved from the surface snow". In: *Science of The Total Environment* 888 (2023), p. 164181. DOI: 10.1016/j.scitotenv.2023.164181.

[175] Ping Yang and KN Liou. "Finite-difference time domain method for light scattering by small ice crystals in three-dimensional space". In: *Journal of the Optical Society of America A* 13.10 (1996), pp. 2072–2085. DOI: 10.1364/josaa.13.002072.

[176] Ping Yang and KN Liou. "Geometric-optics–integral-equation method for light scattering by nonspherical ice crystals". In: *Applied Optics* 35.33 (1996), pp. 6568–6584. DOI: 10.1364/ao.35.006568.

[177] Ping Yang and KN Liou. "Light scattering by hexagonal ice crystals: comparison of finite-difference time domain and geometric optics models". In: *JOSA A* 12.1 (1995), pp. 162–176. DOI: 10.1364/josaa.12.000162.

[178] Ping Yang et al. "Effect of cavities on the optical properties of bullet rosettes: Implications for active and passive remote sensing of ice cloud properties". In: *Journal of applied meteorology and climatology* 47.9 (2008), pp. 2311–2330. DOI: 10.1175/2008jamc1905.1.

[179] Ping Yang et al. "On the radiative properties of ice clouds: Light scattering, remote sensing, and radiation parameterization". In: *Advances in Atmospheric Sciences* 32.1 (2015), pp. 32–63. DOI: 10.1007/s00376-014-0011-z.

[180] Ping Yang et al. “Spectrally consistent scattering, absorption, and polarization properties of atmospheric ice crystals at wavelengths from 0.2 to 100 μm”. In: *Journal of the atmospheric sciences* 70.1 (2013), pp. 330–347. DOI: 10.1175/jas-d-12-039.1.

[181] Xuanhao Zhu et al. “Backscattering properties of randomly oriented hexagonal hollow columns for lidar application”. In: *Optics Express* 31.21 (2023), pp. 35257–35271. DOI: 10.1364/oe.502185.

[182] Donald W Zimmerman and Bruno D Zumbo. “Rank transformations and the power of the Student t test and Welch t’test for non-normal populations with unequal variances.” In: *Canadian Journal of Experimental Psychology/Revue canadienne de psychologie expérimentale* 47.3 (1993), p. 523. DOI: 10.1037/h0078850.